UNIVERSITY OF SOUTHAMPTON

FACULTY OF ENGINEERING, SCIENCE AND MATHEMATICS

INSTITUTE OF SOUND AND VIBRATION RESEARCH

USE OF FAN RIG DATA FOR THE UNDERSTANDING AND PREDICTION OF FAN BROADBAND NOISE AND NOISE CHANGES DUE TO A VARIABLE AREA NOZZLE

by
Eugene Pio Deane

Submitted in partial fulfillment for the degree of
Doctor of Engineering (EngD)

September 2009

Abstract

This thesis presents the results of the research component of this EngD, entitled

Use of fan rig data for the understanding and prediction of fan broadband noise and noise changes due to a variable area nozzle

As suggested by the title, fan rig noise measurements form an integral part of this thesis. The analysis of a database of rig noise measurements forms the first section of this thesis, in two parts. The first part describes the analysis of a set of fan rig noise measurements, including the variation of fan broadband and tone noise in forward and rearward arcs. The second part examines a large database of fan rig noise measurements, and attempts to derive correlations of fan broadband noise and fan performance parameters. Cluster Analysis, Principle Component Analysis, and Regression Analysis are used to understand and describe the underlying physics of broadband noise generation and the relationships between these predictors.

The second section of this thesis uses a cascade broadband noise model to investigate rotor-stator broadband noise. Predictions of the broadband noise from this noise model are compared to rig measurements, showing good accuracy. The underlying physics of rotor-stator broadband noise generation is investigated by performing two parametric studies using the broadband noise model. The first parametric study investigates the effect on broadband noise of simple flow and geometric parameters, namely number of vanes, vane chord, vane stagger angle, and rotor wake turbulence intensity, turbulent length scale, and flow Mach number onto the cascade. These results are used to derive scaling power laws for the prediction of changes in broadband noise due to changes in these parameters. The second parametric study expands upon this by investigating the effect on broadband noise of the fan design parameters shaft speed, pressure ratio, and efficiency, at approach, cutback and cruise conditions. The variation in broadband noise due to these design parameters is explained by considering the underlying flow and geometric parameters such as number of vanes and Mach number, and the scaling power laws based on these simple parameters are used to predict the change in broadband noise between different performance points.

The final section of this thesis investigates the effect of varying exhaust nozzle area on total engine noise. A new method is presented that allows the transfer of changes in fan rig noise to

engine noise predictions, to estimate the change in fan noise due to the pressure ratio changes brought about by a variable area nozzle. Changes in engine noise are investigated for approach, cutback, and sideline conditions, and the application of the new method assessed.

As the research displayed in this thesis is closely linked to industry, the foundation of work presented in several chapters is dependent on data or figures that are commercially sensitive. It has therefore been necessary to create a confidential appendix (Appendix X) to include these commercially sensitive items. These additional results and figures in Appendix X are supplementary in nature, and sufficient results are presented in the public thesis to illustrate the results of the various chapters. Where supplementary information and results are available, this is clearly indicated at the pertinent point in the published thesis, along with the section of Appendix X where the information can be found. In order to gain access to Appendix X, please contact:

Team Leader – Fan Noise
Noise Control Engineering,
Rolls-Royce plc,
SINA-76,
PO Box 31,
Derby DE24 8BJ,
England

Acknowledgements

This thesis is dedicated to my mother Bernie, and fiancée Huijie.

As an EngD is by design an industrial doctorate, there are therefore numerous people who should be thanked for their assistance, both during my time at the University of Southampton, and when at Rolls-Royce, Derby.

Starting with the University of Southampton I should first and foremost thank Prof. Phil Joseph. His assistance throughout this EngD was invaluable during all the projects undertaken, and his patience and good humour when writing the thesis itself was unending. His door is literally always open for a chat. I must also thank Prof. Jeremy Astley for his help during this program, particularly when writing the thesis to satisfy both academic and industrial aspects. His advice and assistance at various stages has been most helpful. I would also like to thank my colleagues and fellow students in the ISVR for the breaks and chats during the past few years, particularly (in alphabetical order) Mahdi Azarpeyvand, Fabrice Castres, Chris Lowis, Claire McAleer, Phil McLaughlin, Chris Powles, and Iansteel Achunche.

At Rolls-Royce I received assistance from practically everyone in the Noise Group at some stage or other; however there are a few people who I should name personally. Dr. Andrew Kempton has been of great help throughout this EngD, both at the University of Southampton and at Rolls-Royce. His advice on the industrial side of the projects and working in industry has been invaluable. While at Rolls-Royce I received a great deal of help from Dr. Alec Wilson, particularly with respect to the broadband noise parametric study shown in this thesis, and without his help certain aspects of the study would not have been possible. Dr. Nick Humphreys gave much advice when working on tasks for external projects, particularly on how to report to external partners, and took responsibility for ensuring the thesis does not display any sensitive data. His assistance on satisfying commercial interests in the thesis has been very useful. I would also like to thank Joe Walsh, for giving me the opportunity to work on the variable area nozzle project, and his advice on the various aspects of the work.

In addition, I must thank my parents Eugene and Bernie for all their love and support throughout my life and all my studies, including their patience with this EngD. I am eternally

grateful for what they taught me about life and work, and although my mother sadly passed away before the completion of this degree her encouragement never wavered.

And finally, though most importantly, I would like to thank my fiancée Huijie for her patience and support during this doctorate. I hope I do not try her patience as much in the future.

Contents

List of Figures

Appendices

Nomenclature

a	Speed of sound, dimensional weighting coefficient
$\boldsymbol{a}$	Weighting coefficient matrix
$\boldsymbol{a_0}$	Optimal weighting coefficient matrix
B	Number of blades
BB	Broadband region
BDC	Bottom Dead Centre measurement position
BFM	Bypass Forward Mode Ring
BPF	Blade Passing Frequency
BRA	Bypass Rear Axial Array
BRM	Bypass Rear Mode Ring
b	Semi-chord
C	Correlation matrix
C_d	Profile drag coefficient
C_D	Blade drag coefficient
c	Aerofoil chord, correlation coefficient
DF	Diffusion factor
D	Correlation distance matrix
d	Characteristic width of wake generator, correlation distance coefficient
dB	Decibel
EO	Engine Order
$EPNLdB$	Effective Perceived Noise Levels in dB
F	Drag force per unit span
f_c	Critical frequency (Hz)
$g(x,k_x,k_y)$	Aerodynamic transfer function
I	Acoustic intensity
i	Imaginary number
k	Gust wave number, turbulent kinetic energy
k_1	Chord-wise acoustic wave number
k_2	Gap-wise acoustic wave number
k_s^+	Non-dimensional sand roughness height
L	Eigenvalues derived during principle component analysis
$\overline{L}$	Span of wake generator
L_w	Mean wake half-wake width
l	Length scale, wake scaling length, acoustic mode number
l_n	Natural logarithm
M	Mach number
M_{Rel}	Fan tip relative Mach number
M_1	Axial Mach number component - $M\cos\theta$
M_2	Gap-wise Mach number component - $M\sin\theta$
m	Spinning mode order
$\dot{m}$	Mass flow
N	RPM, Number of predictors in regression equation
n	Harmonic of blade passing frequency
OGV	Outlet Guide Vane
P	Mean pressure
ΔP	Pressure jump
PWL	Sound power
$\tilde{\mathbf{P}}$	Standardised predictor matrix
P	Predictor matrix
p	Predictor
p_f	Fan generated acoustic pressure
p_t	Throttle generated acoustic pressure
p_∞	Freestream pressure
Q	Independent predictor
Q_l	Non-dimensional modal power response function
q	Velocity Scale
R^2	Regression equation residual squared
R_r	Cascade response function
ΔR	Width of cascade strip

r	Scattering index, least squares analysis residual
SPL	Sound Pressure Level
S	Spreading rate, similarity, duct cross section
St	Strouhal frequency
s	Interblade spacing
s^2	Mean squared error
s/c	Space chord ratio
TDC	Top Dead Centre measurement position
T	Mean temperature
t	Time
U	Mean freestream velocity
U_w	Mean wake axial velocity deficit
U_e	Wake edge velocity $= 0.99U_\infty$
U_∞	Freestream velocity
U^+	Dimensionless velocity
u_x	Wall friction velocity
V	Number of vanes, Predictor amplitude
V'	Total wake root mean square (rms) turbulence intensity, circumferentially averaged
V_m	Mixed jet velocity
V_θ	Whirl velocity
V_1	Average velocity entering blade row
V_2	Average velocity exiting blade row
W	Mean circumferential velocity
w	Circumferential turbulent velocity component
$\boldsymbol{w}$	Sound power matrix
w_g	Harmonic gust velocity
w_0	Harmonic gust amplitude
x	Axial distance
x_0	Virtual origin
Δx	Change in axial distance
y	Gapwise coordinate
y^+	Dimensionless wall distance
$\mathbf{Z}$	Matrix of principle components

z	Spanwise coordinate
α_r	Axial acoustic wave number
β_r	Acoustic circumferential wave number
β_s	Non-dimensional constant, see Eq (4.8.2-1)
σ	See Equation 5-3
δ	Kronecker delta
ε	Turbulence dissipation
ξ	Throttle parameter
η	y/L_w, Efficiency
Λ	Turbulent length scale
λ	Reduced frequency
λ_u	Axial integral length scale
λ_v	Circumferential integral length scale
λ_w	Radial integral length scale
Ω	Shaft rotational frequency
ω	Angular frequency (rads)
ω_{BPF}	Blade passing frequency (rads)
ω_c	Critical frequency (rads)
Π	Sound power
π	Pi
ρ_0	Freestream density
θ	Momentum thickness, cascade stagger angle
ϕ	Phase angle
Φ_{ww}	Turbulence spectra
τ	Time scale
τ_w	Wall shear stress
ν	Kinematic viscosity
Δ	'Delta', change in variable
$E[\ ]$	Expectation
$\bar{}$	Time averaged
$\pm$	+ Upstream and - downstream propagation
T	Matrix transpose
*	Complex conjugate
$_{1,2}$	Axial and gapwise coordinates
:	Notation for variation in cascade parameters, e.g. 10:10:60 denotes 10 to 60, in steps of 10

Chapter 1
Overview of EngD Project

1. Overview of EngD Project

1.1. Philosophy of EngD program

This thesis presents the research work carried out in partial fulfilment of an Engineering Doctorate (EngD). An EngD is a four-year research program, during which research is undertaken that is of interest to, and in close collaboration with, an industrial sponsor.

The research of an EngD can be strongly interdisciplinary, and involve a number of related projects that fall under an overall umbrella title. The research must reflect the state of the art in the field, and display originality and creativity as in a traditional PhD. However, unlike a traditional PhD, the work must be directly applicable to an industrial or commercial context. This context is provided by the industrial sponsor.

The main theme of this EngD thesis is aircraft noise. The aim is to analyse rig measured fan noise, and use this noise data in the prediction of both fan broadband noise and the noise effects of a variable area nozzle. A 'road-map' for this EngD program, describing the research topics and their integration, is discussed in Section 1.5.

The EngD program differs from a traditional PhD program in that it combines doctoral research with a significant taught component which is assessed by examination and coursework. In total a minimum of 1200 Hours of study are required from technical (MSc), management (MBA) and generic skills courses. In total 1325 hours of study were completed during this EngD, before the end of the second year.

1.2. Overview of Research Component

This thesis presents the results of several investigations into aero-engine noise. The core study in this thesis is an investigation into fan rig noise measurements. This provides a greater understanding of the associated noise sources, both tone and broadband, in both forward and rearward arcs. This rig data is used to provide input to, and validate the results of the other investigations in this EngD.

An analytic computer model is used to investigate fan rotor-stator interaction broadband noise. Two parametric studies are carried out using the rotor-stator interaction broadband noise model. The first parametric study investigates the effect on broadband noise of varying simple geometric and aerodynamic parameters associated with the stator vanes. The second parametric study investigates the

effect of varying fan design parameters (efficiency, pressure ratio and shaft speed) on fan broadband noise at cruise, cutback and approach flight conditions.

Another investigation reported in this thesis is that of a statistical analysis of a large fan rig noise database. A number of statistical techniques are used to provide a greater understanding of groups of various correlated flow and performance parameters, and how these correlate with the measured broadband noise. This analysis is used to generate regression equations relating broadband noise to various flow and performance parameters.

The final major section of this thesis presents an investigation into the total aircraft and total engine noise effects of a variable area nozzle on several engines at certification flight points. Variable Area Nozzles are a technology currently under investigation for their potential benefits to both engine performance and noise. This study provides a procedure using fan rig noise data for incorporating fan noise changes due to nozzle area variations into the prediction of total engine noise.

Although the investigations of this EngD are on aero-engine noise, any interpretation relies on knowledge of how the performance of an aero-engine fan is characterised using the concept of working lines. A brief introduction of working line theory is provided in Appendix D.

1.3. EngD Calendar

A calendar outlining the timescales of this EngD can be seen below in Table 1. This includes time spent undertaking either courses or research, stating whether this work was carried out in the Rolls-Royce University Technology Centre (UTC) at the University of Southampton, or at industry. During the course of the EngD, approximately 18 months were spent working at the industrial site, with the remainder spent at the University of Southampton.

Year	2004	2005				2006				2007					2008		
Quarter	4	1	2	3	4	1	2	3	4	1	2	3	4	1	2	3
Topic	Study			Research	Study and Research				Research							
Location	University			Rolls-Royce	University				Rolls-Royce					University		

Table 1 – Calendar of EngD activities

1.4. Overview of taught component

As mentioned previously, the EngD program differs from a traditional PhD in that it also includes a significant taught component, with modules chosen from technical, management and generic skills

streams. In total, 1325 hours of study were completed for these courses, presented below beginning with the technical modules.

1.4.1. Technical modules

The technical modules, completed as part of this EngD program, were chosen for their relevance to aircraft noise. The background of the candidate was in Aeronautical Engineering. No study of acoustics had been performed previously. Modules in acoustics, and signal processing and analysis were therefore undertaken. Due to the emphasis on fan broadband noise, and the importance of the rotor wake on this noise generating mechanisms, further modules were completed on flow turbulence in both physics and modelling. The final technical modules were on numerical methods, and flow control. The technical modules taken by the candidate are listed below:

	Study Hours
• Fundamentals of Acoustics	100
• Analytical and Numerical Acoustics	100
• Signal Processing and Analysis	100
• Numerical Methods	100
• Turbulence 1: Physics and Experiment	100
• Turbulence 2: Computation and Modelling	100
• Flow Control	100

1.4.2. Management modules

The complete list of management modules can be seen below:

	Study Hours
• Analytic Skills	70
• International Business	70
• Project Risk Management 1	70
• Problem Structuring	70
• Business Ethics	70
• Risk and Crisis Management	75

1.4.3. Generic Skills

Generic Skill courses encompass many of the different skills required during and after the EngD program. These courses include presentation skills, negotiation skills, technical writing, CV preparation, and team working. Research engineers are also required to present results of their studies at an annual EngD conference day, in addition to presenting at external conferences. In total these generic skill courses account for 200 study hours.

1.5. Breakdown of Thesis

Figure 1.5-1 shows the 'roadmap' for this EngD program, along with associated thesis chapters where appropriate. This is discussed in the following chapter.

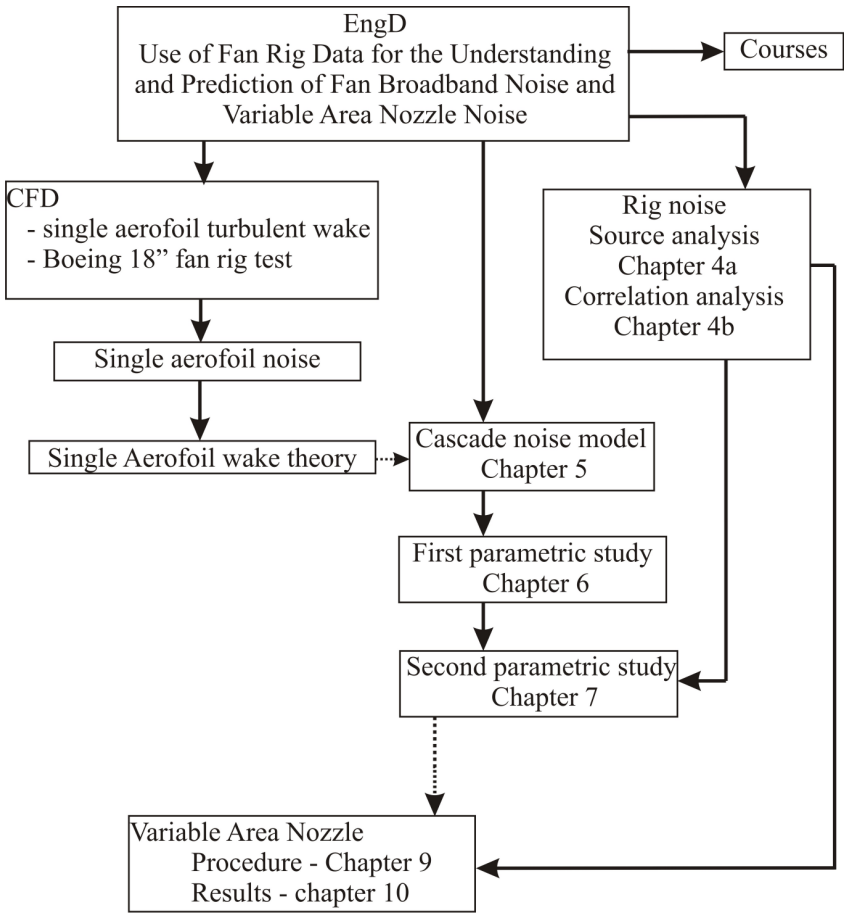

Figure 1.5-1 – Roadmap outlining EngD structure

Chapter 2
Overview of Thesis Chapters

2. Overview of Thesis Chapters

An overview of the contents in each chapter is presented below. As the research displayed in this thesis is closely linked to industry, the foundation of work presented in several chapters is dependent on data or figures that are commercially sensitive. It has therefore been necessary to create a confidential appendix (Appendix X) to include these commercially sensitive items. These additional results and figures in Appendix X are supplementary in nature, and sufficient results are presented in the public thesis to illustrate the results of the various chapters. Where supplementary information and results are available, this is clearly indicated at the pertinent point in the published thesis, along with the section of Appendix X where the information can be found. In order to gain access to Appendix X, please contact the Fan Noise Team Leader at Rolls-Royce plc, Derby.

2.1. Chapter 3

Chapter 3 includes a review of the literature relevant to the investigations of this thesis. This includes papers and reports on rig noise measurements and analysis. Also discussed are papers concerning broadband noise modelling, and those presenting the results of investigations into the acoustic effects of a variable area nozzle on fan noise.

2.2. Chapter 4

A central theme of this thesis concerns rig noise and analysis. Chapter 4 is separated into two sections 4a and 4b, describing two separate rig noise investigations of a measured rig noise dataset.

Chapter 4a provides an analysis of individual fan noise sources. Several results from this chapter can be found in Chapter 4a of Appendix X. Both tone and broadband noise measurements in forward and rearward arcs are plotted against fan pressure ratio and mass flow on working line diagrams. This data is used in each of the other main sections of this thesis. The rotor-stator broadband noise model presented in Chapter 7 uses rig noise measurements to verify the broadband noise predictions of realistic fan stages. Fan rig noise measurements are also used to predict changes in noise level of the various fan noise sources as a function of variable nozzle area, in Chapters 8 and 9.

Chapter 4b presents a correlation analysis of rig noise measurements from many rig datasets. Statistical methods are used to derive the final regression equations, between rig measured fan broadband noise and flow and rig predictors.

The statistical techniques are used to provide an increased understanding of the physics of the different predictors included in the analysis and their mutual correlation. Principle Component Analysis is used to indicate the number of uncorrelated components within the rig noise dataset, indicating the number of predictors required in the final equations. Cluster Analysis is used to reduce the rig noise dataset into groups of uncorrelated performance variables. Regression Analysis is then used to form the final regression equations that predict the rig measured broadband noise from a number of representative uncorrelated components, chosen from the Cluster Analysis results.

2.3. Chapter 5

This chapter is the first of three chapters aimed at understanding fan broadband noise. Chapter 5 presents the theory underlying the broadband noise model at the heart of Chapters 6 and 7. Also introduced is the critical frequency defined in Reference [11], used to separate the modelled broadband noise spectra into low and high frequency bands.

2.4. Chapter 6

Chapter 6 presents the results of the first of two parametric studies performed using the broadband noise model. This first parametric study considers the effect on fan broadband noise of simple geometric (number of vanes, stagger angle, and vane chord) and flow parameter (Mach number, turbulence intensity, and turbulence length scale). The variations in broadband noise are used to derive sound power scaling laws based on the most important of these predictors. These sound power scaling laws are subsequently used in Chapter 7 to predict changes in sound power level between various test points.

2.5. Chapter 7

The parametric study of Chapter 6 is extended in Chapter 7, which considers the effect on broadband noise of the fan design parameters of fan efficiency, pressure ratio, and shaft speed. This chapter presents the predictions of the fan broadband noise, though several results are to be found in Appendix X. The accuracy of these predictions are compared to rig measurements. Use is made of the sound

power scaling laws derived in the first parametric study of Chapter 5 to predict the broadband noise changes between different flight cases. These scaling laws provide an efficient prediction of the changes in sound power without having to run the broadband noise model.

2.6. Chapters 8 and 9

Chapter 8 introduces the final investigation into the effects of a Variable Area Nozzle on total aircraft noise. This chapter introduces the procedure used to extract fan noise changes for changes in working line, from the rig noise data described in Chapter 4. Chapter 9 then presents the resulting noise effects of a Variable Area Nozzle on several engines. These results are presented at certification flight points. Additional results from this investigation can be seen in Appendix X.

2.7. Engines investigated during this thesis

During this thesis fan noise rig measurements were used from a range of representative fan stage geometries. These were used for the prediction and validation of fan broadband noise. Finally the performance of these engines was used to allow prediction of the effect of a variable area nozzle on aircraft noise. Five engines are investigated. The relationship between these engines is presented in Section 2.7 of Appendix X, however the relative performance of each engine is ranked in Table 2 below. The smallest diameter, lowest thrust, and lowest shaft speed, are ranked 1.

Engine	Normalised Diameter	Normalised Thrust	Normalised Shaft Speed
Engine 1	1	5	4
Engine 2	4	4	3
Engine 3	2	2	1
Engine 4	5	1	5
Engine 5	3	3	2

Table 2 – Relative performance descriptions of engines used in this thesis

2.8. Additional technical work *not* included in the thesis

Early work undertaken in the EngD program included the completion of the courses listed previously. Initial research concentrated on the use of off-the-shelf CFD codes for the prediction of turbulent wakes generated by individual aerofoils and rotor blades, and the noise generated by individual blades subjected to turbulent wakes. Early work investigated the use of commercial RANS CFD codes for the prediction of the turbulent wake of a NACA 0012 aerofoil. This assessed the use of RANS CFD in

predicting the self-similarity and evolution of turbulent wakes, with a view to using these results to generate the turbulent wakes impinging on a downstream stator cascade for broadband noise prediction. Note that although this work is not reported in this thesis it is presented in the conference paper [13]. This work was extended by the use of a RANS CFD code to predict the wakes of the Boeing 18" fan, for comparison with the results of [16]. However blade geometry information provided was found to be insufficiently precise to provide accurate predictions, and so these results are not included in this thesis.

The following chapter presents a review of the literature relevant to the work presented in this thesis, commencing with a discussion on the importance of aircraft noise.

Chapter 3
Aircraft noise overview: a survey of relevant literature

3. Aircraft noise overview: a survey of relevant literature

3.1. Importance of aircraft noise

The airport and airline industries are estimated to be worth £18.4 billion per year to the UK Gross National Product[1], £7.8 billion in taxation to the exchequer, and directly supports 234,000 jobs. Air travel is forecast to grow greatly over the coming decades, with some predictions of unconstrained growth estimating 2030 levels of three times that of the year 2000 [51] as plotted in Figure 3.1-1:

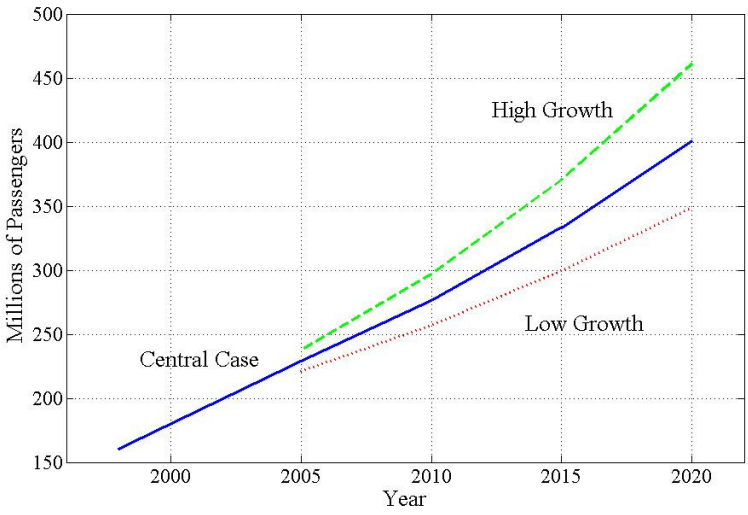

Figure 3.1-1 - Forecast growth of aviation in the UK, 1998 to 2020 [51]

Clearly such growth, while benefiting both the population and the economy, will have an adverse effect on the environment especially in terms of noise and air pollution. This problem is being addressed both at national and international levels in the United States (US) and European Union (EU).

The Advisory Council for Aeronautics Research in Europe (ACARE) [51] in 2001 published a report entitled 'European Aeronautics: A Vision for 2020'. In this report the Strategic Research Agenda (SRA) states the four aims:

1. Reduce fuel consumption and CO_2 emissions by 50%
2. Reduce perceived external noise by 50%
3. Reduce emission of NO_X by 80%
4. Make substantial progress in reducing environmental impact of manufacture, maintenance and disposal of aircraft and related products

[1] Figures from British Air Transport Association, 2009

There are numerous noise sources on an aircraft present on both the airframe and the engine. However, their importance varies depending on the flight regime. Figure 3.1-2 below shows the estimated contributions made by the engine, both in terms of individual component noise and total noise, and airframe noise in the two flight regimes of take-off and approach [52].

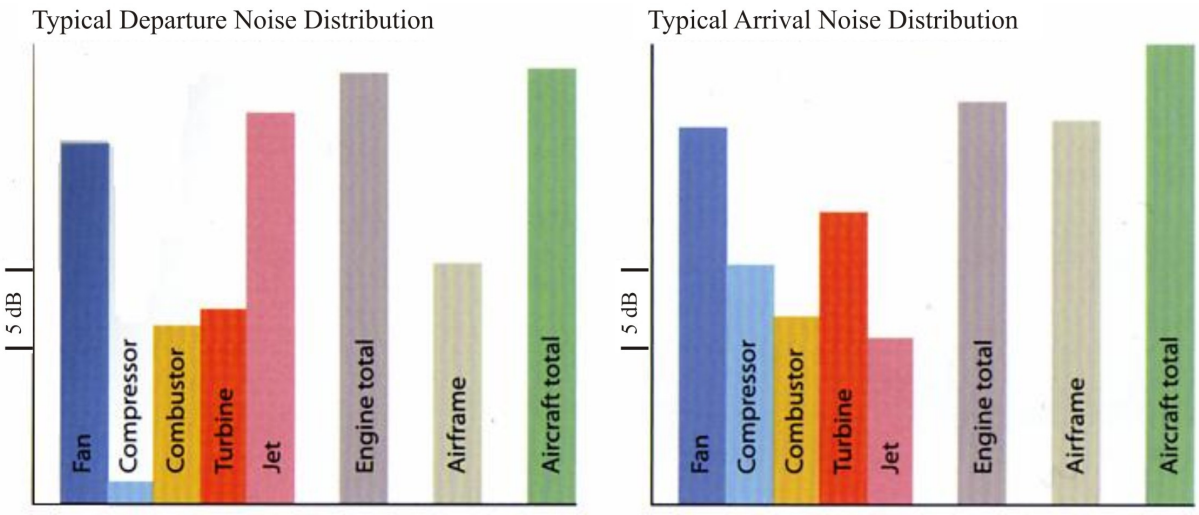

Figure 3.1-2 - The main contributing noise sources for take-off and approach [52]

Although the airframe contribution is considerable, especially at approach, the noise generated by the engine is dominant in both cases, especially at take-off.

3.2. Sources of aircraft noise

Also shown in Figure 3.1-2 above are the contributions of the major noise generating engine components. The magnitude and directivity of these noise sources are shown below in Figure 3.2-1.

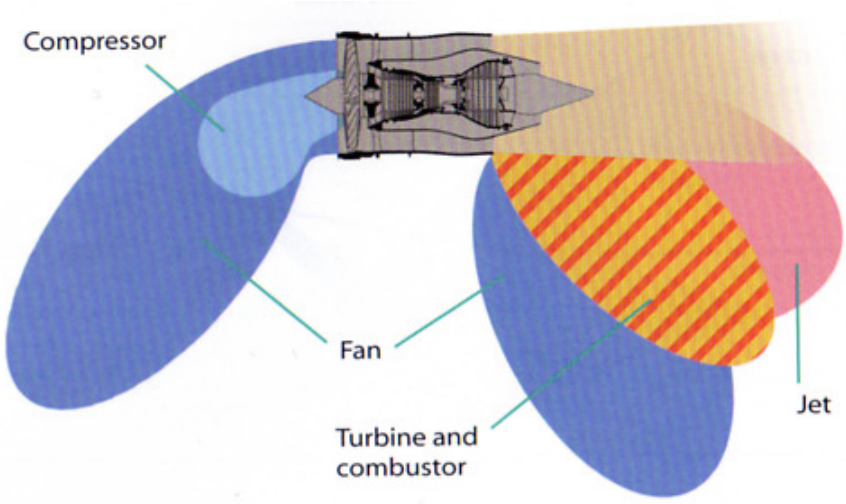

Figure 3.2-1 - Individual noise generating components of a typical modern engine [52]

The most important noise generation mechanisms to overall aircraft noise are jet noise and fan noise. These are further discussed below.

3.2.1. Jet Noise

Jet noise is the principal noise source at take-off, as the aircraft engine is operating under full-power and the jet velocity is at a maximum. The engine exhaust gases are expelled at high velocity, and the noise is generated by the turbulent mixing of these gases with the ambient air. The noise produced by a single-stream jet increases in proportion to the jet velocity to the power of eight.

Jet noise is the only engine noise source that is generated outside the engine. The mixing and noise generation takes place over a large axial distance downstream that can be equivalent to ten nozzle diameters. Smaller turbulence length scales close to the nozzle produces higher frequency noise. As the length scale increases with axial downstream distance (beyond approximately 5 jet diameters downstream) this in turn generates lower frequency noise.

Jet noise was the main contributor to the high noise levels generated by the first generation of turbo-jets. These had either no bypass flow, or were low bypass ratio turbofans. The contribution of jet noise to overall noise levels has now been alleviated greatly with the introduction of higher bypass ratio turbo-fan engines. These allow the same thrust level to be achieved by moving a larger mass of air at a slower velocity. Further jet noise reductions can also be achieved by increasing the mixing between flows before exhausting to the atmosphere. This can be achieved by using a core mixer such as that shown in Figure 3.2.1-1, though the increased drag and weight penalties caused by the inclusion of this device need to be considered to determine if this is the optimum choice for an engine application. Another device to reduce jet noise are nozzle serrations, as shown in Figure 3.2.1-2.

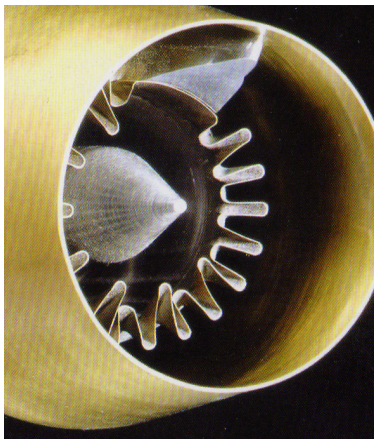

Figure 3.2.1-1 – Jet noise alleviation by core mixer [52]

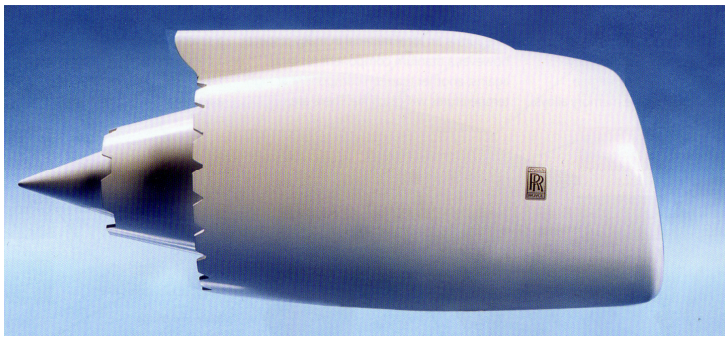

Figure 3.2.1-2 – Jet noise alleviation by nozzle serrations [52]

3.2.2. Fan Noise

At subsonic speeds, fan noise is predominantly generated by the interaction between the fan blade wakes and the stators. This noise then radiates both upstream and downstream of the fan stage. From Figure 3.2-1 it is seen that the noise contribution by the fan is significant, being only slightly lower in level than the jet noise at take-off, but also being the dominant source at approach. Fan noise has both tonal and broadband components. Fan broadband noise is becoming increasingly important as fans become larger and rotate at lower speeds.

3.2.2.1. Tone Noise

At subsonic rotor tip speeds, tone noise is predominantly generated by rotor-stator interaction, at the blade passing frequency and its harmonics. This propagates both down the bypass duct, and upstream through the rotor. Fan blade tip speeds that exceed the speed of sound generate ‘buzz’ noise, so-called because of it’s distinct ‘circular saw’ sound. At supersonic fan tip speeds, shock waves form in the passages between blades. Slight variations between individual shock waves are the cause of buzz-saw noise and produce tones at harmonics of the shaft rotation frequency.

3.2.2.2. Broadband Noise

Most turbo-machinery broadband noise is generated whenever turbulent flow interacts with a surface. It is believed that there are four main fan broadband noise mechanisms:

1. Interaction between turbulence from rotor wake impinging on downstream stators
2. Rotor alone noise
3. Inlet boundary layer growth and interaction with rotor
4. OGV alone noise

The broadband noise investigation that forms a significant part of this thesis describes an investigation into the first mechanism listed above.

The following sections discuss the important literature relevant to the investigations described in this thesis. The first section discusses rig noise measurements, of which there are surprisingly few reported in the open literature that directly measures rig noise and aerodynamic parameters. This is followed by a discussion of the broadband fan noise models published in the literature. The models included in this discussion are broadband noise models that take into account cascade effects in which the influence of adjacent blades on the generated noise are important. Finally, the recent work on variable area nozzles, a technology that is in the early stages of consideration for amelioration of aircraft noise, is discussed.

3.3. Broadband Noise Parameter and Correlation Studies

The mechanism of fan broadband noise generation is complex. Each of the four main broadband sources discussed above in Section 3.2.2.2, involves the complex interaction between fan blades and turbulence, which is poorly understood. This has motivated studies of fan broadband noise by experiment, analysis, and numerical methods. The dominant fan broadband noise source is believed to be due to the interaction between the turbulent wake generated by upstream rotating rotors impinging onto downstream stators. To the Author's knowledge very little work has been published on the subject of the characteristics of the turbulent wake from a ducted rotor in a smooth uniform flow. The important work on the measurement of turbulence within, and noise from, fan rigs is now presented.

3.3.1. Derivation of Fan Wake Turbulence Correlations - Gliebe et al

The first work to be discussed here is that of Gliebe et al [21], whose results have influenced the results of the fan broadband noise investigations presented in this thesis. This is a comprehensive study that describes a number of aeroacoustic prediction codes to model various engine noise sources, not only fan broadband noise. However, in order to provide accurate inputs to their fan broadband noise model, Gliebe et al also produce correlations of experimentally measured turbulence parameters. These correlations are used in this thesis. Gliebe et al use the results of Wygnanski et al [50] who show that the turbulent quantities of the wake generated by an aerofoil can be estimated from knowledge of the mean wake width and the maximum velocity deficit, and the aerofoil trailing edge momentum thickness. Gliebe et al use this work to produce correlations that predict the evolution of

various mean and turbulent wake parameters with increasing downstream distance. These correlations are derived from data measured during fan stage tests at the Low Speed Research Compressor (LSRC), configured to simulate a fan stage with large axial spacing. All three components of the wake turbulence intensity and integral length scales can be predicted from the wake momentum thickness and axial distance downstream. These correlations are therefore used to predict the turbulence inputs to the broadband noise modelling of real fan stages, in the second broadband noise parametric study presented in Chapter 7. The correlations due to Gliebe are presented in Appendix C-2.

3.3.2. Boeing 18-inch fan rig broadband noise test - Ganz et al

Another detailed study of both fan wake turbulence and the associated fan rig noise is that reported by Ganz et al [16], who analyse the measured wakes in a Boeing 18-inch fan rig broadband noise test. This is a wide-ranging and comprehensive investigation in which many turbulent and mean wake results are presented. The Boeing 18-inch fan rig from the Boeing Low-Speed Aeroacoustic Facility is used in an attempt to identify and quantify the mechanisms by which fan broadband noise is produced. The inlet of the rig is cylindrical and contains a boundary layer suction system which can remove part of or the complete inlet boundary layer. Three rotor blade tip gaps were investigated (0.5%, 0.8%, and 1.1% with respect to the mid-chord blade height). The fan stator vanes are removable and a number of stator sets of varying blade number are investigated to increase understanding of the effect on the fan broadband noise of the number of vanes, stator solidity, etc. Two axial stator locations are used. Blade loading is also adjustable by the use of a throttle, with the rotor subjected to three loading levels, including high loading just below stall, medium loading at the design speed, and low loading near choke. Results pertinent to this thesis are discussed in Appendix B. Of particular interest here are the results describing the evolution of rotor mean wakes with downstream distance. However, with respect to this thesis, the most important results are those concerning the turbulent wakes and acoustic measurements. These are summarised below.

Turbulence measurements are taken with two hot-wire anemometer probes in the fan duct between the rotor and stator vanes. These are cross-wire probes that can measure the three unsteady velocity components as well as the mean flow velocity and angle. Ganz et al measured the turbulence intensity at various radial positions in the fan duct, at an axial position equivalent to the forward stator position. Here the turbulence intensity is found to be less than 1% between the rotor wakes, and between 4% and 6% in the wake cores. These levels are similar to those used in the parameteric studies performed in Chapters 6 and 7 (the turbulence inputs to the broadband noise model of Chapters 6 and 7 are derived using the Gliebe [21] wake correlations, discussed above). Ganz et al find the streamwise turbulent component to be largest in the centre of the wake (position of maximum wake mean velocity deficit), the transverse turbulent component to be its maximum near the blade tip, and the radial

turbulent component to be maximal between the wakes near the tip. However, the strongest turbulence component overall is the streamwise component near to the outer wall.

Ganz et al find that the rotor drag coefficient (and therefore momentum thickness), wake width and width of high turbulence intensity region, and turbulence length scales increase with fan loading. Higher fan loadings increase the turbulence intensity near the tip. This is due to radial migration of turbulent flow features towards the tip, and the interaction of a stronger tip vortex with the casing boundary layer. Only small differences are found between the turbulence intensity of all three components, except near the wall regions of the rotor hub and tip. This increase in turbulence intensity and length scale at the tip is calculated using the Gliebe correlations using the increased rotor wake momentum thickness as input data, and therefore do influence the turbulence parameters input to the broadband noise model in the second parametric study (Chapter 7).

The turbulence component perpendicular to the stator vanes is predicted to be the most important in the generation of fan broadband noise. The distribution of the tangential turbulence component across the wake is nearly symmetric, unlike the streamwise and radial components which exhibit a peak on the suction side of the rotor blades.

Ganz et al also present far field and induct acoustic measurements. A novel feature of this investigation is that Ganz et al separate fan noise sources into their sub-components, of rotor noise, boundary layer noise and stator noise sources. A typical source breakdown example can be seen below in Figure 3.3.2-1, for the aft radiated noise generated by the fan at 55% speed.

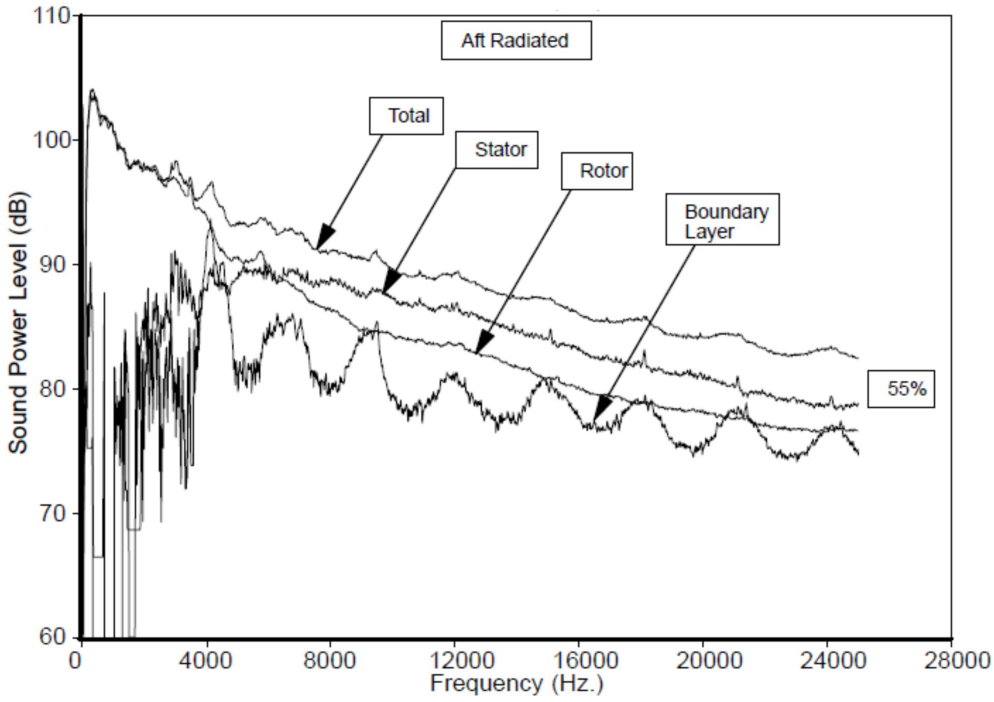

Figure 3.3.2-1 – Aft radiated sound power, fan noise sub-source breakdown, 55% shaft speed [16]

At lower frequencies, below 5 kHz, rotor-alone noise is clearly the dominant source. It appears to be the sole contributing factor at very low frequencies, though this frequency region may be contaminated by rig noise. Ganz et al found that the rotor-alone noise source increases with approximately the 6^{th} power of velocity, suggesting it is of dipole origin. Interaction between the rotor and the outer wall boundary layer generates noise whose spectrum consists of broad hay-stack type tones centred on multiples of the blade passing frequency. This noise source is removed by using the suction mechanism to take away the boundary layer.

Clearly the broadband noise due to rotor-stator interaction is the dominant subsource above approximately 5 kHz at this fan speed. As this is the dominant source it has been chosen for investigation in this thesis. Ganz et al find that the stator noise due to interaction with the rotor blade wake is only weakly dependent on blade loading, with a 3dB change in sound power for a $\pm 10\%$ change in fan pressure ratio. This level of noise change with pressure ratio is very similar to the results predicted in Chapter 7 of this thesis. Ganz et al find that the sound power increases 'nearly linearly' with the number of stators. This variation is considered in more detail in Chapter 7, where a linear increase in upstream propagating sound power with the number of stators is found, although the downstream propagating sound power increases more slowly with the number of stator vanes V. Ganz et al speculate that increasing the stator solidity appears to cause a more rapid fall-off of rotor noise, although more data for different stator sets is needed to fully understand these effects. Ganz et al therefore address several questions concerning the effect of stator cascade geometry on interaction noise, specifically:

- Does the solidity effect increase at even higher solidities?
- How is the peak frequency related to chord and spacing?
- Are these effects predicted by the fluctuating-lift models under development by other researchers?

These questions are discussed in Chapter 6 of this thesis in which the effect of stator count and solidity on the predicted broadband noise is investigated.

Additionally, Ganz et al find that the OASPL (Overall Sound Pressure Level) increases with approximately the 6^{th} power of fan speed. A similar test on the velocity scaling law was performed using the broadband noise model, the results of which are shown in Chapter 7. The effect on rotor-stator broadband noise due to a change in shaft speed along a working line was found to be primarily due to the change in rotor wake Mach number of the flow impinging on the stator vanes. In the first parametric study of Chapter 6, the effect of flow Mach number impinging onto the stator vanes is found to be less than the 6^{th} power law for low frequency sound power (approximately the 4^{th} power), although varies as approximately the 6^{th} power for high frequency sound power. The high frequency

results are therefore in general agreement with the findings of Ganz et al, with the difference possibly due to 3-dimensional effects not captured by the 2-dimensional broadband noise model used in this thesis.

3.3.3. Fan noise source diagnostic test

More recent (1999) experimental campaigns that investigate experimentally both the fan noise and turbulence in the flow around the fan have been carried out as part of the Fan Noise Source Diagnostic Test. This test was carried out in the NASA Glenn Research Centre's 9 by 15 foot low speed wind tunnel on a 22 inch scale-model representative turbofan bypass stage. The principle objective of this project was to study the source mechanisms of noise in a modern high-bypass-ratio turbofan engine, through aerodynamic and acoustic measurements.

Podby et al [39] present measurements taken during testing of two 22 inch diameter turbofan models, in order to assess the differences between the two models. Laser Doppler Velocimetry (LDV) is used to measure the axial and tangential components of velocity. Results are presented for both the mean wake and tone noise, and the turbulent wake and broadband noise. The noise measurements referred to in this paper are those presented by Woodward et al in [46]. Of the results presented in these papers, only the turbulent wakes and broadband noise will be discussed.

Podboy et al investigate experimentally two rotors, both of which produce approximately the same design pressure ratio, though one rotor operates at a 10% higher design speed. Woodward et al [46] indicate that the slower rotor investigated is representative of an early GE90 engine fan. The increase in shaft speed while maintaining pressure ratio is a similar situation to the shaft speed investigation described in Chapter 7. The results of the Podboy investigation are not presented to the level of detail as those of Ganz et al [16]. However, some similar findings are common to both reports. Podboy et al find that increasing the speed of a rotor increases the turbulence intensity, and reduces the thickness of the turbulent regions in the wake. This increase in turbulence intensity occurs more rapidly in the tip region than the blade wake, most likely due to the stronger tip vortex and the generation of turbulence near to the casing wall. Compared to the slower rotor, the rotor operating at the same pressure ratio but 10% higher fan speed had thicker wakes, and less turbulent tip flows, due to the decreased turning required of the rotor blades (an introduction to basic fan performance theory, including rotor turning and velocity triangles, can be seen in Appendix D). However, at a given operating condition the two rotors generate comparable peak levels of circumferential turbulent velocity. The turbulence generated by the rotors diffuses and dissipates as it is convected downstream, although this is slower in the tip region. The persistence of turbulence in the tip region may be due to continuous turbulence production

near the wall boundary layer causing unsteadiness that becomes increasingly important as the wake flow convects downstream.

The acoustic measurements corresponding to the Podboy flow measurements are presented by Woodward et al [46]. Far field acoustic pressure spectra are presented for the two fans mentioned previously with three stator sets. These are: cut-off radial (for the rotor BPF tone), cut-on radial, and cut-on swept. The test investigates the effect of changes in rotor tip design speed, unit area loading, tip clearance, and stator configuration. Woodward et al also include a rotor-alone configuration in which no stators are present, in order to assess their contribution to the overall noise levels. However, Woodward et al present their noise measurements in terms of Effective Perceived Noise Levels, and concentrate the results on changes in blade passing frequency and multiple pure tones. Few conclusions on the broadband noise are presented. Compared to the rotor-alone configuration, inclusion of the cut-on stator set (54 vanes) contributed approximately 5 EPNLdB to the measured broadband noise. The cut-on stator set (26 vanes) produced less broadband noise by virtue of containing fewer vanes. Broadband noise was reduced still further by sweeping the stators. The swept stator set produced the lowest noise levels, and although cut-on, the benefits of stator sweep exceeded the tone noise penalty.

Comparison of the noise data for the three stator sets shows that the perceived noise levels can be lower for a particular rotor and stator combination, even though tone noise does not decrease correspondingly. Sufficient reductions in broadband noise can control the EPNL levels. Woodward et al conclude that designing a rotor to operate at a higher tip speed with reduced unit area loading may significantly reduce overall fan stage noise, especially at subsonic rotor tip speeds. However, as mentioned previously this conclusion is made based on the rotor tone noise sources and therefore cannot be directly applied to the results of the second parametric study of this thesis, presented in Chapter 7 which related to broadband noise.

Recent experimental work into the measurement of fan stage turbulence and its associated noise measurements has been carried by Jurdic et al [28], who compare the modelled and measured fan broadband noise on a low speed fan rig. Although this paper does provide some limited measured acoustic and aerodynamic results, this paper is discussed in the following Section 3.4, due to the inclusion of a modified version of the same broadband noise model in this thesis.

3.4. Models for the prediction of fan broadband noise

The downstream stators onto which a turbulent wake impinges have been modelled as a series of non-interacting airfoils, and as a cascade where blade-to-blade interaction effects are included. Although the early rotor-stator interaction models concentrated on using single airfoil theory (for example the work of Amiet [4] and [5]), the broadband noise model used in this thesis is a cascade noise model.

3.4.1. Creation of the broadband noise cascade model – LINSUB code

One of the first models to predict the response of a cascade to torsional vibration, incoming acoustic waves, or convected wake velocity perturbations, is that of Smith [43]. Smith has proposed a model that allows the calculation of the unsteady blade lift and moment, generated acoustic waves, and shed vorticity when a cascade of blades are subjected to bending or torsional vibrations, incoming acoustic waves, or convected vortical velocity perturbations. This model assumes subsonic, isentropic, 2-dimensional flow over a cascade of flat plates of negligible thickness. It neglects viscous effects, assumes that all perturbations of the uniform mean flow are small, and that unsteady aerodynamics at any particular blade are duplicated at all other blades with a constant phase angle between adjacent blades. This model is found to be accurate at 0^o angle of attack, although accuracy breaks down when steady blade loading is introduced. Whitehead [45] expands upon the work of Smith, and presents a theory to predict the estimation of the vibration characteristics of real blades in addition to the acoustic response. Whitehead has produced the code LINSUB to predict these responses, which is a freely available Fortran code whose acoustic components are based on the Smith model. The LINSUB model is that chosen for use in the broadband noise parametric studies presented in this thesis (Chapters 5 to 7).

3.4.2. Expansion of the cascade noise model - Cheong et al

The LINSUB code was recently used by Cheong et al [11] to predict the sound power produced by a cascade. A critical frequency is defined in which cascade effects due to the interaction between neighbouring aerofoils are such that the unsteady blade loading between adjacent blades are correlated. Above the critical frequency the sound power is proportional to the number of blades and hence radiates incoherently. An analytic expression is derived for the acoustic power spectrum above the critical frequency. Agreement with the exact solution is found to be excellent. This sound power model and approximate expression are discussed further in Chapter 5. In the broadband noise investigations of this thesis the critical frequency is used to separate the predicted sound power into low and high frequency bands, thereby allowing consideration of the variation of low and high

frequency sound power. Cheong et al also performed a parametric study, investigating the effect of varying number of vanes, cascade solidity, Mach number and stagger angle. The parameteric study is extended in this thesis, investigating the effect of varying turbulence intensity and turbulence length scale, in addition to those parameters whose influence was investigated by Cheong et al. The results of this extended parametric study are presented in Chapter 6, and provide sound power scaling laws that allow predictions to be made of the changes in sound power due to changes in the cascade boundary conditions.

3.4.3. Predictions using the cascade noise model - Jurdic et al

Jurdic et al [28], present a comparison between predicted and measured fan broadband noise on a low speed fan. The broadband noise model is an extension of the 2-dimensional LINSUB model used by Cheong et al [11]. The incoming turbulent wake is decomposed into a mean wake profile, plus a random function to model the random turbulent fluctuations of the wake. The turbulence is assumed to be isotropic and homogenous, and requires the turbulence intensity and integral length scale as input parameters. These inputs are provided by both CFD RANS computations, and experimental measurements. The experimental measurements were performed on a rig whose fan stage consists of a 24-blade rotor and a 16 vane stator. Cross-wire hot-wire probes were used to measure the flow velocity components in the rig inlet, and at two axial positions between the rotor and stator. As found by Ganz et al [16] and Podboy et al [39] the wake streamwise mean velocity is relatively constant in the mid-span region, however small variations can be seen in the hub and tip regions. The circumferential and radial mean velocity components are of much lower magnitude than the streamwise component. The circumferential turbulence intensity in the measured wake centreline is approximately 6% near the hub, 2% in the mid-span region, and increasing to 10% near the tip. These values are similar to the measurements of Ganz et al, although large secondary flows in the hub region present in the DLR rig are not as observed in the results of Ganz et al [16], for which tip vortices are more apparent. Comparison of the measured and predicted acoustic power spectra show that the model under predicts the sound power by approximately 1.5dB.

3.4.4. Extension of the cascade model to 3-dimensions - Lloyd and Peake

Lloyd and Peake have extended the LINSUB code to 3-dimensions [31] to allow for oblique gusts. They consider the distortion of the rotor wake in the mean swirling flow downstream of the fan, and also introduce dissipative effects. This paper also considers the interaction of this gust with the downstream stator cascade. Stator lean and sweep effects are also included. The full 3-dimensional solution is obtained by mapping the 3-dimensional inputs to the 2-dimensional parameters of the

LINSUB code, and utilising strip theory. The final sound power spectra predicted by Lloyd and Peake is lower than that predicted by the 2-dimensional noise model. The inclusion of a 3-dimensional swirling gust striking a stator vane introduces spanwise cancellation of modes, this effect is not included in the 2-dimensional model. The 2-dimensional model assumes a normal-incident gust that strikes all radial strips along the vane simultaneously, and does not include the radial mode cancellation, therefore over-estimating the blade response.

3.4.5. Effect of swirl, loading, and stagger angle on predicted cascade broadband noise - Atassi and Vinogradov

Atassi and Vinogradov [9] present predictions of the aerodynamic and acoustic response of a three-dimensional loaded annular cascade subject to impinging turbulence in a swirling flow. They state that 3-dimensional effects and mean flow swirl change the physics of the scattering in three ways; by modifying the number of acoustic modes in the duct, by changing their mode shapes, and causing a significant amplitude and radial phase variation of the incident turbulence. Comparisons between four cases are presented to assess the effect on acoustic response of changes in flow swirl, loading etc. The first three cases have arbitrary cascade geometries and inflow conditions, however the fourth case models the geometry and inflow conditions of the Source Diagnostic Tests mentioned above.

- The first comparison is un-swirled flow with 30 degree swirled flow. The inclusion of swirl increases the low frequency noise level by 3dB, reduces the noise of the mid-frequency range by approximately 3dB, and the spectra converge at very high frequency.

- The second comparison is between an unloaded cascade with 30^0 stagger angle, and a loaded cascade providing mean flow turning, with 12^0 of stagger angle. The loaded cascade generates a higher noise level (approximately 3dB higher) at mid-frequencies compared to the unloaded cascade, though at high frequencies the noise level of the loaded cascade drops below that of the unloaded cascade before they both come together again.

- Thirdly the Source Diagnostic Test geometry, which is subjected to radially varying blade loading, is compared to a loaded cascade providing mean flow turning. The non-uniform loading influences the acoustic power most in the mid-frequency range, reducing the sound power by a maximum of 4dB.

- For the fourth case, the 3-dimensional code is compared with a 2-dimensional calculation for conditions at the mean radius of the cascade. The 2-dimensional code predicts higher sound power a low frequencies, and the 3-dimensional code predicts higher sound power at mid and high frequencies, though the differences between the two codes do not exceed 2dB at any frequency. In addition the fact that the spectra predicted by all cases converge at very high frequencies suggests that there is less dependence on geometry and inflow conditions at high frequencies.

Finally, Atassi and Vinogradov perform a full 3-dimensional calculation for comparison with results of the Source Diagnostic Test for the low count stator set at approach, with data adjusted to give the required outputs at the exhaust. The turbulence intensity and length scale inputs from the experimental

tests are comparable in magnitude to those measured by Ganz et al. Their 3-dimensional model over-predicts the sound power at low and mid-frequencies by approximately 2dB, which may be due to an error in the turbulence intensity input parameters.

3.4.6. Effect of turbulence model on predicted broadband noise - Atassi and Logue

Atassi and Logue [8] investigate the sensitivity of the broadband sound power prediction to different turbulence models. They state that at lower frequencies the difference between using the Liepmann and Von Karman models for the wavenumber spectra of turbulence velocity, is approximately 2dB. This difference reduces to less than 1dB at higher frequencies. Atassi and Logue conclude this difference is not considered significant for the calculation of acoustic spectra. Atassi and Logue also find that the sound power increases with Mach number, and this increase is more rapid at high frequencies. Their results are in agreement with the results described in Chapter 6 of this thesis, however they do not specify a sound power scaling law.

3.4.7. Effect of lean and sweep on cascade broadband noise, an alternative parametric study – Glegg and Hanson

Glegg [20] has also developed an analytical expression for the tone noise response of a 3-dimensional rectilinear cascade of blades with finite chord, excited by a harmonic 3-dimensional gust. Spanwise wave numbers and cross flow effects are included. The expression due to Glegg computes the unsteady blade loading, acoustic mode amplitudes and sound power. The blade loadings at low frequencies are reduced by 3-dimensional effects, and non-zero spanwise wave numbers reduce the acoustic radiation at high frequencies. There is no radiation when the phase speed of the harmonic gust along the leading edge is subsonic.

Hanson [26] has extended Glegg's single frequency solution to include a broadband turbulence input. Radial and blade-to-blade variations of turbulence statistics are treated along with lean and sweep of the cascade. A parameter study is performed that allows the analysis of sound power trends with Mach number, vane count, turbulence length scale and intensity, and lean and sweep. Hanson has found that the sound power increases approximately in proportion to the number of vanes. This linear increase with the number of vanes is also found for the upstream propagating sound power in Chapter 6.1.1, although downstream propagating sound power is found to increase with vanes at a slower rate, at approximately $V^{0.8}$, where V is the number of vanes. Hanson found that vane sweep eliminates tones, and provides broadband noise reduction over a wide range of frequencies. A noise reduction of 1.1dB is found for an angle of sweep of 30^o. Adding lean to the sweep provides further improvements; 30^o of

both sweep and lean provides a 3.9dB improvement. The effects of lean and sweep cannot be considered in the parametric studies of this thesis. Again, Hanson found that the sound power of the downstream spectrum increases approximately as the Mach number to the power of 5. This Mach number scaling power law is between the low and high frequency band sound power variations with Mach number discussed in this thesis (Chapter 6.2).

The beneficial effects of lean and sweep on fan noise proposed by Hanson were also found experimentally by Woodward et al [47]. Three stator sets were investigated; two radial stator sets at two axial positions, one stator set swept by 30^o, and one stator set swept and leaned by 30^o. It was found that improvements for a hypothetical aircraft and flight path would be approximately 3 EPNdB (Effective Perceived Noise in dB). Swept and leaned stators are preferable for reducing tone and broadband noise, compared to shifting the radial stator sets further downstream from the rotor. Moving the vanes may degrade aerodynamic performance, and increase the overall aircraft weight. Sweep is predicted by Hanson to be more beneficial at take off, and lean more beneficial at approach, and combining these should have overall benefits to the overall noise reduction.

3.4.8. Use of RANS turbulence inputs - Nallasamy and Envia

Nallasamy and Envia [37] present a broadband noise model that uses RANS computed rotor flow turbulence as an input to an analytic model of broadband rotor-stator interaction. These are compared to measured results. Good agreement is found, demonstrating the validity of using simple integral flow parameters obtained from CFD to provide inputs to such models. A coupled structural/aerodynamic analysis system is used to compute the fan 'running' shape. A number of parameters are investigated including absolute mean flow Mach number, vane chord and number of vanes, and stagger angle. An unexpected result presented by Nallasamy and Envia is that the sound power varies as the number of vanes squared. This is not consistent with the results predicted by Hanson [26], or the parameter study performed in Section 6.1.1 of this report. Furthermore, evidence to support this finding is neither found in the Ganz study [16], nor explained by Nallasamy and Envia.

3.5. Fan Nozzle Area Effects

Early jet aircraft were very noisy due to the high jet velocities of their exhausts. The introduction of high bypass ratio engines produced a large reduction in aircraft noise by moving a larger mass of air more slowly, thereby reducing the jet velocity. Further diameter increases may be incorporated in the future using either ultra-high bypass engines, or alternatively engines with variable area nozzles.

Variable area nozzles are a technology that can influence many characteristics of the performance cycle of an aircraft engine, including specific fuel consumption, turbine entry temperature, and the rotational speed of components such as the fan and compressor stages. While performance considerations are likely to drive the use of a variable area nozzle, noise benefits may also be achievable due to changes in jet velocity and fan rotational speed. The final investigation presented in this thesis concerns the noise effects of variable area nozzles.

Several experimental studies have recently been carried out considering the effects of further nozzle diameter increases. Two of these are based on the findings of the second entry (SDT2) Fan Broadband Source Diagnostic Test, carried out at NASA Glenn.

3.5.1. Noise benefits of increased exhaust nozzle area - Woodward and Hughes

Woodward and Hughes [48] consider the noise benefits of increased fan bypass nozzle area. Three nozzle areas are considered. The first is a nozzle whose diameter is chosen to provide maximum stage performance at cruise. The second is the baseline area +5.4% sized to simulate the performance at the stage design point conditions. The third is the baseline area +10.9%, whose diameter is chosen to provide the maximum weight flow with fixed nozzle at sea level conditions. The +5.4% nozzle area increase was found to provide a 2dB noise reduction at speeds up to cutback, and approximately 1dB reduction at higher shaft speeds. The larger +10.9% nozzle area provided a 3dB noise reduction at lower shaft speeds, 2dB at intermediate shaft speeds. However an increase in noise at higher shaft speeds was found, which was assumed to be due to degrading fan performance at the higher speeds. These noise reductions were observed at all measured sideline angles. Woodward, Hughes and Podboy [49] further analysed the effect of varying nozzle area on the turbulent rotor wakes, using laser Doppler Velocimetry to provide flow measurements downstream of the rotor. They show that the total turbulent velocity decreases with increasing nozzle flow, postulating that this may explain the reduced rotor broadband noise.

The reductions in fan noise described above due to increasing nozzle area demonstrate that an optimal nozzle area is achievable for different flight cases, as confirmed in the results shown in Chapter 9. This can be performed using a computational optimiser, and forms an ideal test case to evaluate the use of the engine noise model currently used by Rolls-Royce as an optimiser for engine noise.

Rig measurements are central to this thesis. Numerous sets of rig measurements are used to verify model predictions, attempt to obtain broadband noise correlations, and to provide inputs to the variable

area nozzle study. The preparation of these rig measurements for use in the subsequent Chapters of this thesis is discussed below.

Chapter 4

Analysis of a Rig Noise Measurement Database

A central theme of this thesis concerns rig noise and analysis. The following chapter is separated into two sections, 4a and 4b, describing two separate rig noise investigations of a measured rig noise dataset. Both investigations described within this chapter make use of proprietary rig noise measurements. Where necessary these measurements are described in Chapter 4 of Appendix X.

Chapter 4a describes the various fan rig measurement positions, and how the individual noise sources are separated. These separated results are analysed to increase understanding of the individual fan noise sources. Both tone and broadband noise measurements in forward and rearward arcs are plotted against fan pressure ratio and mass flow on working line diagrams.

Chapter 4b presents a statistical analysis of rig noise measurements from many rig datasets, and the relationship between rig measured fan broadband noise and flow and rig predictors is investigated.

4. a - Preparation, processing and interpretation of rig measurements

The first section 4.1 of the following chapter specifies the rig measurement positions. This is followed by a description of typical noise measurement results, and how they are separated into particular noise sources. As measurements are typically taken as decelerations along a working line, a procedure for interpolation along, and extrapolation between, working line measurements is developed.

4.1. Fan rig hardware and description of measurements

The results of a number of rig noise measurement campaigns are used in this thesis. A number of modifications can be made to these fan rigs by varying both the architecture and performance in order to investigate the noise dependency on various engine parameters.

The noise measurements for the inlet are taken in the far field, while bypass measurements are taken in duct. A schematic of the rig geometry used to perform these experimentations is seen below in Figure 4.1-1, with further detail found in Section 4.1, of Appendix X.

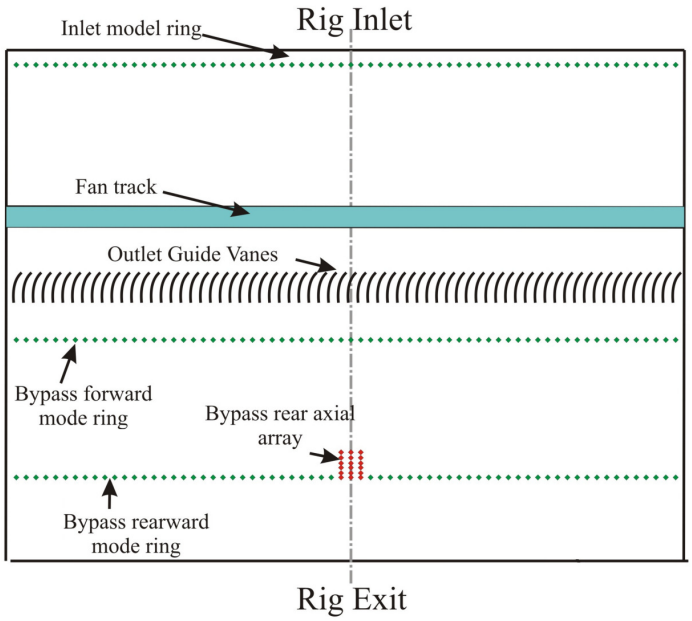

Figure 4.1-1 - Test rig schematic, unrolled

There are three main measurement positions in the bypass duct of the rig. Two mode-ring type microphone distributions are positioned downstream of the fan stage. The first of these is positioned close to the outlet guide vanes, upstream of any bypass duct liner. The second is further downstream, past any bypass duct liner, near the test-section exit. A small linear array of microphones is also located at an equivalent avail position to the second mode-ring. This linear array of microphones is arranged in parallel to the rig centre-line, on the bypass duct outer wall. The measurement results shown in this public thesis document were taken from this axial measurement array.

The fan rig tests whose results are used in this thesis generally measure acoustic data using two different methods. To measure noise data at steady state, the fan rig is run at a particular speed to meet a specified test point. After allowing shaft speed to stabilise, Sound Pressure Level (SPL) measurements are taken both in the fan rig inlet and the bypass duct. The measurement locations used are indicated in the rig schematic shown in Figure 4.1-1.

Alternatively, a fan shaft speed ‘decel’ (deceleration) is performed. In this situation the core nozzle exhaust area is maintained, while the bypass exhaust area is varied to allow a fan working line to be traced via a shaft speed deceleration. Shaft speeds are recorded in terms of ‘Engine Order’ EO via a tachometer attached to the fan, measuring revolutions per minute.

Fan speed must be corrected for ambient temperature to allow comparison between measurements taken on different days. This correction is made using the following equation:

$$RPMc = RPM\sqrt{T_{ref}/T} \qquad \text{Eq (4.1-1)}$$

Where $RPMc$ is the corrected RPM, T_{ref} is the temperature of a standard ISO day (15^0 C), and T is the ambient temperature measured at the time of test. Frequency can then be calculated using Eq (4.1-2) below

$$freq(Hz) = \frac{RPMc}{60} EO \qquad \text{Eq (4.1-2)}$$

A typical working line schematic can be seen in Figure 4.1-2. These working lines are numbered for identification, with working line 1 having the highest pressure ratio, and working line 6 having the lowest pressure ratio. Working line 6 corresponds to the rig being run with the exhaust nozzle fully open.

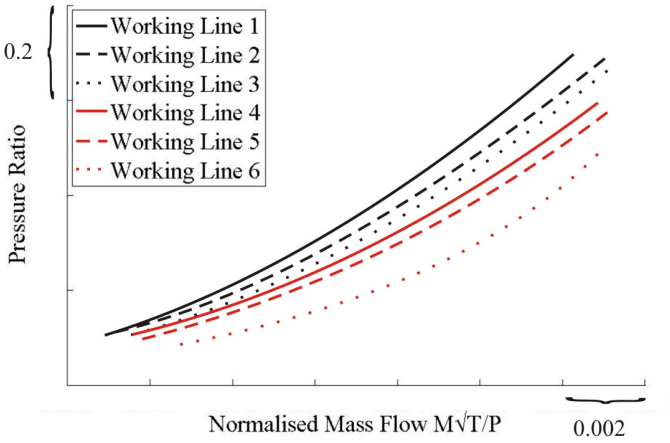

Figure 4.1-2 – Plot of typical fan working lines

4.2. Extraction of rig noise sources

A number of fan rig sources are investigated throughout this thesis. These are defined below:

- Blade Passing Frequency – BPFs 1, 2, 3, and 4, are obtained by extracting the required noise measurement at engine orders that are multiples of the number of blades i.e. *n* times the number of blades, where *n* is the BPF order 1, 2, etc.

- 'Buzz noise' – This is calculated as the average SPL of engine order frequencies measured below the second blade passing frequency, corrected to remove the BPF 1 tone. The BPF tones have been removed by replacing the tone SPL value with the average of the SPL values to either side.

- Broadband – These bands are termed 'BB's' in this thesis, such that *BBn* is within the frequency bandwidth:

$$(n-1)BPF \le f \le nBPF \qquad \text{Eq (4.2-3)}$$

where *BPF* is the blade passing frequency, *f* is the frequency, and *n* is the integer *n=1, 2, 3, 4*. These frequency bands are defined in Figure 4.2-1 below, and are located between successive blade passing

frequency tones. Note that the engine order limits of these blade passing frequency regions are slightly offset from the BPF engine orders themselves, to avoid any contamination. The BB range engine order limits can be seen in Section 4.2, of Appendix X.

The broadband regions (BBs) are calculated for each working line using the following procedure: Data is extracted from the rig measurements at every odd number of 0.5 engine order (0.5, 1.5, 2.5, etc.), to avoid any tones being present at integer engine order values. The noise measurements are then interpolated between adjacent data points to provide new values for each integer engine order. Broadband values are then calculated as the average sound pressure level in the specified engine order ranges.

The frequency ranges of these rig sources is defined below in Figure 4.2-1 for a typical shaft speed.

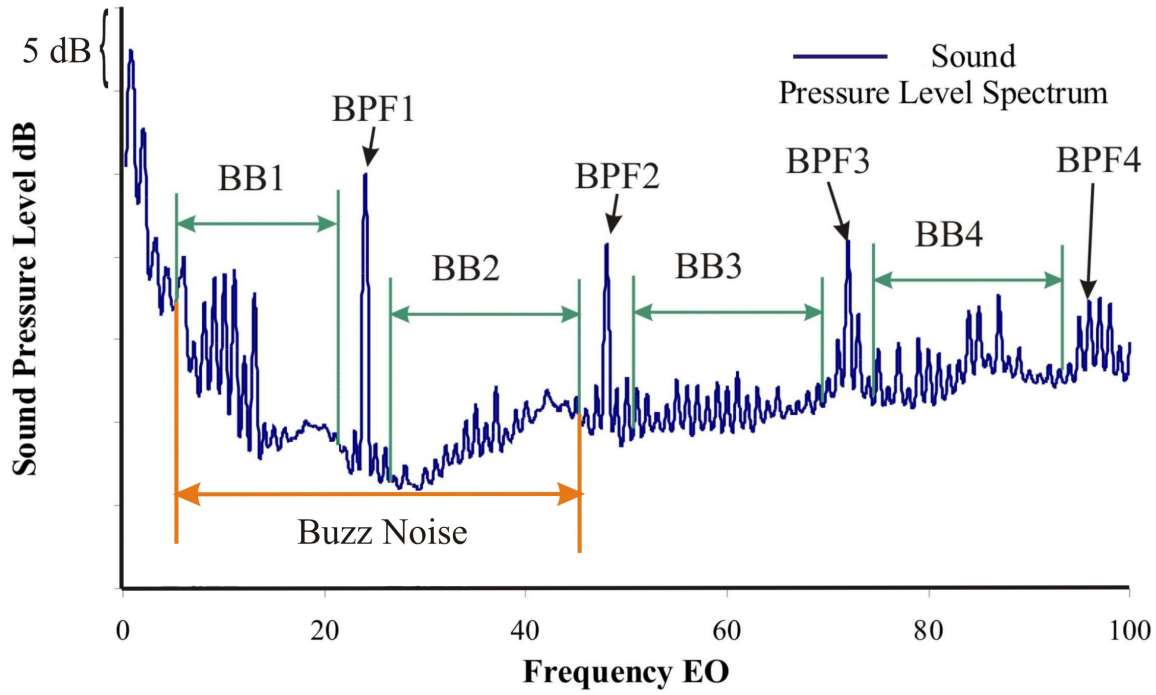

Figure 4.2-1 – Definition of fan source frequency ranges

The noise sources defined above are used in both the derivation of fan noise correlations described in Chapter 4b, and the variable area nozzle investigation of Chapters 8 and 9.

4.3. Interpolation of noise measurements

The noise sources specified above are deduced from measurements at each test point along a working line. A polynomial is then fit through this data to provide a smooth estimate of the noise data at all points along the working line. These working line polynomials are then extrapolated to estimate the noise between working lines. This creates a surface of noise versus pressure ratio and normalised mass flow which covers the measured data domain. A representative result of this procedure can be seen in section 4.4 below, for one noise source. The complete results for all noise sources are shown in Section 4.4 of Appendix X. Note that noise measurements were not extrapolated beyond the measured limits of working lines 1 and 6, as these working lines are near the surge and stall limits of the fan. Any extrapolation of noise sources into these regions would be unreliable.

4.4. Variation of Engine 2 rig noise sources with pressure ratio and normalised mass flow

This section presents a typical plot of a rig noise source chosen from those listed and defined above in Figure 4.2-1. This style of visualisation is not in common use. The noise source chosen is broadband noise in the rearward arc, plotted versus pressure ratio and normalised mass flow. Presentation of the noise measurements in this manner allows insight to be gained in how each fan rig noise source varies with pressure ratio and normalised mass flow. It should be noted that during rig tests the core exhaust area and therefore blockage is maintained constant. This blockage effect does not occur in the same way for the fan stage of a real engine, though the difference does not have a large effect on the measured noise results.

4.4.1. Broadband noise – Rearward Arc

The representative fan noise source considered here is the broadband noise propagating in the rear arc, i.e. measured downstream of the OGVs. This can be seen in Figure 4.4.1-1, with the measured broadband noise being averaged over BBs 1, 2, 3, and 4. These measurements were taken from the axial measurement array, whose location is shown in Figure 4.1-1.

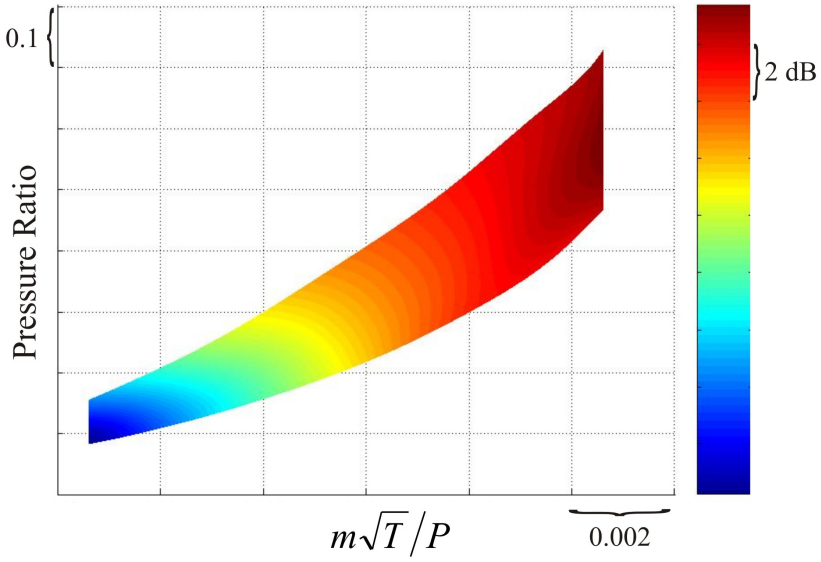

Figure 4.4.1-1– Broadband Noise, Rearward arc, SPL

Rear arc broadband noise is typically higher than that propagating in the forward arc. This may be due to a combination of the effects of rotor blockage and convective amplification. Figure 4.4.1-1 indicates that to reduce broadband noise in the rear arc, shaft speed must be reduced to a lower pressure ratio position on the working lines.

4.4.2. Rig data presentation summary

As mentioned previously, the complete results of the above section 4.4 can be seen in Chapter 4a, section 4.4 of Appendix X. The rig-measured SPL data presented above will later be used in the prediction of rig noise level changes in the study on the use of Variable Area Nozzles of Chapters 8 and 9. In general, reducing pressure ratio at a fixed mass flow will reduce most of the noise sources under investigation. Noise is also found to reduce as the performance point moves down a working line, as fan speed is reduced.

Chapter 4b now describes a statistical analysis of the rig noise measurement database, deriving regression correlation equations base on the relationships between noise measurements and fan rig flow and performance predictors.

4. b Creation of correlations to predict rig broadband noise

Chapter 4b discusses the results of an investigation into a large dataset of experimentally measured noise data from a fan rig. There are two aims for this investigation.

4.5. Aims of statistical analysis of rig noise measurement database

The first aim is to gain a greater physical understanding of fan broadband noise generating mechanisms by investigating the relationships between the experimentally measured noise data and the corresponding aerodynamic and fan rig performance data. Note that nearly all of this aerodynamic and performance data is estimated from a simple 'throughflow' code. The objective is to determine the important parameters on which fan broadband noise is mostly correlated, which could include for example fan pressure ratio, and mass flow.

Initially, the second aim of this investigation was to derive noise prediction equations that incorporated more physics of the broadband noise generation mechanisms compared to the very simple equations currently used within the noise model[2]. Unfortunately, for reasons explained in Section 4.11 below, this was found not to be possible with the data sets available. Instead, simple linear regression equations are derived from the noise data using Least Squares analysis, whose aim is to fit the noise data by linear equations involving the statistically important parameters. The resulting regression equations are linear equations of the form:

$$PWL_j = \sum_i^N p_{i,j} a_i \qquad \text{Eq (4.5-1)}$$

where PWL_j is the sound power level (dB) in a specified frequency bandwidth, with the subscript j denoting the j^{th} fan speed. The predictor variable is $p_{i,j}$, with the predictor number denoted by i. The summation is over the number of predictors in the regression equation, N. Finally, a_i is the dimensional weighting coefficient for the i^{th} predictor.

Note that the predictor p can be a physical flow, or performance, parameter, such as fan Pressure Ratio or fan efficiency. Alternatively, p can be a non-physical index (1, 2, 3, etc), accounting for a change in

[2] In this chapter the term 'noise model' is used for a total engine and aircraft noise prediction model.

a covariate[3], such as, for example, designating whether the fan blade is of Engine 2, Engine 3, or Engine 5 form. The covariates present within this analysis are discussed further below. It is important to note also that no attempt is made to ascertain the power law of the parameter under investigation. Therefore all parameters in Eq (4.5-1) will be assumed to affect broadband noise levels linearly.

Eq (4.5-1) can be rewritten in Matrix form as:

$$\mathbf{w} = \mathbf{P}\,\mathbf{a} \qquad \text{Eq (4.5-2)}$$

The elements of **w** contain the set of J pre-processed broadband sound powers (PWL dB) for a specific frequency band. The j^{th} term represents the j^{th} shaft speed at which the noise measurement was taken.

The matrix **P** is the $J \times N$ predictor matrix made up of the N independent predictor variables (including flow, performance and covariate predictors), at each shaft speed. Each of the predictors under investigation at different speeds forms one column of the matrix. These shaft speeds are matched to those of the measured noise data for an equivalent performance point on the fan rig. The predictor matrix and measured noise vector therefore include both noise and performance data for all available performance points. A representative example of these three matrices is displayed in Eq (4.5-3) below.

$$\begin{bmatrix} PWL_{n,1} \\ PWL_{n,2} \\ PWL_{n,3} \\ PWL_{n,4} \\ \vdots \\ PWL_{N,J} \end{bmatrix} = \begin{bmatrix} P_{1,j_1} & P_{2,j_1} & P_{3,j_1} & \cdots \\ P_{1,j_2} & P_{2,j_2} & P_{3,j_2} & \cdots \\ P_{1,j_3} & P_{2,j_3} & P_{3,j_3} & \cdots \\ P_{1,j_4} & P_{2,j_4} & P_{3,j_4} & \cdots \\ \vdots & \vdots & \vdots & \vdots \\ P_{1,J} & P_{2,J} & P_{3,J} & P_{N,J} \end{bmatrix} \begin{bmatrix} a_1 \\ a_2 \\ a_3 \\ a_4 \\ \vdots \\ a_N \end{bmatrix} \qquad \text{Eq (4.5-3)}$$

where PWL_n denotes the measured sound power in the n^{th} frequency band ($n=1,2,3,4$) of interest, and P_{1,j_1} is predictor 1 at the first fan speed j_1, P_{2,j_4} is predictor 2 at the fourth fan speed j_4 etc. In Eq (4.5-3) the vector **a** is the vector of regression coefficients of length N. The derivation of the optimal values that minimise $\mathbf{a_0}$ is the target of this regression study. The vector $\mathbf{a_0}$ is derived using Least squares analysis, as described in the following section.

[3] A covariate is a factor that is a feature of the rig, and should be taken into account in the analysis. It is a predictor variable that changes continuously between rig noise tests, but not within a noise data set.

4.6. Statistical tools used to create rig broadband noise correlations

This section introduces the statistical approaches used in this chapter to investigate the experimentally measured rig noise dataset. These tools allow an increased understanding of the physics of the broadband noise generating mechanisms in the rig noise dataset. They also produce the linear regression equations, of the form of Eq (4.5-1), to predict the measured fan broadband noise. The software used to perform the statistical analyses presented in this chapter was Minitab[4].

4.6.1. Least squares Analysis

In this investigation Principle Component Analysis and Cluster Analysis are used to reduce the large number of predictors *P* initially present, to a set of *N* independent predictors. This procedure is described in sections 4.6.2 and 4.6.3. However, Least Squares regression is used to derive the final regression equations using these *N* predictors and is introduced below. The final regression equations take the form of Eq (4.5-1). These regression equations form individual linear equations for the prediction of broadband noise, for each broadband region *n* in either the forward or rear arcs, and can be applied irrespective of fan type, working line, etc.

Prediction equations of the form of Eq (4.5-1) are derived to fit the large data set in a least squares sense. The difference between the observed value, and the predicted or fitted value, is called the *residual*, denoted by *r* in Eq (4.6.1-1) below:

$$r = PWL_{\exp} - PWL_{pred} \qquad \text{Eq (4.6.1-1)}$$

where PWL_{exp} is the experimentally measured sound power level, and PWL_{pred} is the predicted sound power level obtained from Eq (4.5-1). Least squares analysis calculates a regression equation through the data points so that the sum of the squares of the distances of those points from the regression line of Eq (4.5-1) is minimised, i.e. the procedure aims to minimise $\sum |r|^2$. The derivation of least squares regression is presented in Appendix H-1. The final result is shown below in Eq (4.6.1-2).

Provided that the inverse of $\mathbf{P}^T\mathbf{P}$ exists (the matrix determinant of $\mathbf{P}^T\mathbf{P}$ is non-zero), the solution of $\mathbf{a_0}$ is given by:

$$\mathbf{a_0} = \left(\mathbf{P}^{\mathrm{T}}\mathbf{P}\right)^{-1}\mathbf{P}^{\mathrm{T}}\mathbf{w} \qquad \text{Eq (4.6.1-2)}$$

[4] www.minitab.com

This procedure can be repeated to produce a regression equation for any broadband noise bandwidth, in either the forward or rear arcs.

Consideration of the magnitude of residuals is important for quantifying the 'goodness of fit' of the regression equation to the data. Residuals and their analysis in this investigation are considered in greater detail in Section 4.9.3.3.

However, before considering the residuals of the final regression equations, Sections 4.6.2 and 4.6.3 will discuss the other statistical techniques used in this investigation for interpreting the broadband noise data, starting with Principle Component Analysis.

4.6.2. Principle Component Analysis

Principle Component Analysis is used in this study to reduce the large predictor set (Matrix *P* in Eq (4.5-2)) presented at the start of the analysis, by extracting the most important underlying behavioural 'structures' within the predictor data set. Each of these structures' is a component of the overall behaviour. Separation and ordering of the most important behavioural components allows a smaller subset of predictors to be chosen that account for the maximum predictor variance using the minimum number of components.

Principal Component Analysis may be applied to either a correlation matrix (i.e. with elements that are normalised) or a covariance matrix to identify how predictors vary statistically in relation to each other. For this study the correlation matrix is used to assess which predictors are correlated and which are statistically independent.

The correlation matrix **C** has elements $c_{m,n}$ given by

$$c_{m,n} = \frac{\sum_{j=1}^{J}\left(P_{j,m} - \overline{P_m}\right)\left(P_{j,n} - \overline{P_n}\right)}{(J-1)\sigma_{\mathbf{P}_m}\sigma_{\mathbf{P}_n}} \qquad \text{Eq (4.6.2-1)}$$

where $P_{j,m}$ and $P_{j,n}$ denote any two predictors m and n, at speed j, and $\sigma_{\mathbf{P}_m}$ and $\sigma_{\mathbf{P}_n}$ are the standard deviations of the predictor vectors $\mathbf{P}_\mathrm{m}$ and $\mathbf{P}_\mathrm{n}$ respectively. The standard deviation is calculated using Eq (4.6.2-2):

$$\sigma_m = \sqrt{\frac{\sum_{j}^{J}\left(P_{j,m} - \overline{P_m}\right)^2}{J-1}} \qquad \text{Eq (4.6.2-2)}$$

where $\overline{P_m}$ is the mean of predictor P_m. The standard deviation is equal to the square root of the variance σ^2.

The vector representing a predictor P can be decomposed into the summation of statistically independent predictors Q_i, and their amplitudes V_i. This can be written as:

$$\begin{aligned} P_1 &= V_{1,1}Q_1 + V_{1,2}Q_2 + \cdots + V_{1,N}Q_N \\ P_2 &= V_{2,1}Q_1 + V_{2,2}Q_2 + \cdots + V_{2,N}Q_N \\ &\vdots \\ P_N &= V_{N,1}Q_1 + V_{N,2}Q_2 + \cdots + V_{N,N}Q_N \end{aligned} \qquad \text{Eq (4.6.2-3)}$$

or in matrix notation as

$$\mathbf{P} = \mathbf{VQ} \qquad \text{Eq (4.6.2-4)}$$

If $\mathbf{P}$ is normalised by subtracting the mean $\overline{\mathbf{P}}$ and dividing by the standard deviation $\sigma_{\mathbf{P}}$, then the correlation matrix, whose elements are given by Eq (4.6.2-1), can also be written as

$$\begin{aligned} \mathbf{C} &= \mathrm{E}\left[\mathbf{P}\mathbf{P}^T\right] \\ &= \mathrm{E}\left[\mathbf{V}\mathbf{Q}\mathbf{Q}^T\mathbf{V}^T\right] \end{aligned} \qquad \text{Eq (4.6.2-5)}$$

As only the new predictor terms Q are stochastic quantities, Eq (4.6.2-5) can be rewritten

$$\mathbf{C} = \mathbf{V}\,\mathrm{E}\left[\mathbf{Q}\mathbf{Q}^T\right]\mathbf{V}^T \qquad \text{Eq (4.6.2-6)}$$

Then Eq (4.6.2-6) may be written in the form $\mathbf{C} = \mathbf{V}\mathbf{L}\mathbf{V}^T$, where $\mathbf{V}$ is the eigenvector matrix, and $\mathbf{L} = \mathrm{E}\left[\mathbf{Q}\mathbf{Q}^T\right]$ is the matrix of eigenvalues. The eigenvectors and eigenvalues of $\mathbf{C}$ form the basis of Principle Component Analysis.

The eigenvector with the largest eigenvalue accounts for the largest proportion of variance (data dispersion) in the predictor dataset, and is therefore the *Principle Component*. The eigenvector with the second highest eigenvalue accounts for the second largest proportion of data variance (second principle component), etc. The large initial dataset of this broadband noise investigation can therefore be reduced by ignoring the principle components of the smallest eigenvalues. Information is lost, however, if the eigenvalues are small then the amount of variance in the data set unaccounted for is also small. The decision of where to limit the data set is determined arbitrarily. In this investigation, use is made of *Scree Plots* (eigenvalue plots) to identify the number of principle components N to include in the final data set. This will be discussed later in Section 4.9.3.1. An example of a Scree plot can be seen as Figure 4.9.3.1-1.

The principle components are in essence linear combinations of the original predictors that account for the individual uncorrelated behavioural trends of the dataset. The eigenvectors are the 'weights' for each standardized predictor variable used to calculate the principle components, with each eigenvector

indicating the orientation of the respective principle component behaviour in the data set. In matrix form this is given by:

$$\mathbf{Z} = \mathbf{U}\widetilde{\mathbf{P}} \qquad \text{Eq (4.6.2-7)}$$

in a similar form to Eq (4.6.2-4), where **Z** is the matrix of principle components, $\widetilde{\mathbf{P}}$ is the standardised predictor matrix **P**, and **U** is the matrix of eigenvectors.

Each individual principle component represents a statistically uncorrelated 'variable' within the dataset, which may or may not correspond directly to the original physical predictors. A principle component in this study may be simply shaft speed, which can be included directly as a predictor, or could be a factor based on the characteristics of the rotor wake. This is a more complicated example, the modelling of which could be a function of such variables as rotor loss, flow whirl angle, rotor separation characteristics, or rotor efficiency. Unfortunately, Principle Component Analysis does not indentify which predictors are included in each 'component' group, or which combination of predictors could be used to accurately model the desired behavioural trend. This may be remedied for future tests by designing an experiment that isolates the underlying behaviours during testing, by varying the combinations of uncorrelated predictors in such a way that each variation in a principle component can be measured individually. This would allow each principle component to be quantified as a function of several predictors. Inclusion of the principle components would help provide the physically based equations of broadband noise initially desired from this investigation. The use of designed experiments to provide further information on fan rig measured broadband noise is discussed further in Section 4.11.

However, as the current data set was measured by varying only shaft speed and throttle, this detailed information cannot be extracted from the current dataset. Therefore, in this investigation it is assumed that the variance in the predictor dataset, due to the underlying behaviour of the information contained within **C**, captured by each of the *N* uncorrelated principle components in **U**, may be encapsulated as much as possible by defining *N* uncorrelated groups of collinear (i.e. correlated) predictors. The aim is to capture as much as possible the effect of the underlying behaviour on the predictor dataset. This procedure has the advantage of providing insight into the physical reasons behind the collinearity of the different groupings (clusters) of predictors. Such knowledge would contribute to any future designed experiment by identifying individual predictors that could be modified to provide the desired behavioural change. As each of these uncorrelated groupings is formed of collinear predictors, every grouping can be reduced to a single representative predictor taken from the cluster. In order to identify collinear predictors and arrange these into *N* corresponding groupings, *Cluster Analysis* is used. This technique is described below.

4.6.3. Cluster Analysis

Cluster analysis classifies the individual predictors into a number of different statistically correlated sets called 'clusters'. The number of clusters N to be formed is defined by using Principle Component Analysis, described above.

Predictors to be grouped into a single cluster are compared in terms of their 'distance'. A 'correlation distance matrix' **D** is created, whose components $d_{m,n}$ are calculated from

$$d_{m,n} = 1 - c_{m,n} \qquad \text{Eq (4.6.3-1)}$$

where $c_{m,n}$ is the correlation coefficient between any two predictors P_m and P_n, calculated using Eq (4.6.2-1) above. 'Distances' $d_{m,n}$ are therefore between 0 and 1 for positive correlations, and between 1 and 2 for negative correlations. This means that negatively correlated data are considered further apart than positively correlated data. The correlation distance matrix **D** is used to store these correlation coefficients for calculation of the 'linkage method' and 'similarity' between predictors and clusters, as explained below.

The cluster amalgamation procedure begins with all predictors assumed to be uncorrelated. The method of clustering is called 'linkage'. For this investigation, *weighted average linkage*, also called 'McQuitty's method', is used. This method calculates the average of the distances of two clusters which are about to be joined to form another cluster. Consider for example four clusters, each of which initially contains a single predictor, labelled 1, 2, 3, and 4. The objective is to amalgamate these clusters using the above weighted average linkage method.

Assuming clusters 1 and 2 are highly correlated, their 'distance' defined using Eq (4.6.3-1) is very small, and they form a new cluster which can be labelled 1^*. The next amalgamation step can form a new cluster from three possibilities; grouping clusters 3 and 4, or joining cluster 3 to cluster 1^*, or cluster 4 to cluster 1^*.

The distance between clusters 3 and 4 can be calculated using Eq (4.6.3-1) as before. However, the distance between cluster 3 and cluster 1^* is calculated as the average of the distances between cluster 1 to cluster 3, and cluster 2 to cluster 3. Likewise for considering cluster 4 and cluster 1^*. This procedure can be written as Eq (4.6.3-2) below:

$$d_k = \frac{d_m + d_n}{2} \qquad \text{Eq (4.6.3-2)}$$

where d_m and d_n denotes the distance between any two clusters, and d_k denotes the resulting amalgamated distance. Therefore as the clustering progresses and more groupings are formed, the

amalgamation distance depends on a combination of predictors rather than individual predictors within a cluster.

The number of clusters to be formed can be specified in two ways. The first is by indicating the final number of clusters directly. The second is by specifying the 'similarity' limit below which two clusters are not amalgamated. The similarity S_{mn} between two clusters m and n is calculated using Eq (4.6.3-3) below

$$S_{mn} = 100\frac{(1-d_{mn})}{d_{\max}} \qquad \text{Eq (4.6.3-3)}$$

where d_{max} is the maximum distance in the distance matrix **D**. This 'similarity' limit is applied during the formation of the clusters.

In this investigation the linking of predictors continues until the specified final number of N clusters has been formed, with N having been determined using Principle Component Analysis. We assume that each of the final clusters is a group of statistically correlated (collinear) variables, and that the final clusters are sufficiently statistically uncorrelated with each other. Each cluster therefore attempts to incorporate as much as possible the effect of a principle component of the previous analysis.

Section 4.6.1 above has introduced the procedure used in this investigation to calculate $\mathbf{a_0}$, the vector of N predictor coefficients. However, before these techniques can be applied, the vector **w** containing the sound power measurements and the matrix **P** of predictors must be formed. The following section describes how these matrices are formed from the available predictor and measurement datasets.

4.7. Formation of noise and predictor data sets

As mentioned above the flow and performance variables associated with a particular noise measurement are calculated using a simple through-flow code. Some flow parameters take single values, such as efficiency or pressure ratio, while others are presented as a radial profile whose values vary as a function of radius, such as flow Mach number or flow angle. In these cases the parameter under investigation is represented by its value at the representative spanwise position of *10%*, *50%*, and *95%* of the blade span.

Table 3 below lists the flow and performance variables whose influence on fan broadband noise is to be investigated:

Predictor Variable Name	Predictor Code	Single or Radial Values
Fan shaft speed	Shaft Speed RPM	Single
Total rotor mass flow	Rotor mass flow	Single
Rotor total pressure ratio	Rotor PR	Single
OGV total pressure ratio	OGV PR	Single
ESS total pressure ratio	ESS PR	Single
Total rotor efficiency	Rotor Eff	Single
Total OGV efficiency	OGV Eff	Single
Total ESS efficiency	ESS Eff	Single
Rotor flow Mach number	Rotor M	10% 50% 95%
OGV flow Mach number	OGV M	10% 50% 95%
ESS flow Mach number	ESS M	10% 50% 95%
Rotor outlet flow whirl angle	Rotor WHIRL	10% 50% 95%
OGV inlet flow whirl angle	OGV WHIRL	10% 50% 95%
ESS inlet flow whirl angle	ESS WHIRL	10% 50% 95%
Rotor diffusion factor	Rotor Diff Fact	10% 50% 95%
OGV diffusion factor	OGV Diff Fact	10% 50% 95%
ESS diffusion factor	ESS Diff Fact	10% 50% 95%
Rotor pressure loss coefficient	Rotor PLC	10% 50% 95%
ESS pressure loss coefficient	ESS PLC	10% 50% 95%

Table 3 – Flow and performance predictors included in this investigation

Most of these predictors are non-dimensional, with the exception of rotor mass flow (kgs/sec), and the whirl angle predictors (degrees). In addition to the predictors listed in the table above, a number of covariates are available for inclusion in the correlation equations. As mentioned previously, covariates are features of the rig architecture that should be taken into account in the analysis, such as liner type, blade type, and on which fan working line the experiment is made. The effect of these parameters on noise and flow is often complicated. Differences between individual covariates of a specific type, such as rig liner types, or fan blades, are often complex and subtle. For example, small differences in blade geometry could affect the position of flow transition over the fan blades. Some of these subtle differences cannot be parameterised from the data sets available. Differences between covariates can therefore only be included in this study by recognising their existence. Therefore many of the covariates listed Table 2, Section 4.7 of Appendix X are indexed to indicate which 'version' of the covariate is present for each experimental data set. For example, if the case liner was present during a test, then the case liner parameter 'p' is assigned the index '1', if the case liner were removed for a test then the case liner index is assigned '2'. A complete list of the covariates included in this investigation, along with a key associating an index with each covariate, can be seen in Table 2 of Appendix X

Rear-arc measurements of the pressure spectrum are taken from the bypass duct. Rear-arc sound pressure level measurements (SPL dB) are converted into sound power levels using the relationship derived by Joseph et-al [27]. Measurements of acoustic power in the forward arc are made using a semi-circular array located 18.3m from the inlet.

When performing the final least squares analysis to form the regression equation, it is desirable to keep some data in reserve to use as a test case for the final derived regression equations. This data must not be used when deriving the correlation equation; including the additional variance of the test cases will mean their objectivity is compromised. Two test cases were reserved. The test cases chosen to be reserved during this study are the results of the Engine 3 fan on working line 5, and the Engine 5 fan with a conventional liner on working line 3.

One of the main difficulties with deriving linear regression equations from the noise data is that flow and performance variables may be strongly collinear, i.e. they may be strongly statistically correlated. For example, as fan speed increases many of the flow, performance, and noise parameters increase proportionally. The techniques described above, namely Principle Component Analysis, Cluster Analysis, and Least Squares regression, are used to reduce the number of collinear variables and hence derive noise prediction correlations in terms of the important independent parameters. Two sets of correlation equations of the form of Eq (4.5-1) are derived. The first consists only of flow and performance parameters; the second also includes the covariate parameters listed in Table 2 of Appendix X.

The procedure used to produce the final regression equations can be summarised as follows:

1. Rig measurements are pre-processed. The measured sound pressure level is converted into sound power levels, and the broadband noise calculated in defined frequency bands, for each measured shaft speed

2. Experimentally measured broadband noise levels are matched to calculated flow and performance parameters to form complete sets of data for the equivalent shat speed performance points

3. Principle Component Analysis (Section 4.6.2) is used to identify the minimum number of predictors required to explain the maximum amount of measured noise variation. The results of this analysis suggest that the number of predictors N that the data set can be reduced to, thereby limiting the redundancy of the collinear predictors

4. Cluster Analysis (Section 4.6.3) is used to rearrange the predictors into a number of 'families', based on the finding of Principle Component Analysis. This allows the identification of the reduced predictors used in the final regression equation

5. Finally regression equations are obtained to provide a fit between the predictors and response variables using Least squares analysis (Section 4.6.1)

The following section is a description of the rig noise measurement preparation carried out during this investigation, commencing with a description of how the rig measurements were pre-processed into the vector of noise data, **w**.

4.8. Rig measurement pre-processing

This section describes the pre-processing procedure applied to the rig measured noise data, in preparation for the procedure that will determine the parameters which are statistically important for fan broadband noise. We consider first the removal of the blade passing frequency tones.

4.8.1. Removal of BPF tones

A typical sound pressure level spectrum measured in an aero-engine duct is characterised by a broadband spectrum superimposed on a number of tones. An example of this can be seen in Figure 4.8.1-1 of Appendix X.

The largest tones occur at the blade passing frequency, and its harmonics. In this investigation the BPF tones are removed by simply deleting them and replacing their SPL values by the broadband levels in the frequency bins immediately adjacent.

Numerous tones remain at the higher shaft speeds. These are *Buzz-Saw Tones*, so called because they sound like a chain or buzz saw. This noise signature is the buzz signature which has a tone at every integer EO.

Due to the difficulty in identifying the broadband noise floor amongst the buzz-saw tones the spectra used for the correlation analysis were restricted to shaft speeds below that at which the buzz-saw noise appears, this cut-off speed is given in Section 4.8.1 of Appendix X.

The objective of this study is not to predict the spectral shape of fan broadband noise but instead to estimate the broadband sound power level in specified frequency bands, according to Eq (4.5-1). As mentioned previously in Section 4.2 these bands are termed BB's in this thesis, such that *BBn* is the frequency bandwidth defined in Eq (4.2-3).

There are, however, several unavoidable problems with this choice of frequency bandwidth for comparing the results from different fans. The first is that the EO ranges for each rig and working line are not equal since the blade passing frequencies are different for each fan. A common range of EOs for all cases cannot therefore be defined. A BB bandwidth on one fan may overlap the BPF locations of another fan. Therefore, all of the EO ranges defined, while generally overlapping, are individual to the specific experimental case.

4.8.2. Converting from Sound Pressure Level (SPL) to Sound Power Level (PWL)

As the regression analysis is based on sound power it is necessary to convert the sound pressure level measurements made in the rig to sound power. The theoretical basis and assumptions used for making this conversion are outlined in reference [27]. Only the main assumptions and equations used are presented here.

The approach predicts the relationship between sound power and pressure based on the assumption that the duct is infinite and hard-walled, and then the overall sound power is shared equally amongst the cut-on modes, propagating in a uniform mean flow.

The total transmitted sound power in a duct can be estimated from the mean square pressure at the duct wall using Eq (4.8.2-1) below

$$\overline{W} = \frac{\beta_s}{4}\frac{S\left(p_{RMS}^2\right)}{\rho c} \qquad \text{Eq (4.8.2-1)}$$

S is the duct cross section, ρ is the mean density, and c is the speed of sound and P_{RMS} denotes the root-mean-squared sound pressure measured at the duct wall. β_s is a non-dimensional constant, which for high ka (non-dimensionalised wave number) is given by:

$$\beta_S = \frac{1}{2}\left(1 - M_x + \frac{1}{3}M_x^{\,2}\right)^{-1} \qquad (ka \to \infty) \qquad \text{Eq (4.8.2-2)}$$

where M_x is the flow axial Mach number. The total sound power in decibels is then calculated by

$$PWL = 10\log_{10}\left(\frac{\overline{W}}{W_{ref}}\right) \qquad \text{Eq (4.8.2-3)}$$

with $W_{ref} = 10^{-12}$ watts.

4.9. Statistical Analysis of the Fan Broadband Noise Data

This section describes the application of the various statistical techniques that are used in this analysis to the spectral data. The analysis was performed using the commercial software package 'Minitab'. An example case is described, with selected illustrative results being shown. The test case chosen is the BB1 broadband noise region in both the forward and rearward arcs, with and without covariates included.

To commence, some definitions are presented in order to understand the presentation of results.

4.9.1. P-value and α-level

The most important statistic to consider in this investigation is the probability, in this thesis termed the '*p-value'*, of whether to reject the null-hypothesis in a hypothesis test. An hypothesis test is a procedure that evaluates which of two mutually exclusive statements about a population is likely to be true. The two statements are called the *null* hypothesis and the *alternate* hypothesis.

In terms of this investigation, an example of the null hypothesis is 'BB1 does not correlate with fan efficiency'. If the *p-value* were to fall below the *α-level*, then this hypothesis would be rejected in favour of the alternate hypothesis that 'BB1 does correlate with fan efficiency'.

The *α-level* is a user defined cut-off point, which is the maximum acceptable risk of rejecting a true null hypothesis (called a type-1 error). This is also called the level of significance. During this investigation the *α-level* is set equal to 0.05, so that the chance of finding an effect that does not exist is 5%. With a small α-level there is less possibility of rejecting the null-hypothesis by mistake, though this also means a decreased chance of detecting an effect if one truly exists.

4.9.1.1. A note on Statistical Significance

A sample statistic is statistically significant if a hypothesis test proves it to be too unlikely to have occurred by chance. In other words the statistic is probably true, and is said to have 'statistical significance'. This *does not* mean that the effect is important, according to everyday use of the word significant. The p-value assesses statistical significance.

4.9.2. Definition of R^2

The R^2 (also *R-sq*) values shown in the results below define the percentage of the response variables that are explained by their relationship to one or more predictors. In this investigation R^2 values are used to estimate how well the final regression equations fit the measured data and predict the test cases not included in the analysis. If the model were to explain 100% of the response variance then the R^2 value would be equal to 1.

The following section describes the application of Principle Component Analysis, Cluster Analysis, and Least squares Analysis to the pre-processed data-set. Selected results for BB1 in the forward and rearward arc are shown.

4.9.3. Application of statistical analysis tools to the fan noise and predictor database

As mentioned previously the fan noise predictors used in this analysis exhibit high levels of multi-collinearity. This means that some predictors P are correlated with other predictors, making meaningful analysis difficult. This section describes the application of the procedures used to remove the influence of multi-collinearity when deriving the broadband noise correlations.

There are two solutions to solving the problem of multi-collinearity. The first is to simply remove highly correlated parameters from the model. The highly correlated predictors provide redundant information; therefore their removal does not greatly affect the residuals of the final predictive model of Eq (4.5-1). Another approach is to use Principle Component Analysis (PCA). As described above in Section 4.6.2 this approach reduces the number of predictors to a smaller set of statistically uncorrelated components. Principle Component Analysis allows the estimation of the number of uncorrelated parameters N by accounting for the maximum proportion of variance (dispersion within the dataset) with the fewest number of principle components. Cluster Analysis is then used to separate the complete predictor set into the suggested number N of uncorrelated parameter families, to identify which predictors can be used in a broadband noise prediction equation. Finally, Least Squares analysis is performed to generate best-fit prediction equations using the chosen predictors. The output of the Least Squares analysis is the regression equation Eq (4.5-1).

The results of each of these three techniques are discussed further below, with typical results presented for the prediction of BB1 in the forward and rearward arc. This analysis can also be performed on the other broadband noise regions, in both forward and rearward arcs. However, similar findings are made and therefore these results are not shown in this thesis.

4.9.3.1. Principle Component Analysis

As described in Section 4.6.2, Principle Component Analysis is used to reduce a large number of collinear predictors into a smaller number of uncorrelated predictors. A graphical representation of the Principle Component Analysis results for deciding the significant number of factors in this analysis is the Scree Plot, an example of which is shown below in Figure 4.9.3.1-1, for BB1 noise measured in the rear arc. A Scree Plot is a plot of the eigenvalues of the Principle Components (Eq (4.6.2-6)) in descending order versus the component number.

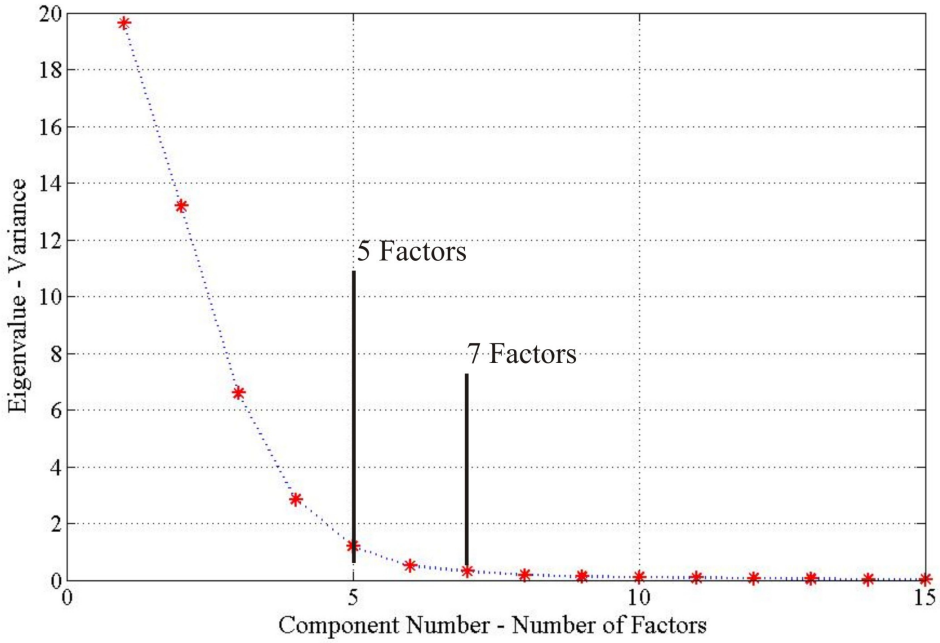

Figure 4.9.3.1-1 - Scree plot for BB1 in the rear arc

The eigenvalues are also plotted in Table 4 below, which tabulates the eigenvalue, proportion of variance, and cumulative variance accounted for by each factor group. 'Proportion of variance' explained by the k^{th} principle component is defined as

$$\frac{L_{k,k}}{L_{1,1}+L_{2,2}+\cdots+L_{M,M}} \qquad \text{Eq (4.9.3.1-1)}$$

with $L_{k,k}$ being the k^{th} eigenvalue, and M the total number of principle components. The 'cumulative proportion of variance' for principle component k is calculated by:

$$\frac{L_{1,1}+L_{2,2}+\cdots+L_{k,k}}{L_{1,1}+L_{2,2}+\cdots+L_{M,M}} \qquad \text{Eq (4.9.3.1-2)}$$

Eigenvalue	20.696	9.858	6.792	4.158	1.216	0.561	0.240	0.197	0.084
Proportion	0.470	0.224	0.154	0.094	0.028	0.013	0.005	0.004	0.002
Cumulative	0.470	0.694	0.849	0.943	0.971	0.984	0.989	0.994	0.996
Eigenvalue	0.044	0.043	0.031	0.023	0.015	0.013	0.007	0.006	0.004
Proportion	0.001	0.001	0.001	0.001	0.000	0.000	0.000	0.000	0.000
Cumulative	0.997	0.998	0.998	0.999	0.999	0.999	1.000	1.000	1.000

Table 4 – Principle Component Analysis for BB1 in the rear arc

The sum of the eigenvalues equals the number of predictors included in the analysis, with the first eigenvalue accounting for the variance of approximately 20.696 'predictors'. A number of different approaches to deciding on how many principle components are required. The first approach is to apply the 'Kaiser Criterion', which states that only components with an eigenvalue above 1 should be retained. This is equivalent to stating that unless a factor extracts at least as much as the equivalent of one original predictor, it should not be included. This would suggest 5 components are necessary. The

second approach is simply to retain the number of components up to the start of the horizontal portion of the Scree plot. From Figure 4.9.3.1-1 above this is approximately 7.

The number of factors *N* to be investigated using Cluster Analysis for broadband noise region 1 in the rear arc, without covariates, is therefore 5 and 7. An equivalent analysis carried out on broadband noise region 1 in the forward arc, including covariates, suggests the use of 9 predictors.

4.9.3.2. Cluster Analysis

As described in Section 4.6.3, Cluster Analysis classifies variables into different sets of statistically correlated predictors. The number of clusters to be formed has been determined by Principle Component Analysis as 5 for BB1 in the rear arc without covariates, and 9 for BB1 in the forward arc including covariates. It is assumed that the variance in the predictor dataset due to the underlying behaviour captured by each of the *N* uncorrelated principle components may be encapsulated by defining *N* uncorrelated groups of collinear predictors. Principle Component Analysis does not indicate which predictors are used to form the required components. It is therefore necessary to apply Cluster Analysis to identify the groupings of collinear predictors. One representative predictor can then be chosen from each independent cluster.

Section 4.9.3.2 of Appendix X includes the cluster analysis of the data obtained in the rear arc for BB1 with 5 predictors and no covariates, and the cluster analysis of the same noise band in the forward arc for 9 predictors with covariates.

For BB1 in the rear arc without covariates, the 5 suggested predictors are:

- Cluster 1 - Fan tip relative Mach number - Rotor M 95
- Cluster 2 - Rotor efficiency - Rotor Eff
- Cluster 3 - Fan tip exit flow whirl angle - Rotor Whirl 95
- Cluster 4 - OGV mid-span inlet whirl angle – OGV whirl 50
- Cluster 5 - Rotor tip pressure loss coefficient - Rotor PLC 95

For BB1 in the forward arc with covariates, the 9 predictors suggested by Cluster Analysis are

- Cluster 1 - Inlet Temperature – Temp
- Cluster 2 - Rotor Efficiency – Rotor Eff
- Cluster 3 - Number of blades – No. of Blades
- Cluster 4 - OGV mid-span inlet whirl angle – OGV Whirl 50
- Cluster 5 - Rotor tip inlet Mach number – Rotor M 95
- Cluster 6 - Rotor flow exit whirl angle 95% span – Rotor Whirl 95
- Cluster 7 - Rotor tip pressure loss coefficient - Rotor PLC 95
- Cluster 8 - Engine Section Stator hub whirl angle – ESS Whirl 10
- Cluster 9 - Rotor mid-span diffusion factor – Rotor Diff Fact 50

The predictors listed above are then used to form correlation equations to predict fan broadband noise, using Least Squares Analysis. This is described below.

4.9.3.3. Least Squares Analysis

Least Squares regression is now used to form regression equations of Eq (4.5-1) from the predictors decided upon in Section 4.9.3.2. The final results of regression equations can be used to create residuals between the measured and fitted noise data ($r = PWL_{\exp} - PWL_{pred}$), as described in Section 4.6.1. The assessment of these residuals is important in order to ensure that the rig noise measurements are of sufficient quality, and the assumptions are met that allow the application of statistical analyses. Therefore, before considering the final regression equation, the following section describes the analysis of residuals in this investigation.

4.9.3.3.1. Residuals and Analysis

There are a number of presentations of the residual data that are used within this investigation for quantifying the goodness of fit. Examples of the use of regression analysis, applied to the data set, are shown in Figure 4.9.3.3.1-1to Figure 4.9.3.3.1-4. These are:

1. Normal probability plot
2. Histogram
3. Fitted value plot
4. Observation vs. order plot

Each of these figures will now be discussed in turn. The regression analysis that generates these figures is presented later in this chapter. Similar figures can be generated by Principle Component Analysis and Cluster Analysis.

1. Normal probability plot

Figure 4.9.3.3.1-2 is the normal probability plot, whereby the cumulative distribution of the residuals is plotted against the standardised residuals.

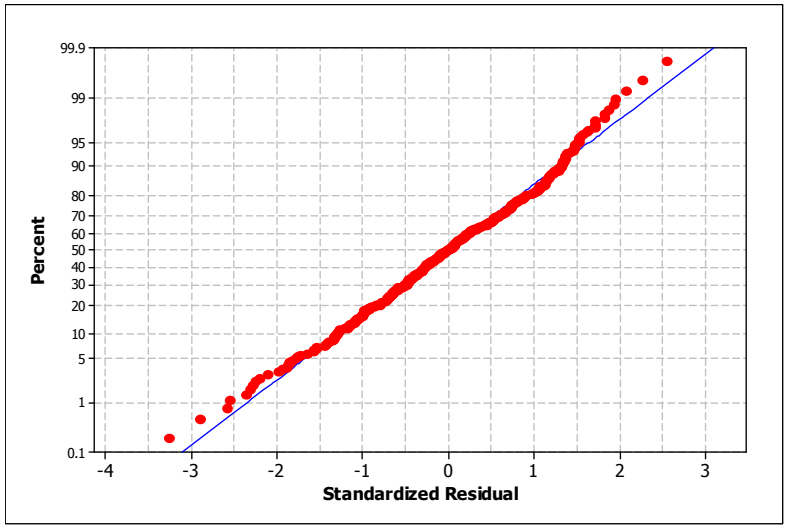

Figure 4.9.3.3.1-1 – Normal probability plot of residuals

The *standardized residuals* are calculated by dividing the residual by its standard deviation. Standardized residuals are used because all of the data used by the analysis can be plotted on the same figure despite their disparate units. The cumulative distribution is the percentage of values in the sample that are less than or equal to it, denoted *percent*. The straight blue line in this figure is the theoretical slope the residuals would follow if they were perfectly normally distributed. The red points mark the actual residual data.

Although the regression approach assumes normally distributed data, in practice small departures from normality are acceptable for data with a large number of observations. The usefulness of this representation is that it reveals the presence of *outliers*. These are single extreme values that can greatly influence the regression coefficients *a*. If outliers are present then this may indicate measurement error for example. Also, Figure 4.9.3.3.1-2 shows that all of the data points are close to the theoretical value. This suggests that the data is sufficiently 'normal' to be used with regression analysis. Departure from normality would suggest difficulties with the suitability of the noise database for use in this type of investigation. The presence of non-normal behaviour may only be with one working line or fan noise data set. Alternatively, it could indicate a problem with the measurement procedure or technique used when measuring the database. Fortunately the data appears to be satisfactory in this case.

2. Histogram

Figure 4.9.3.3.1-3 is a plot of the standardized residuals of the predictor data set versus the frequency of occurrence, in the form of a histogram.

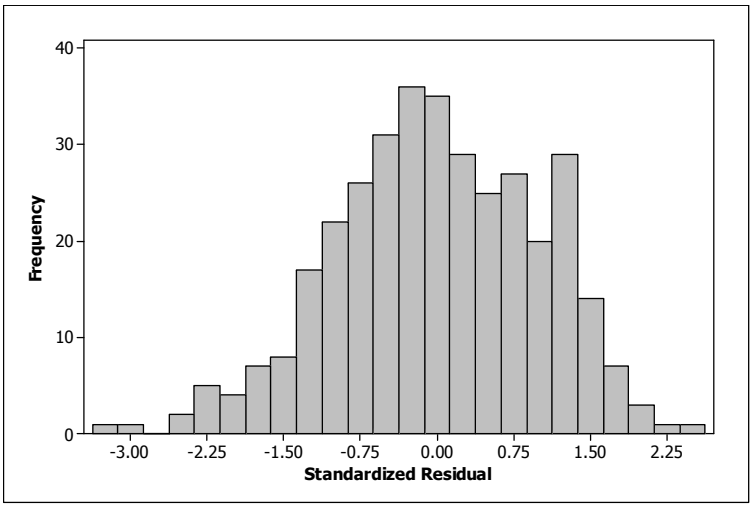

Figure 4.9.3.3.1-2 – Histogram of predictors

Although a histogram of the residuals can indicate normality, use of a Normal Probability Plot is preferable for such an analysis. The histogram is used to assess general characteristics of the data. Outliers can be identified by spurious bars located away from the main cluster. Long tails suggest skewness in the data set. For this data set, Figure 4.9.3.3.1-3 displays little skewness. Note that lack of skewness alone does not indicate normality, which is why the Normal Probability plot should also be used to assess whether or not the data is normally distributed.

3. Fitted value plot

Figure 4.9.3.3.1-3 plots the predicted values versus the standardized residuals.

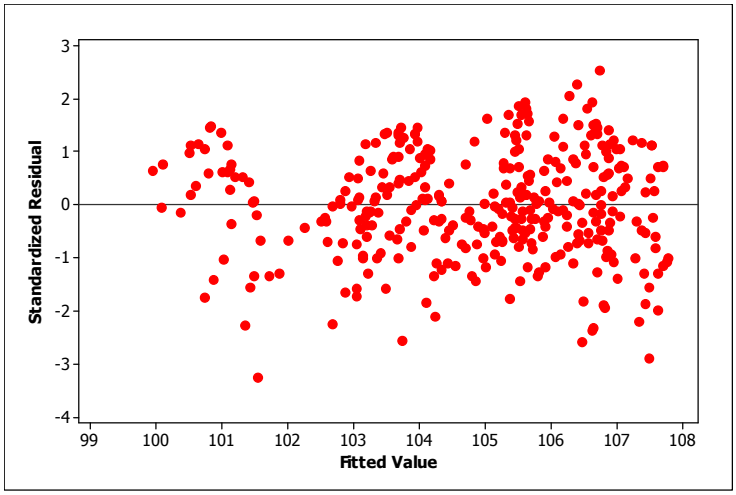

Figure 4.9.3.3.1-3 – Fitted value plot of predicted mean response

In regression analysis *Fitted Values* are calculated by substituting selected predictor values into the regression equation, providing an estimate of the mean response for the given predictor values. These are plotted versus the standardised residuals. Ideally the points should be scattered about zero. Figure 4.9.3.3.1-3 displays satisfactory scatter, although a broader spread is visible for the negative standardized residuals. This indicates that the regression equation used to generate these plots fits the data relatively well, although some predictors present in the data set are lower than would be expected by the regression equation.

4. Observation versus order

Figure 4.9.3.3.1-5 plots the observation order of the measurements versus the standardized residuals.

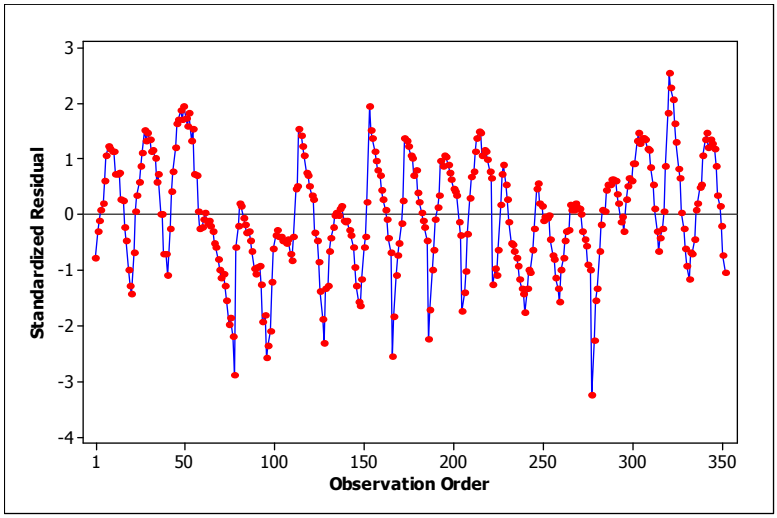

Figure 4.9.3.3.1-4 – Observations versus order

Figure 4.9.3.3.1-4 can be used to assess whether the order in which the data is taken influences the measured results. The data should form a random pattern. In Figure 4.9.3.3.1-4 a repetitive pattern is apparent, due to the grouping of measurement into their respective rig and working line sets. This form of grouping is often difficult to correct after the data has been measured. If possible, therefore, the runs of the experiment should be randomised. This should be noted for future experimental campaigns, although randomising all predictors may be difficult to achieve on a fan rig where the number of controllable variables during test are limited to fan speed and throttle area.

The full derivation and analysis of the results of the Least Squares Analysis can be seen in Section 4.9.3.4. of Appendix X. A summary of the final results can be seen below.

4.9.3.4. Least Squares Analysis Results

The following section presents the regression equation coefficients and results calculated for the example cases of BB1 in the rear arc without covariates, shown in Section 4.9.3.4.1, and BB1 in the forward arc with covariates, presented in Section 4.9.3.4.2.

4.9.3.4.1. BB1 in the rear arc without covariates

Typical results of a least squares analysis applied to broadband noise region BB1 in the rear arc are now presented. This section presents results for a regression equation formed from 5 flow and performance predictors, without the inclusion of covariants. The use of 5 predictors for this regression equation has been suggested by the Principle Components Analysis performed previously.

The *P-value* for the overall model is calculated to be 0.000. This is less than the defined *alpha* of 0.05 which suggests that the model is statistically significant. These parameters were defined previously in Section 4.9.1. Table 5 below lists the standard errors and p-values of each predictor. The individual coefficients for each predictor can be seen in Section 4.9.3.3.2 of Appendix X

Predictor P_i	Coefficient a_i	Coefficient Standard Error	P-value
Constant	**u**	15.52	0
Rotor Eff	**v**	0.1108	0
Rotor M 95	**w**	0.4973	0
Rotor Whirl 95	**x**	0.08294	0
OGV Whirl 50	**y**	0.04861	0
Rotor PLC 95	**z**	2.451	0.496

Table 5 – Model Selection and Validation for Broadband noise region 1, rear arc

The final correlation equation, in the form of Eq (4.5-1), can therefore be written as

$$\begin{aligned} BB1 = {} & \mathbf{u} - \mathbf{v} \times (Rotor\ Eff) + \mathbf{w} \times (Rotor\ M\ 95) \\ & - \mathbf{x} \times (Rotor\ Whirl\ 95) - \mathbf{y} \times (OGV\ Whirl\ 50) \\ & + \mathbf{z} \times (Rotor\ PLC\ 95) \end{aligned} \qquad \text{Eq (4.9.3.4.1-1)}$$

The predictors that form this regression equation have been chosen from the cluster analysis, due to their importance to broadband noise in the rear arc. Note that the numerical values of these predictors are visible in Table 5, of Appendix X. The sign of the associated coefficient is shown above in Eq (4.9.3.4.1-1) provides insight to the effect on broadband noise of modifying the predictor.

The regression equation derived above can be used to predict the broadband noise in the rear arc for the two test cases left out from the regression analysis, the Engine 3 fan on working line 5, and the Engine 5 fan with liner on working line 5. A preliminary assessment of the accuracy of the model is presented in Figure 4.9.3.4.1-1 below, which presents a comparison of the shaft speed versus measured and predicted sound power values.

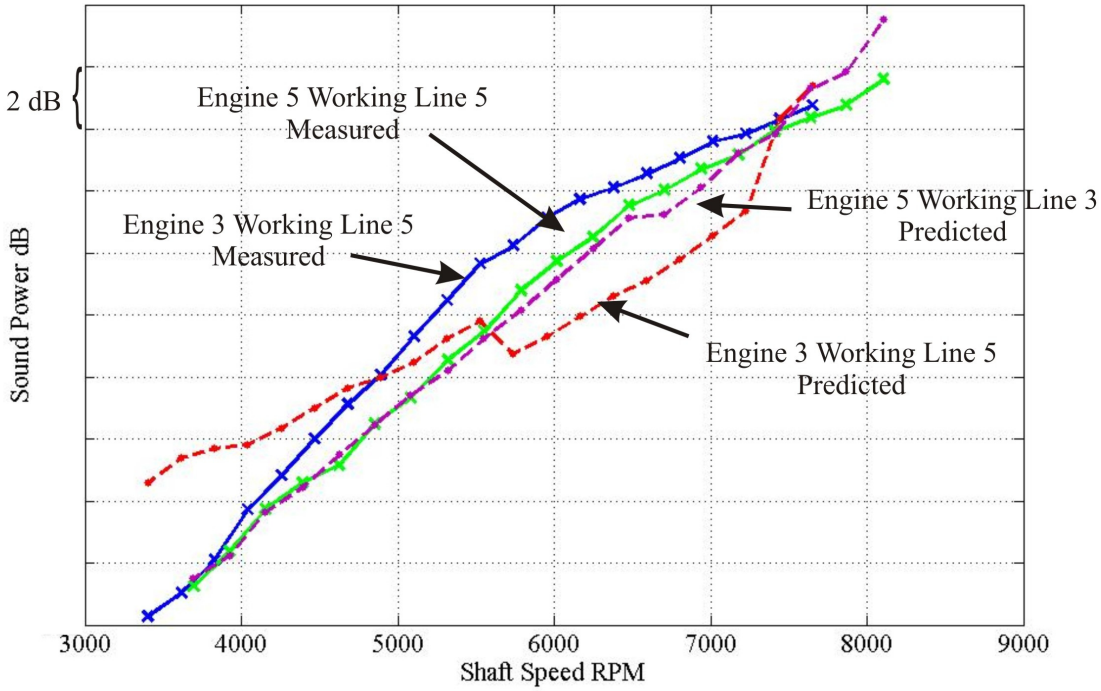

Figure 4.9.3.4.1-1 – Measured and predicted BB1 sound power, rearward arc, 5 predictors without covariates

The regression equation predicts the noise of the Engine 5 fan more accurately than the Engine 3. The predicted spectra are within 2dB of the measured spectra, except at very low shaft speeds for the engine 3 working line 5 case. This difference occurs despite the large number of measurement points used to form the regression equation, and shows the difficulty of deriving a predictive correlation that remains accurate when asked to predict the fan noise for a different performance point. The high level flow and performance predictors chosen do not capture all the changes in noise sources measured on the rig.

The largest discrepancy for the Engine 3 noise prediction is between approximately 5500 and 7500 Hz. This is due to sudden increases in several Engine 3 predictor variables, not shown here, including fan tip pressure loss coefficient, and fan tip flow exit whirl angle. These predictors have negative coefficients in Table 5. An increase in predictor value therefore causes a corresponding decrease in predicted sound power. The discrepancy between Engine 3 measured and predicted sound power at

low shaft speeds appears to be due to a reduction in rotor efficiency at these shaft speeds. (Note that this figure, with further discussion, is shown in Appendix X, Section 4.9.3.4.1).

The following section presents the results of the Least Squares analysis of BB1 in the forward arc with covariates.

4.9.3.4.2. BB1 in the forward arc with covariates

The Least Squares Analysis of BB1 in the forward arc including covariates, seen in Section 4.9.3.4.2, of Appendix X originally suggested the use of 7 predictors. However, using 7 predictors was not found to be accurate when using the resulting correlation equation to predict the broadband noise of the reserved test case. An additional two predictors were required to provide satisfactory prediction.

The inclusion of the additional predictors produces a regression equation with a p-value of 0.000. The final regression equation is:

$$\begin{aligned} BB1 = {} & \mathbf{q} - \mathbf{r} \times (No.Blades) - \mathbf{s} \times (Temp) \\ & - \mathbf{t} \times (Rotor\ Eff) + \mathbf{u} \times (Rotor\ M\ 95) \\ & + \mathbf{v} \times (Rotor\ Whirl\ 95) + \mathbf{w} \times (OGV\ Whirl\ 50) \\ & - \mathbf{x} \times (Rotor\ PLC\ 95) - \mathbf{y} \times (ESS\ Whirl\ 10) \\ & - \mathbf{z} \times (Rotor\ Diff\ Fact\ 50) \end{aligned} \qquad \text{Eq (4.9.3.4.2-1)}$$

The numerical values of the coefficients for each predictor can be seen in Section 4.9.3.4.2 of Appendix X. The p-values of each individual predictor is also 0.000, as shown below in Table 6. This suggests that the above combination of predictors allows a broadband noise prediction with a larger degree of correction due to the larger number of degrees of freedom, allowing each predictor to be 'statistically significant'.

Predictor P_i	Coefficient a_i	Coefficient Standard Error	P-value
Constant	**q**	29.48	0
No. Blades	**r**	0.2006	0
Temp	**s**	0.02351	0
Rotor Eff	**t**	0.1761	0
Rotor M 95	**u**	1.463	0
Rotor Whirl 95	**v**	0.2036	0
OGV Whirl 50	**w**	0.08316	0
Rotor PLC 95	**x**	3.283	0
ESS Whirl 10	**y**	0.107	0
Rotor Diff Fact 50	**z**	5.274	0

Table 6 – New Model Selection and Validation for Broadband noise region 1, forward arc

The new model described above accounts for approximately 78.5% of the measured noise variation (R-sq value). This accuracy is confirmed when using the regression equation of Eq (4.9.3.4.2-1) to predict the forward arc broadband noise of the two reserve test cases, which can be seen below in Figure 4.9.3.4.2.

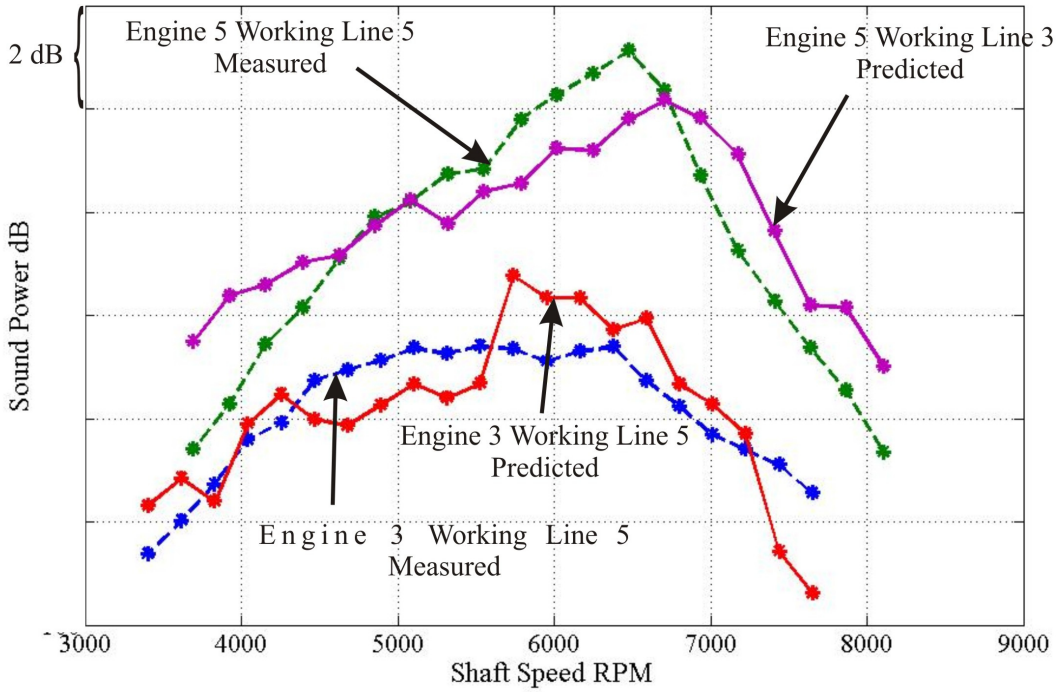

Figure 4.9.3.4.2-1 – Measured and predicted BB1 sound power in the forward arc, 9 predictors with covariates

Note that while BB1 in the rear arc (Figure 4.9.3.4.1-1) increases monotonically with shaft speed, BB1 in the forward arc peaks between 6000 and 65000 RPM. This is most likely due to the increase in rotor blockage with higher shaft speeds. This increase in blockage at high speed for these low pressure ratio working lines, and may indicate the presence of shocks on the rotor blade preventing the propagation of broadband noise in the forward arc (c.f. Figure 4.4.1-3, of Appendix X).

This accuracy was not found when using 7 predictors, as shown in Appendix X, Section 4.9.3.4.2. There are several possible explanations for the improvement in the predictive capability of the model by adding the two additional predictors. The most probable reason is simply the increase in the number of degrees of freedom provided by the increase in the number of predictors. Increasing the number of predictors to 9 increases the variance of the predictor data set that is included in the regression model.

However, the increase in the number of degrees of freedom included in the regression equation, may mask the additional effects included in the new regression equation. The additional predictors chosen for inclusion in the regression equation, via the procedure displayed in Section 4.9.3.4.2 of Appendix X, allow the inclusion of the interaction between rotor hub flow and the ESS cascade. These predictors were not chosen for inclusion in the first version of the forward arc BB1 noise regression equation. The need to include the larger number of predictors than Principle Component Analysis suggested, implies that the assumption made in the use of cluster analysis may not be correct.

This assumption stated that the variance in the predictor dataset, due to the underlying behaviour captured by each of the *N* uncorrelated principle components, may be encapsulated by defining *N* uncorrelated groups of collinear predictors. There are three different ways of interpreting the possible consequences from the results of the regression analysis:

1. The assumption is wrong and it is not possible to encapsulate the variance of the *N* uncorrelated principle components by creating *N* uncorrelated clusters. This may be due to the fact that one or more of the principle components may be due to the interaction between predictors that may or may not be placed in a specific cluster.

2. The assumption is correct. However, the principle components defined suggest noise prediction mechanisms (which could be for example rotor wake interaction with downstream vanes) that may be applied to both OGV and ESS cascades.

3. The assumption is correct. However, from the results of the cluster analysis one cannot state whether the correlated predictors within each cluster are collinear because they vary in a correlated sense due to different physical effects, or are actually related due to a physical interaction between possible groups of different predictors.

Ultimately the three reasons listed above are different ways of looking at the same problem with using the current predictor dataset for this type of analysis. One must identify and isolate the effects within the predictor dataset labelled ‘principle components’. These must be varied during testing in such a way that the relationship between the different predictors and these principle components can be modelled. These future tests must take any necessary covariates into account. However, if understanding is desired of the broadband noise generating mechanisms of the fan stage (rotor, OGV, ESS) specifically, restrictions should be placed on the use of additional inlet forms, liners, etc. until the noise generating mechanisms themselves are quantified.

The following section will discuss the findings of this correlation study, including accuracy of the regression equations derived, the process of derivation of the regression equations, and the difficulties encountered when including covariates.

4.10. Discussion of the correlation study

The regression equations derived in this study include several additional predictors over the current broadband noise model. They offer therefore a greater degree of flexibility as they allow a single correlation equation to be applied to the fan rigs whose data was used during the derivation of the regression equations. The cluster analysis also provided an increased understanding of the physics and the interaction between different variables, by considering the physics behind the correlation of different predictors, and their groupings during the cluster analysis.

Principle Component Analysis is used to identify the number of underlying behavioural structures in the predictor data set. Each individual principle component represents a statistically uncorrelated behaviour within the dataset. These may or may not correspond directly to the original physical predictors, and may be a function of several predictors. Principle Component Analysis does not indentify which predictors are included in each 'component' group, or which combination of predictors could be used to accurately model the desired behavioural trend. As the current data set was measured by varying only shaft speed and throttle, this level of detail could not be extracted from the current dataset. A design of experiment approach to improve a future predictor data set is discussed in the following section.

In this investigation, therefore, it was assumed that the variance in the predictor dataset, due to the underlying behaviour captured by each of the N uncorrelated principle components, may be encapsulated by defining N uncorrelated groups of collinear predictors. The aim is to capture as much of the effect of the underlying behaviour on the predictor dataset as possible. Cluster Analysis was used to reduce the highly collinear predictors into less correlated 'families' of predictors. Knowledge of these families can provide additional physical insight into the interaction between the predictors that form each cluster. The grouping of flow and performance variables with covariates can alleviate some of the problems inherent in the specification of covariates. For example, the working line covariate can be replaced by the use of rotor efficiency, as done in this study. However, the assumption underlying the use of cluster analysis may be unacceptable, as the principle components may represent a behaviour that incorporates the interaction between several predictors.

Not being able to incorporate predictor interactions means that the final derived regression equations themselves are linear equations, formed by the use of Least Squares regression. In order to incorporate interaction effects that may capture the predictor variance of the principle components more accurately, an alternative structured approach to measurement, such as Design of Experiment, should be used. This is discussed further below in Section 4.11.

The specification of certain covariates could prove problematic in future studies. Covariates may have to be included in the prediction equation models. However, there is currently no method of describing these variables in a physical manner. For example, a fan liner can be described in terms of porosity, cell depth, or resistance. However, for this study these different liners were simply indexed by 1, 2, 3 etc. in order to distinguish between their different effects. Due to this indexing, only acceptance that different liners exist within each covariate group can be taken into account. Therefore the resulting prediction equations could not be applied to new liner architecture with confidence. This is a common problem when several covariates are present, but particularly affects liners, and intake forms (whether cylindrical or drooped, and angle of droop).

The approach of separating the broadband measured spectra into four averaged noise regions provides a simple method of calculating broadband noise for this study, despite the problems of overlapping bandwidths. An improvement would be the prediction of the complete broadband noise spectrum.

4.11. On the difficulties in deriving physical correlations

In this investigation no prior knowledge of the physics of fan broadband noise generation was assumed in an attempt to derive new broadband noise regression equations unrelated to those currently in use.

The difficulties encountered in deriving physically based fan broadband noise correlations may be due to the inadequate data sets available for investigation, in which a typical experimental procedure is to measure fan noise for decelerations along a particular working line. This procedure provides ‘linear effects’ within a larger multi-dimensional experimental space. By attempting to derive generally applicable physical correlation equations, we may be using these ‘linear effects’ in an attempt to derive ‘planar effects’.

To explain this effect imagine several ‘response sheets’ of different orientations, which may cross at a line. The topography of each ‘sheet’ is formed by the independent variation of several related predictors, and their effect on broadband noise. In other words, each response sheet corresponds to a ‘principle component’ of the predictor dataset. However, the variation along a fan working line does not allow the independent variation of many predictors in order to form these response sheets, providing instead a single ‘line’ of fan behaviour within the sheet domain. This line may correspond to the location along which several sheets cross, if the predictors are related to several principle components. Due to the high data collinearity the angle separating the sheets may not be derivable.

In order to improve the modelling of the principle components, each underlying behaviour described by a principle component must be isolated and varied independently. This will require identification of the predictors of which the principle components are a function, i.e. the axes of the 'response sheets'. The predictors may consist of both flow predictors and rig covariates. An experimental matrix can then be designed that will allow the variation of each isolated factor independently. This may require controlled variation of several combinations of simple flow predictors and rig covariates in order to isolate different behavioural factors and include interactions between parameters.

The regression equations derived during this study would then be improved by the inclusion of physical interactions between parameters, rather than the simple linear summing of different predictors. A number of statistical analysis techniques may be applied to the data sets in an attempt to derive these interactions. These techniques such as Analysis of Variance (ANOVA, discussed further below), assess predictors both independently and with respect to interactions. Unfortunately, an attempted application of these techniques to this data set gave statistical significance to many arrangements of the same variable (e.g. shaft speed (rpm) to the power of 0.5, 1, 2, or normalised by temperature etc.), despite the fact that on visual inspection of the data one format would clearly provide a better fit to the data. Several of the techniques suggested that all prediction fits were statistically significant, rather than one providing the 'best fit'. This in turn introduces difficulties when interpreting potential interactions between different predictors. For example it is not clear whether the interaction between flow Mach number and OGV stagger angle is more relevant than an interaction between Mach number squared and OGV stagger angle.

If the predictors chosen depend upon the data set used, then the effects of these predictors on broadband noise may not be statistically significant (and generally transferable to new rig predictions), and may only provide reliable predictions for that particular data set.

In addition to the difficulties associated with separation of the measured data and flow predictors, as mentioned previously, problems were met when deciding on how best to represent the covariates and their, often complicated, effects on the experimental data. These covariate effects are not systematically accounted for within this current measurement database. In order to alleviate this problem a more structured description of several covariates is required, specifically fan rig liners and fan intake form. These covariates should be parameterised in a way that allows variation in their design to be accounted for, i.e. it allows their physical differences to account for their effects on broadband noise predictions. Liners could be described in terms of cell depth, number of layers, facing sheet, and pore density. The rig intake could include such variables as angles of droop and rotation. This increase in flexibility would allow novel designs to be predicted more accurately without being part of the database used to derive the prediction equations.

Assuming an experimental approach is pursued to more clearly parameterise the covariates, a pre-defined method of understanding the effects of these covariates, and indeed the other flow and performance parameters, should be followed. The current standard rig noise test procedure is to perform a combination of fan deceleration and steady state measurements. These fan decelerations vary the fan speed and throttle size to track lines of constant thrust, and therefore the fan rig working lines. One future possibility is to use an experimental system based on the '*Design of Experiment*' (DoE) approach. Such methods include *Factorial Designs*, *Response Surface Designs*, and *Taguchi Designs*. All of these approaches allow the assessment of factors that affect the generation of broadband noise, and aid in the identification of interactions between predictors.

An important factor to take into consideration when preparing a designed experiment for a fan rig test, is whether the required performance points can actually be attained by the rig. When preparing an initial high-low factorial design, for example, it would be important for the designer to prepare points within the fan rig performance envelope, i.e. below the fan surge limit and above the fan stall limit.

If successful the results of a study such as this could allow increased physical analysis of each experiment and the creation over time of a more descriptive noise measurement database. A modular fan rig would greatly increase the ease with which such an investigation into factor variation could be performed, by increasing the speed of rig component replacement. Varying rig parameter components individually would be prohibitive in terms of time. However designed experiments allow the creation of test matrices within which combinations of parameters are varied simultaneously in a set order. This greatly reduces the number of runs required, and allows the understanding of interactions between predictors.

Thus far the investigations within this thesis have concentrated on analysis and understanding of fan broadband noise. This noise source is becoming more important as engine diameters grow, in an attempt to improve overall engine performance and reduce jet noise. In the competitive market of aero-engine design and manufacture, several technologies are being considered to allow further control of engine performance and noise, and reducing the importance of fan broadband noise. One of these technologies concerns the variation of engine exhaust area as a means of improving engine performance, fan flutter, and noise. Such a technology is holistic, as every engine parameter is affected, including the fan. The following section describes an investigation into the noise effects of a variable area nozzle being added to the bypass duct exhaust of several existing engines.

Chapter 5
Theory of cascade model for the prediction of broadband rotor-stator interaction noise

5. Theory of cascade model for the prediction of broadband rotor-stator interaction noise

This section will introduce the rotor/stator broadband noise interaction model that will be used later to perform a parameter study of a number of basic geometric and aerodynamic parameters, described in Chapters 6 and 7. The derivation below follows that presented in [11].

The basic model equation is presented and described below. The physical assumptions made in derivation are also presented. This is followed by description of the turbulence spectrum model that provides the representation of the turbulent wake impinging on the stators. The 'critical frequency' defined by Cheong et al [11] is defined along with its implications for the acoustic power spectrum, leading to the approximate expression for the acoustic power spectrum in a high frequency bandwidth.

In deriving the equation for the rotor-stator interaction broadband model, the theory described by Cheong et al [11] is closely followed. The derivation of the broadband noise model equation assumes a 2-dimensional cascade of flat plate aerofoils with a stagger angle equal to θ. The incoming flow is also assumed to be 2-dimensional, with a flow direction parallel to the aerofoil chord so that there is zero angle of incidence. Taylor's frozen turbulence assumption is made, i.e. the magnitude of the turbulent velocity fluctuations w are much less than that of the mean velocity W. Assume a harmonic gust incident upon the cascade, of the form:

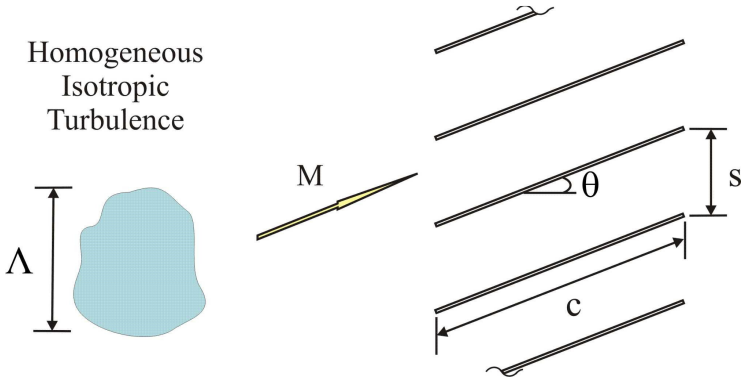

Figure 5-1. Representation of modelled cascade

$$w(y_1, y_2, t) = w_0 e^{i[k_1(y_1 - Wt) + k_2 y_2]} \qquad \text{Eq (5-1)}$$

which is assumed to convect with the mean flow. Here w is the upwash velocity perturbation of amplitude w_0 convected at mean velocity W, comprising of wavenumbers k_1 and k_2, where k_1 is the acoustic wave number in the chordwise direction and k_2 the acoustic wave number in the gapwise direction. Following Smith the acoustic pressure generated by this gust impinging on the cascade is of the form:

$$p^{\pm}(x_1,x_2,t)=\rho_0 W w_0 \sum_{r=-\infty}^{\infty} R_r^{\pm} e^{i(k_1 Wt+\alpha_r x_1+\beta_r x_2)} \qquad \text{Eq (5-2)}$$

where $R_r^{\pm}$ is the cascade response function $R_l^{\pm}$ which couples the impinging turbulent fluctuations to the acoustic pressure. The superscript ± denotes noise propagation upstream (+) and downstream (-) respectively. $R_l^{\pm}$ is completely defined by the parameters $R_l^{\pm}=R_l^{\pm}(\%_c,\theta,M,\sigma,\lambda)$ where σ is the phase angle and $\lambda=\omega c/W$ is the reduced frequency.

From Equation 5-2 it is seen that each incoming harmonic gust generates an infinite number of scattered acoustic waves $(r=-\infty,...,-1,0,1,...,\infty)$. A single wave number component of vorticity (k_1, k_2) generates an r^{th} acoustic wave with a phase angle $\beta_r s$ between adjacent blades. This phase angle has the form:

$$\beta_r s=\sigma-2\pi r \qquad \text{Eq (5-3)}$$

The acoustic circumferential wave number β_r of the r^{th} acoustic wave is therefore given by:

$$\beta_r=\frac{(k_1\sin\theta+k_2\cos\theta)s-2\pi r}{s} \qquad \text{Eq (5-4)}$$

The axial acoustic wave number is expressed in terms of β_r and ω by the quadratic expression

$$\alpha_r^{\pm}=\frac{M_1(\omega/a+M_2\beta_r)\pm\sqrt{(\omega/a+M_2\beta_r)^2-(1-M_1^2)\beta_r^{\,2}}}{1-M_1^2} \qquad \text{Eq (5-5)}$$

Equation 5-2 is only valid for a harmonic gust, this can be generalised to model the acoustic pressure radiated by a cascade subject to a turbulent gust by the equation

$$p^{\pm}(x_1,x_2,t)=\rho_0 W\int_{-\infty}^{\infty}\int_{-\infty}^{\infty}\hat{\hat{w}}(k_1,k_2)\sum_{r=-\infty}^{\infty}R_r^{\pm}(k_1,k_2)\times e^{i\left(k_1 Wt+\alpha_r^{\pm}x_1+\beta_r x_2\right)}dk_1dk_2 \qquad \text{Eq (5-6)}$$

The 2-dimensional wave-number spectrum of turbulence is denoted by $\hat{\hat{w}}(k_1k_2)$. The double hat of the turbulence spectrum signifies that the spectrum is evaluated in the moving reference frame. According to Goldstein [23] the spectral density of acoustic intensity in a fluid moving at a uniform velocity is given by:

$$I^{\pm}(\omega)=\lim_{T\to\infty}\frac{\pi}{T}\mathrm{Re}\left\{\left(\frac{\tilde{p}_T(\omega)}{\rho_0}+U_1\tilde{u}_{1,T}^{\pm}(\omega)+U_2\tilde{u}_{2,T}^{\pm}(\omega)\right)\times\left(\rho_0 u_{1,T}^{\pm *}(\omega)+\frac{U_1\tilde{p}_T^{*}(\omega)}{a^2}\right)\right\} \qquad \text{Eq (5-7)}$$

where U_1 and U_2 are the mean flow velocity components in the chordwise and gapwise directions, $\tilde{u}_1$ and $\tilde{u}_2$ are the acoustic particle velocities in the respective directions. The stars denote complex conjugate. The Fourier transform with respect to time of Equation 5-6 becomes:

$$p_T^{\pm}(\mathbf{x},\omega)=\rho_0\int_{-\infty}^{\infty}\hat{\tilde{w}}(K_1,k_2)\sum_{r=-\infty}^{\infty}R_r^{\pm}(K_1,k_2)e^{i\left(\alpha_r^{\pm}x_1+\beta_r x_2\right)}dk_2 \qquad \text{Eq (5-8)}$$

where $K_1=\omega/W$. Substituting Equation 5-8 into the linearised momentum equation gives the particle velocities $\tilde{u}_1$ and $\tilde{u}_2$. Substituting these into Equation 5-7 and assuming that the velocities at different wave numbers are uncorrelated, i.e. the turbulence is homogeneous:

$$\lim_{T\to\infty}\frac{\pi}{T}E\left[\hat{\tilde{w}}(K_1,k_2)\hat{\tilde{w}}^{*}(K_1,k_2')\right]=W\delta(k_2-k_2')\Phi_{ww}(K_1,k_2') \qquad \text{Eq (5-9)}$$

gives Equation 5-10 for the acoustic intensity spectrum where $\Phi_{ww}(K_1,k_2')$ is the turbulence wave number spectrum in the moving reference frame.

$$I^{\pm}(\mathbf{x},\omega)=\rho_0 M\int_{-\infty}^{\infty}\Phi_{ww}(K_1,k_2)\sum_{r=-\infty}^{\infty}\sum_{r'=-\infty}^{\infty}\times\mathrm{Re}\left\{\begin{array}{l}\dfrac{\omega\left(-\alpha_{r'}^{\pm *}+M_1\left(\omega+U_1\alpha_{r'}^{\pm *}+U_2\beta_{r'}\right)\right)}{\left(\omega+U_1\alpha_r^{\pm}+U_2\beta_r\right)\left(\omega+U_1\alpha_{r'}^{\pm *}+U_2\beta_{r'}\right)}\\ \times R_r^{\pm}(K_1,k_2)R_{r'}^{\pm *}(K_1,k_2)e^{i\left(\left(\alpha_r^{\pm}-\alpha_{r'}^{\pm *}\right)x_1+(\beta_r-\beta_{r'})x_2\right)}\end{array}\right\}dk_2 \qquad \text{Eq (5-10)}$$

The acoustic power per unit span can be calculated by integrating Equation 5-10 over a distance *Bs*, i.e. over the circumferential length of the 2-dimensional cascade if rolled up. The gap-wise wave numbers are periodic over *Bs*, and this introduces a Kronecker delta function on integration over x_2

$$\int_0^{Bs}e^{i(\beta_r-\beta_{r'})x_2}dx_2=Bs\,\delta_{rr'} \qquad \text{Eq (5-11)}$$

This Kroneker delta allows the r' summation in Equation 5-10 to be removed, and the acoustic power spectrum per unit span is to be written in the form

$$p^{\pm}(\omega) = \rho_0 MBs \int_{-\infty}^{\infty} \Phi_{ww}(K_1, k_2) \sum_{r=-\infty}^{\infty} \left| R_r^{\pm}(K_1, k_2) \right|^2 \times \frac{\omega \mathrm{Re}\left\{ -a\alpha_r^{\pm} + M_1\left(\omega + U_1\alpha_r^{\pm} + U_2\beta_r\right)\right\}}{\left|\omega + U_1\alpha_r^{\pm} + U_2\beta_r\right|^2} dk_2 \qquad \text{Eq (5-12)}$$

The incoming turbulence must be periodic in the circumferential direction, with basic spatial period equal to *Bs*, the circumference of the cascade. Therefore by geometry the wavenumber in the x_2 direction must satisfy

$$k_{2,m} = \frac{2\pi m}{Bs\cos\theta} - K_1 \tan\theta \qquad \text{Eq (5-13)}$$

In order to integrate Equation 5-12 over k_2 at a constant frequency, or K_1, the wave number must be replaced by

$$k_{2,m} \to \frac{2\pi\Delta m}{Bs\cos\theta} \qquad \text{Eq (5-14)}$$

where $\Delta m = 1$. Therefore the remaining integral in Equation 5-12 can be replaced by the summation:

$$p^{\pm}(\omega) = \frac{2\pi\rho_0 M}{\cos\theta} \sum_{m=-\infty}^{\infty} \Phi_{ww}(K_1, k_2) \sum_{r=-\infty}^{\infty} \left| R_r^{\pm}(K_1, k_2) \right|^2 \times \frac{\omega \mathrm{Re}\left\{ -a\alpha_r^{\pm} + M_1\left(\omega + U_1\alpha_r^{\pm} + U_2\beta_r\right)\right\}}{\left|\omega + U_1\alpha_r^{\pm} + U_2\beta_r\right|^2} \qquad \text{Eq (5-15)}$$

From Eq (5-15) it is clear that the turbulence consists of an infinite sum of vortical waves of order *m* each of which interacts with the stator blade, generating an infinite number of acoustic modes with scattering index *r*. The radiated sound is therefore a sum of these generated acoustic modes.

Firstly the cascade response function $R_r^{\pm}$ is within both summations of *m* and *r* which is very inefficient computationally. Transforming the variables over which the summation is performed allows the term $R_r^{\pm}$ to be moved from the double summation to a single summation. The turbulence spectrum Φ_{ww} then moves under the double summation, which is acceptable, however, as the turbulence spectrum in this case is calculated from an algebraic expression (c.f. Section 5.1), and can be performed quickly. The cascade response function requires another infinite summation of the 'cascade-waves' and the numerical computation of the upwash integral equation in [43].

The acoustic wave number in the x_2 direction must satisfy;

$$\beta_l = \frac{2\pi}{Bs} l \qquad \text{Eq (5-16)}$$

The integer l represents the order of the acoustic mode in the x_2 direction, and is equivalent to the circumferential mode number m in duct theory. Insertion of Equations 5-16 and 5-13 into Equation 5-4 gives:

$$m = l + Br \qquad \text{Eq (5-17)}$$

This equation relates the m^{th} vortical wave number to the acoustic mode number l and the cascade scattering index r. This is the scattering rule for the generation of acoustic modes by the interaction of a vortical mode with a cascade. Equation 5-17 can be substituted into Equation 5-13, the result of which can in turn be substituted into Equation 5-15, which after rearrangement results in:

$$p^{\pm}(\omega) = \frac{2\pi\rho_0 M}{\cos\theta} \sum_{l=-\infty}^{\infty} Q_l^{\pm}(K_1) \sum_{r=-\infty}^{\infty} \Phi_{ww}(K_1, k_{2,l+Br}) d\omega \qquad \text{Eq (5-18)}$$

The term $Q_l^{\pm}(K_1)$ is a non-dimensional modal power response function:

$$Q_l^{\pm}(K_1) = \left|R_l^{\pm}(K_1, k_{2,\mathrm{mod}(l,B)})\right|^2 \frac{\omega \mathrm{Re}\left\{-a\alpha_l^{\pm} + M_1(\omega + U_1\alpha_l^{\pm} + U_2\beta_l)\right\}}{\left|\omega + U_1\alpha_l^{\pm} + U_2\beta_l\right|^2} \qquad \text{Eq (5-19)}$$

where $\mathrm{mod}(l, B)$, is the remainder when the first term is divided by the second.

Note that the summation over l is restricted to a finite range of values by only taking into account the cut-on modes. In a subsonic flow ($W < a$) propagating modes occur over the range of β_l given by

$$\frac{M_2 - (1 - M_1^2)^{1/2}}{1 - M^2}\omega \le a\beta_l \le \frac{M_2 + (1 - M_1^2)^{1/2}}{1 - M^2}\omega \qquad \text{Eq (5-20)}$$

The maximum and minimum integers of the acoustic mode number l are denoted L_{max} and L_{min} respectively, corresponding to acoustic modes travelling with, and against, the swirl velocity U_2 respectively. The acoustic power spectrum per unit span can therefore be written as:

$$p^{\pm}(\omega) = \frac{2\pi\rho_0 M}{\cos\theta} \sum_{l=L_{\min}}^{L_{\max}} Q_l^{\pm}(K_1) \sum_{r=-\infty}^{\infty} \Phi_{ww}(K_1, k_{2,l+Br}) \qquad \text{Eq (5-21)}$$

In Equation 5-21 the range of the cascade scattering index *r* is chosen to ensure convergence. The sound power integrated over the frequency bandwidth $\omega_L \le \omega \le \omega_H$ is therefore:

$$\Pi^{\pm} = \frac{2\pi\rho_0 M}{\cos\theta}\int_{\omega_L}^{\omega_H}\sum_{l=L_{\min}}^{L_{\max}} Q_l^{\pm}(K_1)\sum_{r=-\infty}^{\infty}\Phi_{ww}(K_1, k_{2,l+Br})d\omega \qquad \text{Eq (5-22)}$$

To summarise Eq (5-22), the turbulence spectrum $\Phi_{ww}(K_1, k_{2,l+Br})$ provides the turbulent fluctuating velocities of the incoming wake. The fluctuating velocities are coupled to the generated acoustic pressure fluctuations by the cascade response function $Q_l^{\pm}(K_1)$. These terms are then integrated over a specified frequency band, and multiplied by a number of factors affecting the magnitude of the resultant acoustic sound power.

Finally, the acoustic spectra presented in the parameter study are expressed as a sound power level *PWL*, defined by:

$$PWL^{\pm} = 10\log_{10}\left(\frac{2\Pi^{\pm}\Delta R}{10^{-12}}\right) \qquad \text{Eq (5-23)}$$

In the above expression the factor of 2 is included to convert from a two-sided spectrum to a one-sided spectrum, and ΔR denotes the width of the cascade in the spanwise direction. The reference power is 10^{-12} W.

There are a number of limitations inherent in the model described above. The use of a 2-dimensional cascade of flat plates neglects to take the effects of vane thickness or camber into account. However, more importantly the assumption that the wake flow is always impinging perfectly onto the vane leading edges means that an angle of attack between the flow direction and the vane chord cannot be taken into consideration. This has an effect on the second parametric study, investigating the effect of variation in fan design parameters on broadband noise, discussed further in Chapter 7.

5.1. Turbulence spectra

The turbulent wakes generated by turbofan rotors have been found to have similarities to isotropic turbulence by both Ganz et al [16] and Gliebe et al [21]. Isotropic turbulence is therefore a reasonably valid assumption despite the complex, highly non-homogenous nature of the wakes. There are two commonly used spectra satisfying these requirements, the von Karman spectrum and the Liepmann spectrum. Atassi and Logue [8] find that at lower frequencies the difference between the Liepmann

and Von Karman models is approximately 2dB. This difference reduces to less than 1dB at higher frequencies. Either model may therefore be used to calculate the sound power spectra. The Liepmann spectrum is chosen, the three dimensional form of which is:

$$\Phi_{ww}(k_1,k_2,k_3)=\frac{2\overline{w^2}\Lambda^3}{\pi^2}\frac{\Lambda^2\left(k_1^2+k_3^2\right)}{\left[1+\Lambda^2\left(k_1^2+k_2^2+k_3^2\right)\right]^3} \qquad \text{Eq (5.1-1)}$$

where Λ is the turbulence integral length scale, and $\overline{w^2}$ is the mean squared value of turbulent velocity fluctuations normal to the aerofoil chord. Integrating over k_3 give the required two dimensional spectrum of the form:

$$\Phi_{ww}(k_1,k_2)=\frac{\overline{w^2}\Lambda^3}{4\pi^2}\frac{\left[1+\Lambda^2\left(4k_1^2+k_2^2\right)\right]}{\left[1+\Lambda^2\left(k_1^2+k_2^2\right)\right]^{5/2}} \qquad \text{Eq (5.1-2)}$$

5.2. Critical Frequency

In Reference [11] a 'critical frequency' ω_c is defined that separates the acoustic power spectrum into two frequency regions. It is defined as the lowest frequency at which the acoustic mode number in the circumferential direction l equals the number of vanes V, and is calculated using Equation 5.2-1 below:

$$\omega_c=\frac{1-M^2}{M_2+\left(1-M_1^2\right)^{1/2}}\frac{2\pi a}{s} \qquad \text{Eq (5.2-1)}$$

The significance of the critical frequency is that when $l=V$, the wavelength of the acoustic mode in the circumferential direction is equal to the vane spacing s. Above this critical frequency the number of cut-on acoustic modes whose circumferential wavelengths are less than s increases. These shorter wavelengths are expected to have relatively weak interaction with the cascade, as the waves pass straight through the cascade with little interaction.

Secondly, it may be shown that at the critical frequency all turbulence components excite cut-on (i.e. propagating) acoustic modes. Below the critical frequency only some of the wave number components excite cut-on acoustic modes. It is therefore shown in Reference [11] that below the critical frequency the unsteady blade loading between adjacent blades is partially coherent and the sound power is not proportional to the number of vanes. Above the critical frequency the unsteady blade loading between adjacent vanes is coherent and the radiated sound power is approximately proportional to the number of vanes V. This behaviour above the critical frequency allows the derivation of an analytic expression

for the acoustic power spectrum that can be applied in this frequency region. This expression is described below in Section 5.3.

It is useful to compare ω_c to the blade passing frequency ω_{BPF}, where $\omega_{BPF} = B\Omega$, where B is the number of blades, and Ω is the rotor shaft speed. Given that $s = 2\pi R/V$, where R is an arbitrary radial position, then the critical frequency can be related to the shaft speed by Eq (5.2-2) below

$$\frac{\omega_c}{\omega_{BPF}} = \frac{1-M^2}{M_2 + \left(1-M_1^{\,2}\right)^{1/2}} \frac{V}{B} \frac{a}{R\Omega} \qquad \text{Eq (5.2-2)}$$

The ratio of ω_c/ω_{BPF} is therefore directly proportional to the ratio of number of vanes to number of blades *V/B*. Comparing results for the Engine 3 at cruise, cutback and approach shaft speeds, the critical frequency is calculated to be approximately 1.6, 1.8, and 3.65 times the blade passing frequency, respectively. Therefore at lower shaft speeds the sound power generated by incoherent blade responses covers a smaller frequency range of the acoustic spectra than the sound power spectra generated at higher shaft speeds. The critical frequency increases in importance with shaft speed, moving through the frequency range between second and third blade passing frequency. This frequency range is considered to be important from a perceived noise level perspective. For very high shaft speeds the critical frequency does not pass below the first blade passing frequency.

5.3. Approximate expression for acoustic power spectrum

Cheong et al [11] have derived an approximate expression for the acoustic sound power per unit span above the critical frequency, of the form:

$$P^{\pm}(\omega) \approx F^{\pm}(M,\theta) \frac{B\rho_0 \Lambda \overline{w}^2 W}{2\pi^2 \omega} \frac{M\left(1-M_1^{\,2}\right)^{1/2}}{\left(1-M^2\right)} \frac{\left(1+3\Lambda^2 K_1^{\,2}\right)}{\left(1+\Lambda^2 K_1^{\,2}\right)^2} \qquad \text{Eq (5.3-1)}$$

where $F^{\pm}$ is an empirical function that depends only on M and θ, and $K_1 = \omega/W$. In this equation it has been assumed that Φ_{ww} is a slowly varying function of k_2, and the turbulent integral length scales are small compared to the blade spacing. From the formulation of Eq (5.3-1) it is also apparent that the acoustic power above the critical frequency is proportional to the blade number, and is independent of blade chord and cascade solidity.

The function $F^{\pm}(M,\theta)$ has been expressed in the form of the polynomial $F^{\pm}(M,\theta) = \sum_{m=0}^{2} \sum_{n=0}^{4} a_{m,n}^{\pm} \theta^n M^m$, with coefficients given by:

n		m 0	1	2
0	$a^{+}_{0,m}$	1.06902	-2.07280	1.00861
	$a^{-}_{0,m}$	1.50791	3.95533	-5.24509
1	$a^{+}_{1,m}$	-1.08014	1.29047	-0.0643443
	$a^{-}_{1,m}$	1.69650	-12.8537	13.7227
2	$a^{+}_{2,m}$	2.09042	-2.11989	-0.174012
	$a^{-}_{2,m}$	-3.35771	23.7866	-29.1403
3	$a^{+}_{3,m}$	-0.712208	1.20546	-0.451791
	$a^{-}_{3,m}$	2.88637	-22.7343	28.2291
4	$a^{+}_{4,m}$	0	0	0
	$a^{-}_{4,m}$	-0.944190	7.56542	-9.18514

Table 7 –Coefficients of $\mathbf{F}^{\pm}(\mathbf{M},\theta)$ for use in high frequency approximation

Chapter 6
Variation of Broadband noise with basic fan stage parameters

6. Variation of Broadband noise with basic fan stage parameters

This chapter describes the results of a parameter study of the broadband noise generated by a hypothetical fan stage using the noise model described in Chapter 5. The effect on rotor-stator broadband noise of simple geometric and aerodynamic parameters on predicted broadband noise is investigated, above and below the critical frequency f_c. The parameters investigated are varied about a nominal cascade configuration, given by

- Number of vanes V 30
- Mach number M 0.5
- Stagger angle θ 30^o
- Duct radius (m) R 0.8
- Strip size (m) ΔR 0.4 (R/2)
- Turbulence intensity w^2/W^2 0.0004
- Turbulence length scale λ/R 0.035
- Space/chord ratio s/c 0.8

Note that this is the same nominal cascade geometry as used in [11]. This number of vanes is not representative of a real engine geometry. For a real fan stage standard practice is to design so the first blade passing frequency is cut-off. This requires the number of vanes to be greater than twice the number of fan blades, which is therefore greater than 30.

6.1. Results of variations in cascade parameters

The broadband noise model of Chapter 5 makes clear that the cascade geometry is completely defined by

- Number of Vanes V
- Blade chord length c and Space/Chord ratio s/c
- Stagger angle θ

6.1.1. Variation of Broadband Noise with Number of Vanes (V)

The number of vanes is an important parameter as not only does it correspond to the number of leading edge sources, but it also affects the vane spacing s in the cascade, and therefore the space/chord ratio s/c, and hence the interaction between vanes. Therefore the broadband noise was

investigated for increasing number of vanes at constant c, and constant s/c. The nominal cascade is investigated but with the variation in vane number:

- Number of Vanes V 5:5:60

In the first instance, space/chord ratio s/c is kept constant, therefore as s decreases with increasing V, c also decreases to maintain the space/chord ratio

- Space/chord ratio s/c 0.8

In the second example the blade chord is kept constant, therefore

- Vane Chord (m) c 0.5
- Vane spacing (m) s $2\pi R / V$

The critical frequency f_c , defined by Eq (5.2-1), for the various values of V are given by:

V	f_c (Hz)	V	f_c (Hz)
5	220.30	35	1542.12
10	440.60	40	1762.42
15	660.91	45	1982.72
20	881.21	50	2203.02
25	1101.51	55	2423.32
30	1321.81	60	2643.63

Table 8 – Variation of critical frequency with number of vanes

The critical frequency is a function of vane spacing, and therefore varies with the number of vanes. High and low frequency bands are therefore chosen to be consistently outside the range of variation of the critical frequency. The frequency band below f_c is between 160.0Hz and 320.0Hz, and the high frequency band is between 3225.4Hz and 8127.5Hz. The upstream and downstream sound power spectra in 1/3rd octave bands for the baseline case are plotted in Figure 6.1.1-1, for V = 30 and s/c = 0.8. The low and high frequency bands for this case can also be seen in Figure 6.1.1-1.

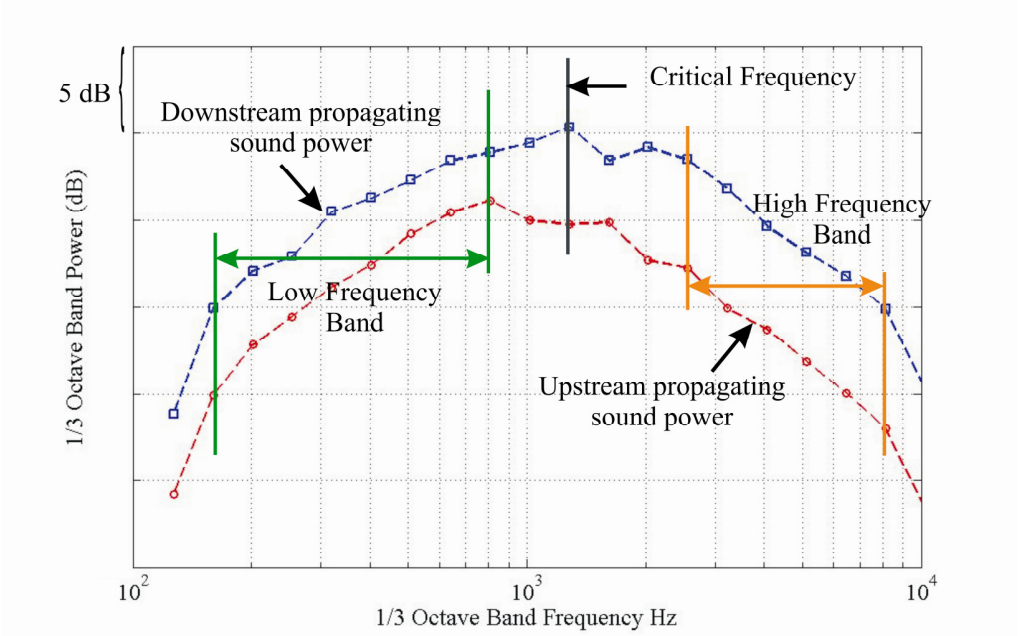

Figure 6.1.1-1 – 1/3 Octave power spectra for low and high frequency bandwidths upstream and downstream, along with critical frequency, $V = 30$, $s/c = 0.8$

Figure 6.1.1-2a and b display 1/3rd octave sound power spectra, propagating downstream and upstream respectively. Sound power spectra are overlaid for $V = 10:10:60$.

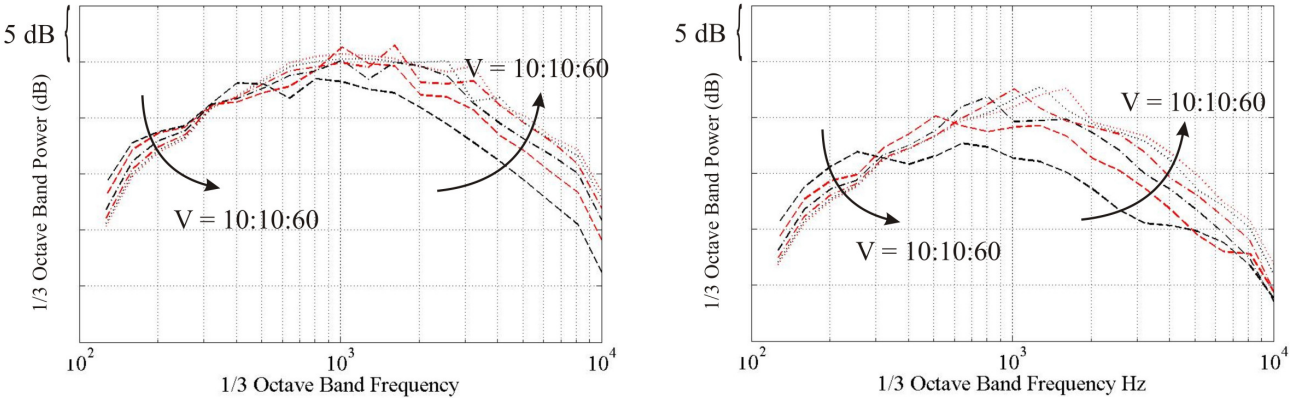

a – Downstream sound power, varying V with constant chord

b - Upstream sound power, varying V with constant s/c

Figure 6.1.1-2 – Variation of sound power spectra with $V = 10:10:60$

It is clear from both Figure 6.1.1-2a and b that as V increases, the sound power decreases at low frequencies, and increases at high frequencies. In Figure 6.1.1-2 the spectra appear to rotate about a 'pivot' frequency at approximately 320 Hz. The frequencies of maximum sound power propagating downstream, seen for example in Figure 6.1.1-2a, correspond approximately to the critical frequency. This is generally true for downstream sound power spectra displayed in this initial parametric study

(Chapter 6), though not the upstream sound power spectra. The peak in downstream sound power may correspond to a resonance effect associated with the acoustic wavelength of the critical frequency.

Figure 6.1.1-3a and b show the sound power variation of upstream propagating sound power, for constant chord, and constant space/chord ratio, integrated over the high frequency bandwidth indicated in Figure 6.1.1-1, for $V = 10:5:60$.

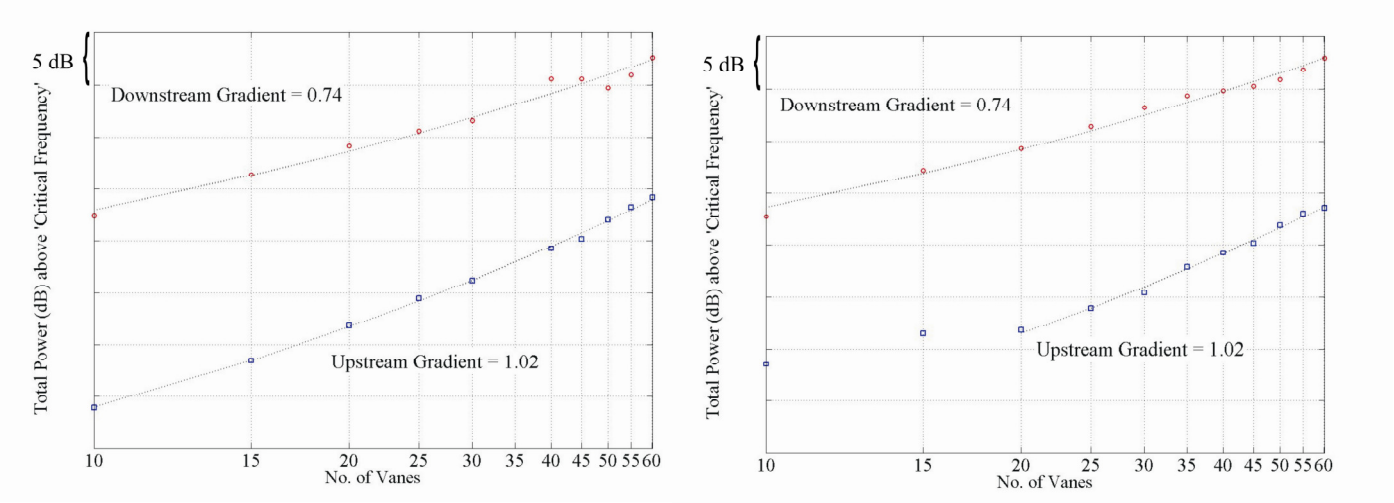

a – Variation in sound power with V, constant chord

b – Variation in sound power with V, constant space/chord ratio

Figure 6.1.1-3 – Variation of sound power with number of vanes, integrated over the frequency band above f_c

These figures demonstrate that the rate of increase of sound power with number of vanes is similar when the vane chord length and the space/chord ratio are held constant. The sound power propagating upstream in the high frequency bandwidth increases approximately linearly with the number of vanes. The scaling power law of 1.02 suggests that each vane acts independently. This result agrees with the findings of, for example, Ganz et al [16]. However, for the downstream sound power a weaker vane-count dependence is observed of approximately $W \propto V^{0.75}$. This result for downstream sound propagation is unexpected, as from experimental studies (such as Woodward et al [46]) it is found that the sound levels in both directions increase with the number of blades at these high frequencies. The slower increase in downstream sound power suggests an interaction effect between adjacent blades, whereby increasing the number of vanes does not increase the number of sources linearly.

Figure 6.1.1-4a and b below show the variation of sound power integrated over the frequency bandwidths below the critical frequency versus $V = 10:5:60$.

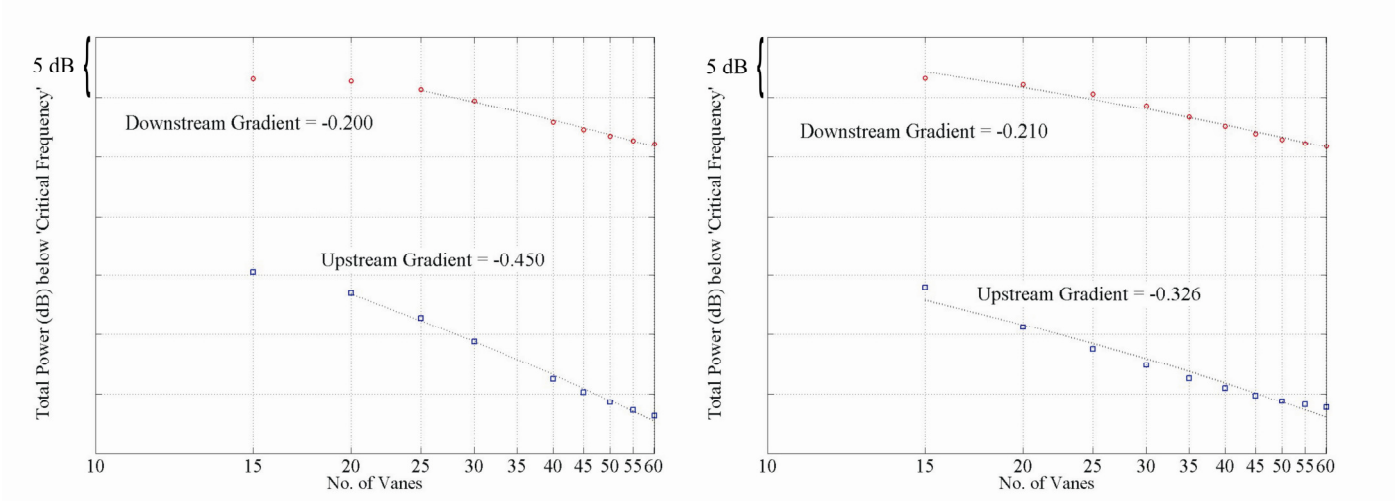

a – Variation in sound power with V, constant chord

b – Variation in sound power with V, constant space/chord ratio

Figure 6.1.1-4 - Variation of average sound power with number of vanes, frequency band below f_c

In contrast to Figure 6.1.1-3, sound power below the critical frequency reduces very slowly with increasing V. Both the downstream and upstream sound power appear to peak for approximately $V = 15$. The upstream sound power reduces more rapidly with V when the chord is held constant, compared with the sound power reduction when space/chord ratio is kept constant. This suggests that at these low frequencies when not all turbulence wavenumbers contribute to the predicted sound power, the unsteady blade loading between adjacent blades is negatively correlated, such that increasing the number of vanes reduces the overall efficiency of the cascade.

The smallest number of vanes predicted is 10, it is unclear whether for lower numbers of vanes the low frequency sound power decreases. A decrease in sound power for even lower numbers of vanes would be expected; as vane count decreases each vane becomes an independent source.

6.1.2. Variation of Broadband Noise with Blade chord (*c*)

The variation of sound power with chord when all other parameters are held constant is now investigated. The cascade of this investigation has the same parameters as the nominal cascade, with variation in chord now given by:

- Chord length c 0.1:0.1:2
- Vane spacing s $2\pi R/V$

The critical frequency in this case is 1322Hz and is independent of chord. The low frequency band below f_c is chosen to be between 160Hz and 806Hz, and the frequency band above f_c is between centre frequencies of 2560Hz, and 8128Hz.

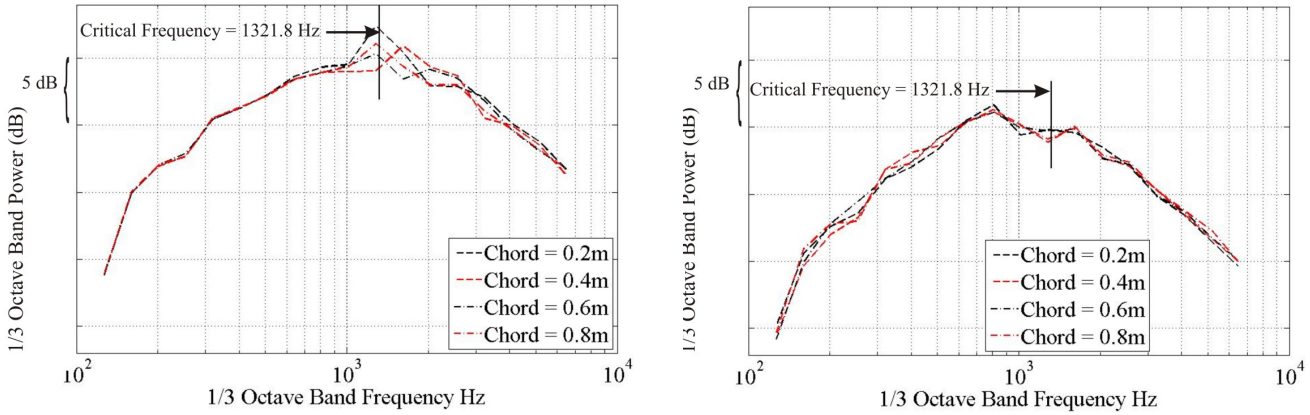

a – Downstream sound power **b – Upstream sound power**

Figure 6.1.2-1 – Variation of sound power with vane chord

Figure 6.1.2-1a and b above show that the sound power in the low and high frequency bands are generally independent of chord. The exception is at the critical frequency f_c on the downstream sound power spectra. This weak sensitivity to chord is because in a cascade the sound power generated predominantly at the vane leading edge, with the trailing edge being of secondary importance. Note that the chord is of importance for isolated aerofoils.

6.1.3. Variation of Broadband Noise with Stagger angle θ

The final geometric parameter investigated in this chapter is the stator vane stagger angle θ. It is assumed here that the stagger angle affects only the geometry of the cascade, not the loading on the vanes as the incoming turbulence is assumed to be convected parallel to the vane chord. The cascade is as for the Nominal case with the following variation in stagger angle:

- Stagger angle θ 0^o: 5^o: 75^o

The critical frequency for the range of θ values between 0° and 75° is tabulated below:

θ Degs	f_c (Hz)	θ Degs	f_c (Hz)
0	1757.36	40	1222.29
5	1671.15	45	1180.73
10	1589.98	50	1144.33
15	1514.27	55	1112.86
20	1444.28	60	1086.11
25	1380.12	65	1063.85
30	1321.81	70	1045.91
35	1269.26	75	1032.12

Table 9 – Variation of critical frequency with stagger angle

The low frequency band below f_c is therefore between centre frequencies 160Hz and 806Hz, and the frequency band above f_c is between centre frequencies 2560Hz, and 8128Hz.

Figure 6.1.3-1 below shows the variation of upstream sound power for varying stagger angles between $10^\circ : 10^\circ : 60^\circ$:

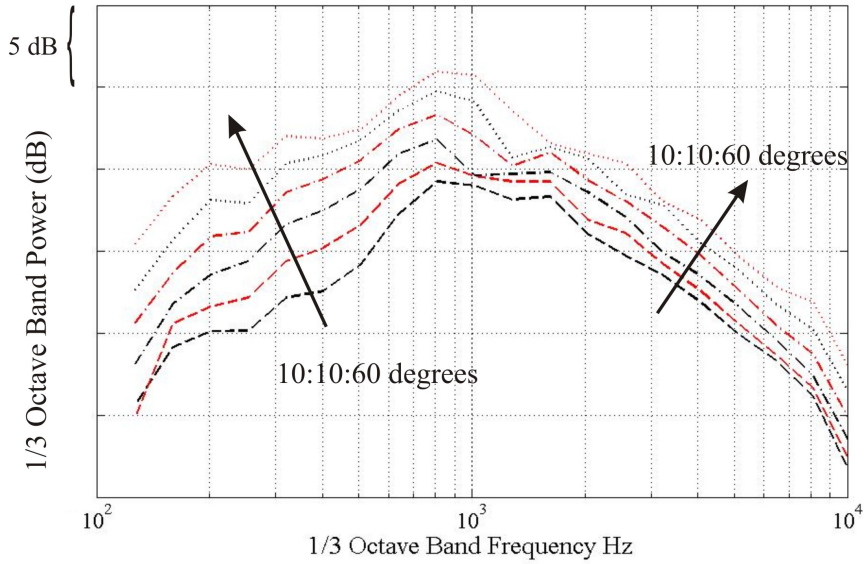

Figure 6.1.3-1 – Variation of sound power propagating upstream with stagger angle θ

Figure 6.1.3-1 suggests that increasing the stagger angle increases the total sound power level over the entire frequency range, with a faster increase at lower frequencies. The corresponding variation for the downstream sound power spectrum is plotted in Figure 6.1.3-2

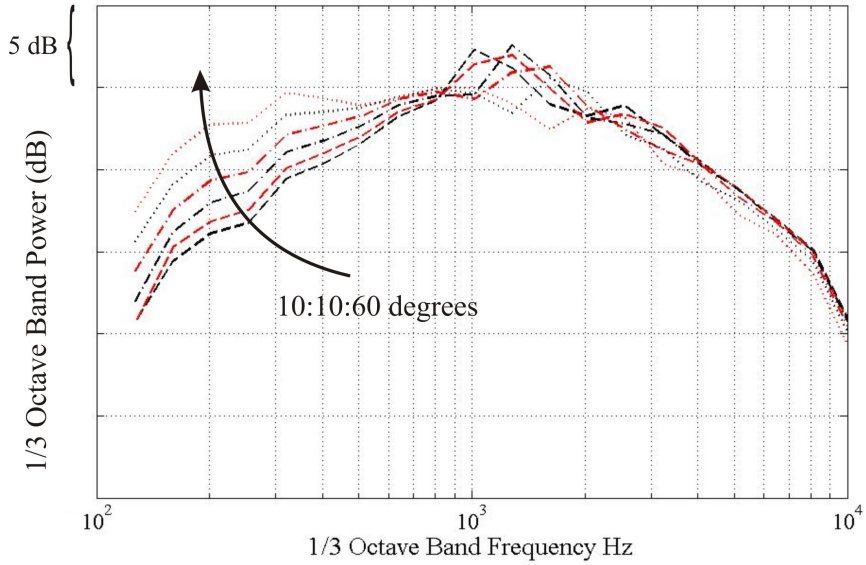

Figure 6.1.3-2 – Variation of sound power propagating downstream with stagger angle θ

Figure 6.1.3-2 suggests that for the downstream power, the low frequency sound power increases for increasing stagger angle, and decreases slightly at the higher frequencies. There appears to be a 'pivot' frequency at approximately 840Hz at which the sound power is independent of θ. At frequencies just above this frequency each spectrum displays a peak in the vicinity of the critical frequencies, above which the downstream sound power appears to be weakly dependent on θ.

Figure 6.1.3-3a and b show the variation of the integrated sound power with θ, both above and below f_c.

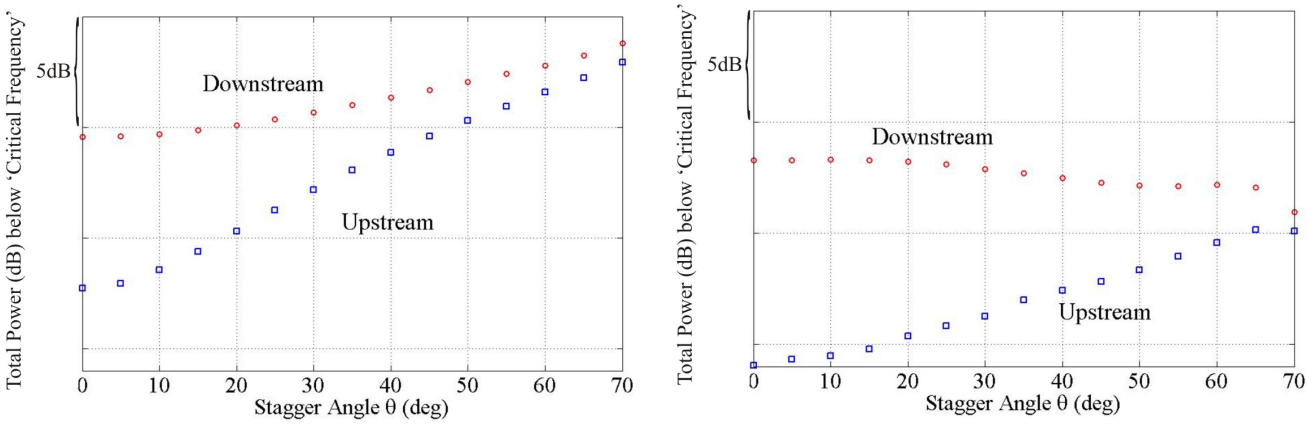

a – Variation of sound power below f_c **b –Variation of sound power above f_c**

Figure 6.1.3-3 – Variation of average sound power with stagger angle θ

As the stagger angle θ increases above 70° the upstream and downstream sound power spectra converge. Note that a stagger angle of 70° is extremely large and beyond current design, where OGV leading edge stagger angle is generally of the order of 20° (note that OGV vanes on a real engine are cambered, which the current noise model does not consider). This limiting stagger angle is also found by Cheong et al [11] who have derived an approximate expression for the sound power spectral shape above f_c, given by Equation 5.3-1.

Jurdic and Joseph [29] have investigated in detail the generation of acoustic modes by the cascade used in this investigation, and whether these modes propagate upstream or downstream. They derive an ellipse on the circumferential and axial wave number axes. This ellipse defines the cut-on wave number limits, and the relationship between each cut-on circumferential and axial wave number. The orientation of the major axis of this ellipse is controlled by the cascade stagger angle. Also derived on the same axes is a group velocity circle that indicates the direction of propagation of the acoustic energy of these modes. The centre of this circle is a function of the axial (M_1) and gap-wise (M_2) flow Mach numbers onto the cascade, and the circle radius is equal to c_0. These geometries are indicated on the schematic shown below in Figure 6.1.3-4. The results of Jurdic and Joseph indicate the complexity of the influence of stagger angle on the broadband noise generated by a rectilinear cascade of 2-dimensional flat plates. For further information and a full discussion of these effects see [29].

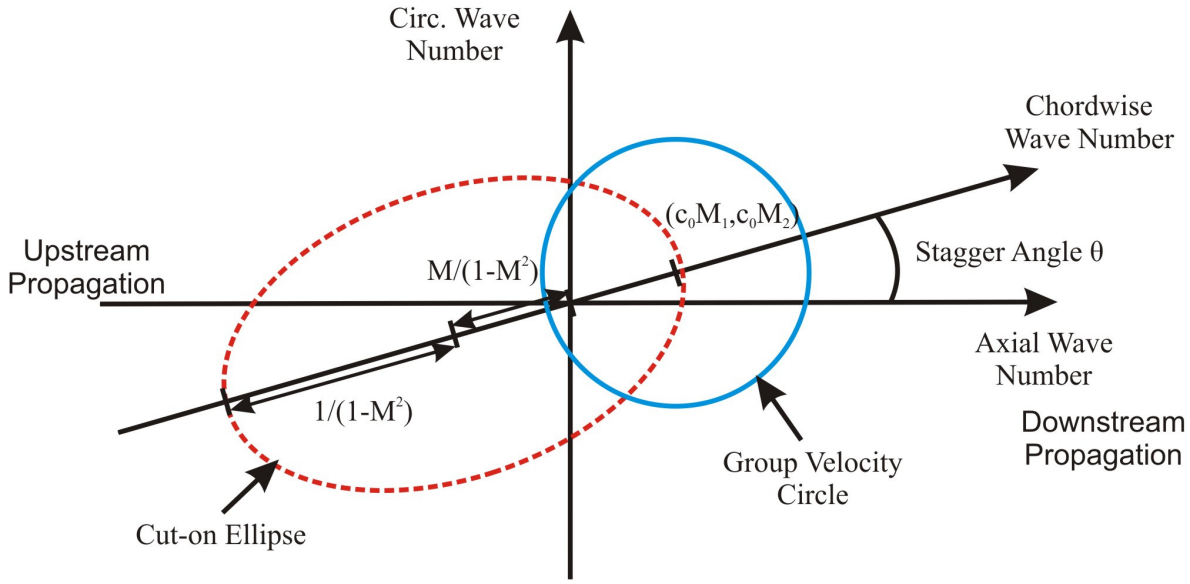

Figure 6.1.3-4 – Cut-on wave number ellipse and group velocity circle, defined by Jurdic and Joseph [29]

6.2. Broadband Sound Power Variation with Aerodynamic Parameters

In this section the effect on broadband noise of the aerodynamic parameters of flow Mach number, turbulence intensity, and turbulence length scale is investigated. The sound intensity is proportional to $\overline{u^2}$, while the turbulence length scale characterises the size of the largest eddies and therefore the frequency distribution of the turbulent velocity, and hence sound power spectrum.

6.2.1. Variation of Broadband Sound Power with Mean Flow Mach Number

We now investigate the broadband noise generated by the nominal cascade for the range of flow speeds with the values:

- Mach number M 0:0.1:0.7

The critical frequency varies with Mach number according to Eq (5.2-1) as shown in Table 10 below

M	f_c (Hz)	M	f_c (Hz)
0	2029.23	0.4	1497.74
0.1	1920.14	0.5	1321.81
0.2	1795.63	0.6	1125.00
0.3	1655.16	0.7	903.61

Table 10 – Variation of critical frequency with Mach number

Here a frequency range between 160Hz and 640 Hz below the critical frequency, and between 2560Hz and 8127.5Hz above the critical frequency is chosen for the analysis.

Figure 6.2.1-1 below shows the spectra of downstream sound power for flow Mach numbers *M=0.1:0.2:0.8.*

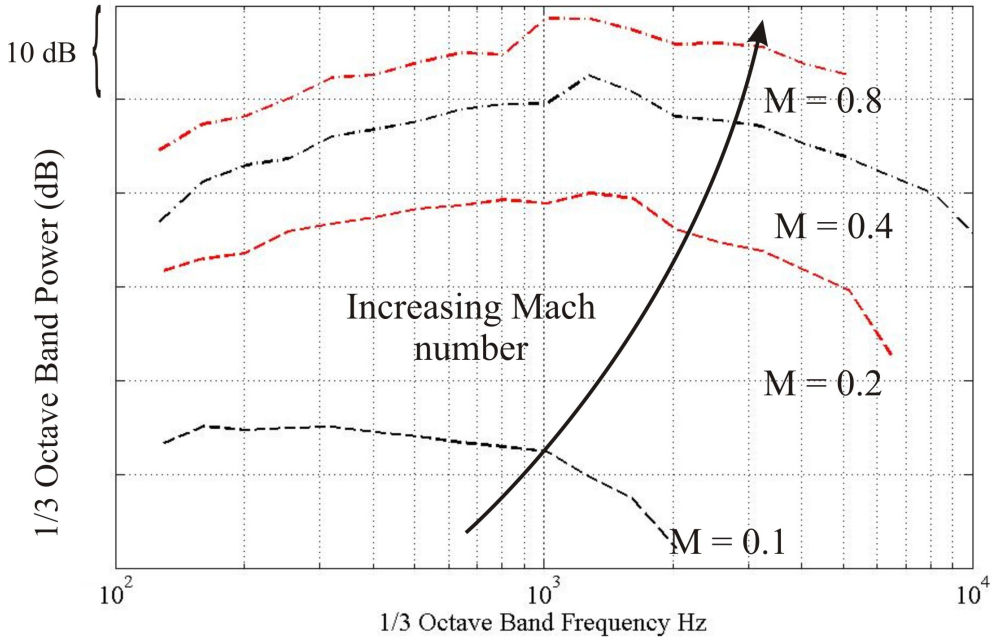

Figure 6.2.1-1 – Effect of increasing Mach number on downstream propagated sound power

As is well documented, fan broadband noise is highly sensitive to Mach number, found to vary with between the 5th and 6th power. Hanson [26] has predicted the variation of downstream sound power varying with a scaling law of approximately M^5, while Ganz et al [16] have measured variation in overall sound power with a scaling law of M^6.

Separating the sound power spectra plotted in Figure 6.2.1-1 into low and high frequency bands allows this frequency dependency to be investigated in greater detail. Figure 6.2.1-2a and b shows the variation of the sound power with Mach number M, integrated over the low and high frequency band ranges specified earlier.

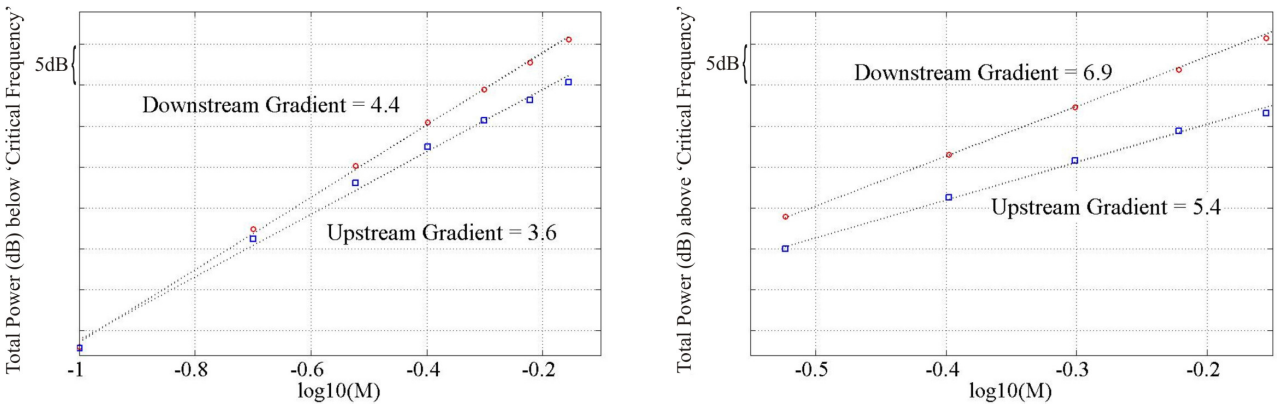

a – Sound power below f_c

b – Sound power above f_c

Figure 6.2.1-2 - Variation of average sound power with Mach number M

Below the critical frequency the downstream sound power increases with M more rapidly than the upstream. Both upstream and downstream sound powers are very similar in the low Mach number limit. Above f_c the rate of increase of downstream sound power with M is faster than the upstream sound power, though both increase more rapidly that their low frequency counterparts. Note that the sound power in the low frequency band increases more slowly than the M^5 scaling law, while the sound power in the high frequency band increases more rapidly than M^5. This suggests that differences in spectral behaviour at high and low frequencies must be considered separately, as opposed to specifying a single scaling law for the entire spectrum.

This finding was also reported by, for example, Glegg and Jochault [19] and Atassi and Logue [8], who also report that the noise variation due to Mach number is strongly dependent on frequency, being much larger at high frequencies.

6.2.2. Variation of Broadband Sound Power with Turbulence Intensity

The effect of increasing turbulence intensity on predicted broadband sound power is now investigated. The cascade investigated for the variation in turbulence intensity is as the nominal cascade with the following parameter variation:

- Turbulence intensity $\overline{w^2}/W^2$ $(2.5:2.5:1000)x10^{-5}$

The turbulence intensity $\sqrt{\overline{w^2}/W^2}$ therefore varies from 0.5% to 10% in steps of 0.5%. The critical frequency remains constant at 1322Hz for varying turbulence intensity. The frequency bands chosen are therefore between 160Hz and 806Hz for the low frequency band, and between 2032Hz and 8128Hz for the upper frequency band. As expected the broadband sound power increases linearly with increasing turbulence intensity, proportional to $\overline{w^2}/W^2$. This sound power scaling law is found for both upstream and downstream propagating sound powers, in both low and high frequency bands. Figure 6.2.2-1a below displays the variation in downstream propagating sound power spectra, and Figure 6.2.2-1b displays the variation in low frequency sound power, both with increasing turbulence intensity. Variation is the same for upstream sound power spectra, and high frequency sound power; these are therefore not shown.

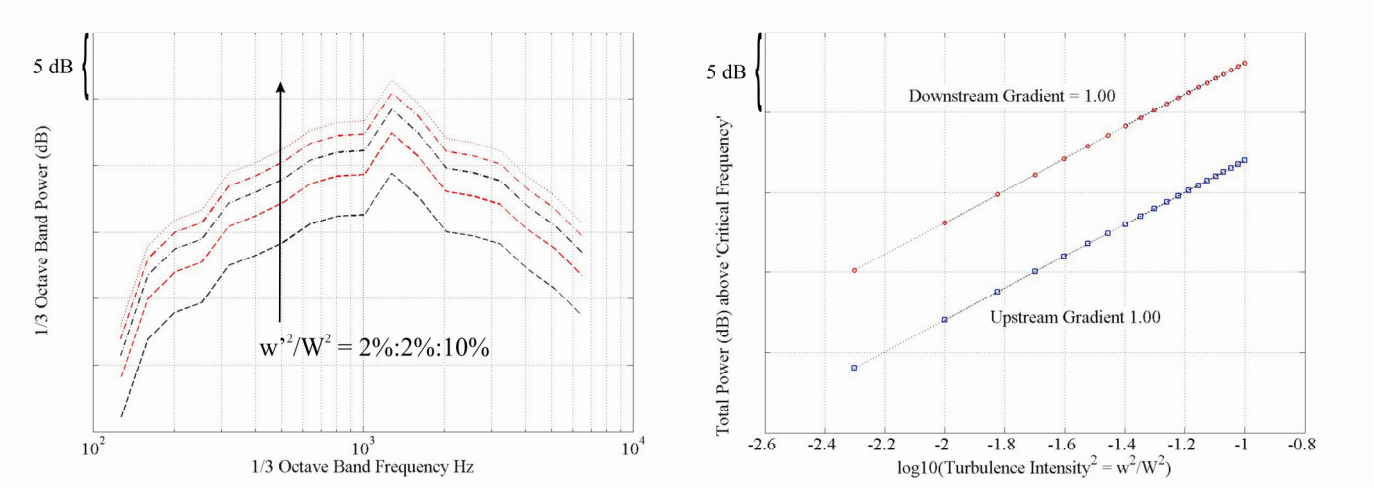

a – Downstream propagating sound power **b – Sound power below f_c**

Figure 6.2.2-1 - Variation of sound power with Turbulence Intensity

6.2.3. Variation of Broadband Sound Power with Turbulence Length Scale

The final aerodynamic parameter investigated is the turbulence length scale. This quantity quantifies the typical size of the largest turbulent eddy impinging on the blade. The cascade and flow parameters assumed in this investigation are the same as the nominal configuration but with the following variation in Λ:

- Turbulence length scale Λ / R $\qquad (5:5:75)x10^{-3}$

The critical frequency is again constant at 1322Hz. Frequency bands were chosen to be between 160Hz and 806Hz for the low frequency band and between 2032Hz and 8128Hz for the high frequency band. These frequency band limits were chosen to be consistently below and above the critical frequency, respectively.

Figure 6.2.3-1a and b below shows the effect of varying turbulence length scale on the sound power spectra:

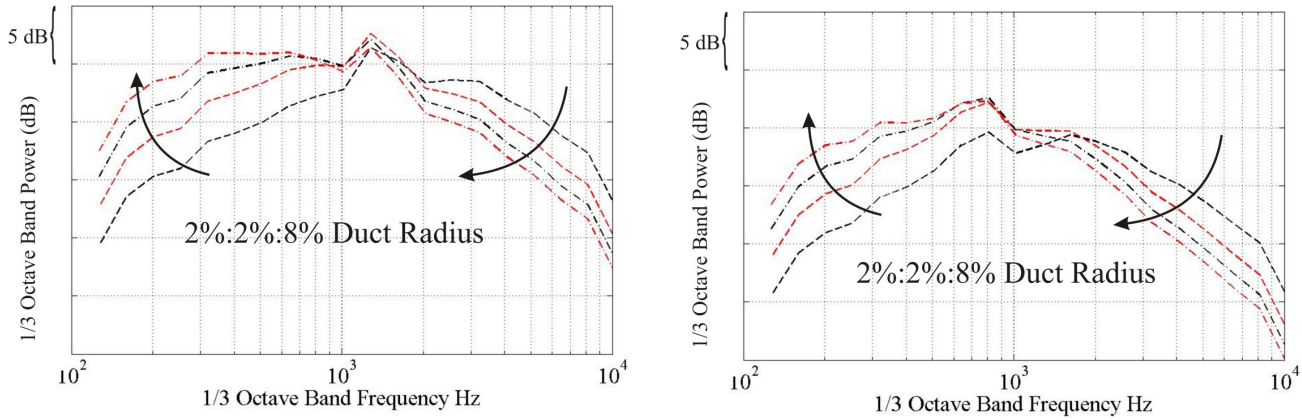

a – Downstream sound power **b – Upstream sound power**

Figure 6.2.3-1 - Variation of sound power spectral shape with turbulence length scale Λ

Increasing the turbulence length scale causes a 'rotation' of the power spectra, for both upstream and downstream sound power. As the turbulence length scale is increased the sound power increases at lower frequencies, and decreases at higher frequencies. This 'rotation' occurs around the frequency peak of the respective spectra. In the downstream sound power spectrum this is approximately equal to the critical frequency. This effect is likely to be fortuitous as the critical frequency is defined to be independent of length scale Eq (5.2-1). This rotation of the sound power spectra is also reported by Atassi and Logue [8], who find that the effect is stronger at higher Mach numbers.

Figure 6.2.3-2 shows the variation of the integrated sound power integrated over the low frequency band. The sound power is proportional to the turbulence length scale Λ, for small Λ. However, as Λ is increased further, the sound power begins to plateau. This suggests there is a limiting turbulence length scale above which low frequency sound power does not increase.

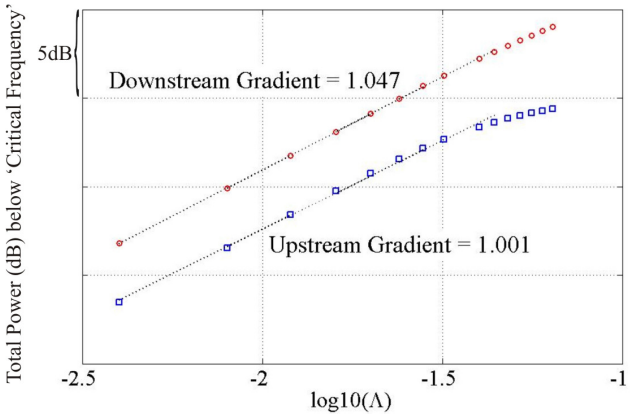

Figure 6.2.3-2 - Variation of average sound power with integral length scale, below f_c

The variation of sound power with length scale at high frequency can be compared directly with the analytic expression due to Cheong et al [11]. The integrated form of the high frequency analytic expression can be calculated by integrating the acoustic sound power per unit span above the critical frequency, to give the following equation:

$$P^{\pm} \approx F^{\pm}(M,\theta)\frac{B\rho_0\Lambda\overline{w}^2 W}{2\pi^2}\frac{M\left(1-M_1^{\,2}\right)}{\left(1-M^2\right)} \times\left[W^2\left(\frac{\ln\omega}{W^2}-\frac{\ln\left(W^2+\Lambda^2\omega^2\right)}{2W^2}-\frac{1}{W^2+\Lambda^2\omega^2}\right)\right]_{\omega_1}^{\omega_2} \qquad \text{Eq (6.2.3-1)}$$

This can be rearranged to

$$P^{\pm} \approx F^{\pm}(M,\theta)\frac{B\rho_0\Lambda\overline{w}^2 W}{2\pi^2}\frac{M\left(1-M_1^{\,2}\right)}{\left(1-M^2\right)}\left[\left(\ln\omega-\frac{1}{2}\ln\left(W^2+\Lambda^2\omega^2\right)-\frac{1}{1+\left(\Lambda\omega/W\right)^2}\right)\right]_{\omega_1}^{\omega_2} \qquad \text{Eq (6.2.3-2)}$$

where $(\Lambda\omega/W)$ is a Strouhal number, a non-dimensional number describing oscillating flow mechanisms. Figure 6.2.3-3 shows the variation of the integrated sound power in the high frequency bands, compared against the analytic expression due to Cheong et al [11] integrated over the high frequency bandwidth (Eq (6.2.3-2)).

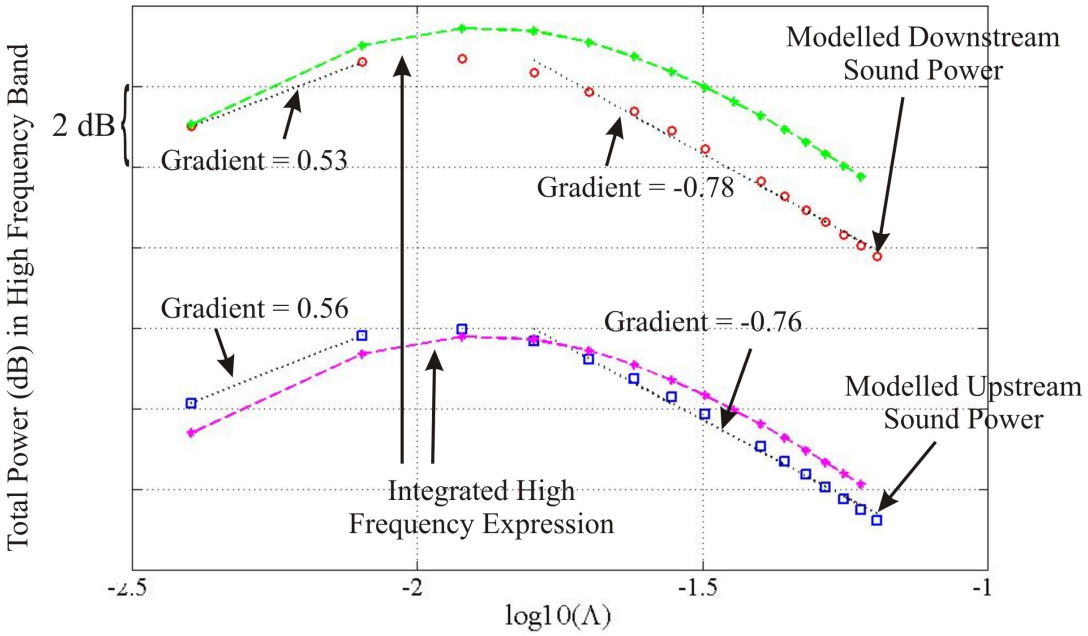

Figure 6.2.3-3 - Variation of average sound power with integral length scale, above f_c

In the high frequency bandwidth the sound power increases for small Λ initially, and then peaks for approximately $\Lambda = 0.012$. The power then decreases at a constant rate approximately proportional to $\Lambda^{-0.8}$. The sound power spectra calculated from the integrated equation of Eq (6.2.3-1) provides a reasonable approximation to the variation in sound power in the high frequency band, particularly for the upstream propagating sound power. The differences seen between the cascade model and integrated sound power spectra may be due to inaccuracies in the function $F^{\pm}(M,\theta)$ which was derived by a polynomial curve fit through predicted data. The length scale that maximises the sound power at high frequency is obtained from the minimum value of Eq (6.2.3-2).

The length-scale variation for low and high frequency limits can be investigated further by further rearranging terms of Eq (6.2.3-1 unrelated to turbulence length scale and frequency:

$$P = F^{\pm}(M,\theta)\frac{B\rho_0\overline{w}^2 W}{2\pi^2}\frac{M\left(1-M_1^{\,2}\right)}{\left(1-M^2\right)} \times \Lambda\left[\left(\ln\omega - \frac{1}{2}\ln W^2 - \frac{1}{2}\ln\left(1+\left(\Lambda\omega/W\right)^2\right) - \frac{1}{1+\left(\Lambda\omega/W\right)^2}\right)\right]_{\omega_1}^{\omega_2} \qquad \text{Eq (6.2.3-3)}$$

which reduces to:

$$= \Lambda\left(\ln\frac{\omega_2}{\omega_1} - \frac{1}{2}\ln\frac{1+St_{\Lambda,2}^{\,2}}{1+St_{\Lambda,1}^{\,2}} - \left[\frac{1}{1+St_{\Lambda,2}^{\,2}} - \frac{1}{1+St_{\Lambda,1}^{\,2}}\right]\right) \qquad \text{Eq (6.2.3-4)}$$

where $St_{\Lambda,1} = \omega_1 \Lambda / W$ and $St_{\Lambda,2} = \omega_2 \Lambda / W$, are the Strouhal number associated with the lower and upper frequencies.

At low frequencies $St_{\Lambda,1,2} \to 0$, and

$$P \propto \Lambda \ln \frac{\omega_2}{\omega_1} \qquad \text{Eq (6.2.3-5)}$$

Therefore

$$P \to \Lambda \text{ as } \Lambda \to 0 \qquad \text{Eq (6.2.3-6)}$$

At high frequencies where $St_{\Lambda,1,2} >> 1$, Eq (6.2.3-4) can be reduced to

$$P \propto \frac{3W^2}{2\Lambda}\left[\frac{1}{\omega_1^{\,2}} - \frac{1}{\omega_2^{\,2}}\right] \qquad \text{Eq (6.2.3-7)}$$

Therefore

$$P \to \Lambda^{-1} \text{ as } \Lambda \to \infty \qquad \text{Eq (6.2.3-8)}$$

These slopes of Λ^{+1} and Λ^{-1} for the high and low frequency limits are not reached in Figure 6.2.3-3, as the length scale magnitudes investigated do not sufficiently approach these low and high frequency limits.

6.3. Sound Power Scaling Equation

In this section the parametric results obtained in Sections 6.1 and 6.2 are used to deduce regression power law equations of the form:

$$PWL^{\pm} = \alpha^{\pm} 10 \log_{10}(\beta) \qquad \text{Eq (6.3-1)}$$

where α is the power law component for the parameter under consideration and β is the parameter under investigation. The change in sound power for a change in a particular parameter can therefore be calculated from:

$$\delta PWL^{\pm}(\beta)_i = \alpha^{\pm} 10 \log_{10}\left(\beta_1 / \beta_2\right)_i \qquad \text{Eq (6.3-2)}$$

where β_1 is the predictor parameter at the original performance point, and β_2 is the predictor parameter at the desired performance point. The power laws observed in the figures presented in Sections 6.1 and 6.2, for Mach number, turbulence intensity, turbulence length scale, number of vanes, and vane chord length are displayed in Table 11. Low frequency is defined as below the critical

frequency, and high frequency is defined as above the critical frequency. Note that the scaling law for the number of vanes is at constant chord.

Prediction Parameter	Low Frequency α		High Frequency α	
β	Upstream -	Downstream +	Upstream -	Downstream +
Mach Number	3.630	4.360	5.750	6.940
Turbulence Intensity	2.000	2.000	2.000	2.000
Turbulence Length Scale	1.001	1.047	$0.560 \rightarrow -0.764$	$0.532 \rightarrow -0.780$
Number of Vanes	-0.450	-0.200	1.020	0.740
Vane Chord length	0.000	-0.001	0.052	0.000

Table 11 - Summary of predictor gradients from first parametric study

The scaling powers summarised in Table 11 allow an increased understanding of the broadband noise generated by the cascade model. These are summarised below:

- The low and high frequency sound powers vary with scaling power laws on either side of the classic M^5 scaling. This implies that changes in low and high frequency sound power spectra must be considered separately, as opposed to specifying a single scaling law for the entire spectrum. Low frequency sound power varies approximately with Mach number to the 4th power which is smaller than the 6th power law measured by Ganz et al [16]. However high frequency sound power does vary approximately with the 6th power law measured by Ganz for fan broadband noise. The results of this investigation highlight the differing behaviour of acoustic power spectra at low and high frequencies.

- The lack of sensitivity of the acoustic power to vane chord length suggests that the rotor stator interaction noise generated by the cascade is localised towards the vane blade leading edges.

- The variation in sound power with turbulent length scale exhibits the most complicated behaviour. At low frequencies where the circumferential acoustic wavelength is larger than the vane spacing sound power increases proportionally to length scale. At higher frequencies a 'worst' case length scale is identified. This high frequency behaviour is predicted reasonably well by the analytic approximation of Eq (6.2.3-1

- The lack of a scaling power law for stagger angle shows that the influence of this parameter is highly complex.

After their investigation, Ganz et al [16] pose three questions concerning the effect of stator vanes on fan broadband noise. These were presented previously in Section 3.3. From the results of this parametric study little sensitivity in sound power is found to both solidity and chord. From the work of Cheong et al [11], the peak in the downstream propagating sound power spectra is found to correspond to the critical frequency, which is the frequency at which the acoustic mode number is equal to the number of vanes. These, and other effects, are predicted successfully by the cascade broadband noise model and allowed the derivation of the scaling power laws listed previously.

These power-laws derived in the first parametric study allow predictions of the change in broadband noise due to variations in the aerodynamic and geometric parameters. They are now used in the next chapter to predict the change in broadband noise due to changes in fan design parameters.

Chapter 7
Variation of Broadband noise with fan stage design parameters

7. Variation of Broadband noise with fan stage design parameters

The first parameter study of rotor-stator broadband noise described in Chapter 6 concentrated on the effects of basic geometric and aerodynamic variation on broadband noise. Chapter 7 now describes the results and procedure of a second parameter study of the cascade broadband noise model that incorporates variations in aerodynamic design parameters. These aerodynamic parameters are shaft speed, pressure ratio, and efficiency, which are varied while maintaining thrust. These variations are performed at three performance points; cruise, cut-back and approach. The results included in this thesis present the effect of varying fan pressure ratio on broadband noise. Section 7.4.1 of Appendix X displays a comparison between narrowband spectra predicted by the noise model and those measured on a fan rig test. Also shown in Section 7.4.2 of Appendix X are the effects of varying shaft speed and efficiency on broadband noise.

Division of the spectra into low and high frequency regions, as in the first parametric study, is again undertaken to allow the behaviour of the predicted sound power to be investigated with variations in design parameters. Lastly this chapter will investigate use of the correlations derived as part of the first parametric study to predict changes in broadband noise by considering the effects of changes in the base wake flow parameters Mach number, turbulence intensity, and turbulence length scale.

7.1. Preparation of common input conditions to throughflow prediction of rotor performance

The input parameters, listed previously in Chapter 6, to the noise model are calculated using a throughflow CFD solver. This is an axi-symmetric flow prediction program, where predictions are restricted to radial variations in flow parameters through the engine. The spanwise variation in the variables is calculated using non-uniformly distributed streamlines. Note that the throughflow program cannot compute fan stage performance as the program only tracks streamlines.

The main rotor-wake correlating parameter of pressure loss coefficient is calculated by the through-flow program and converted to wake momentum thickness, using the procedure described in Appendix E-1. The rotor wake momentum thickness, in addition to the distance travelled by the wake from the rotor trailing edge to the stator leading edge, form the inputs to the rotor turbulent wake correlations proposed by Gliebe et al [21]. These correlations are used to calculate the wake circumferential turbulence intensity and length scale that are the turbulence inputs to the broadband noise model.

The method of computing the flow variables for each parameter variation is described in the next section.

7.2. Theory of working line modifications and prediction of flow parameters for broadband noise parameter study – Engine 3

This section describes the modifications to the throughflow model input and output parameters necessary to deduce the flow variables for variations in:

- Fan design speed
- Fan design pressure ratio
- Fan efficiency

whilst maintaining constant thrust at the three flight conditions:

- Cruise
- Cut-Back
- Approach

The first of these parameters investigated is the fan design speed. The procedure by which fan speed is modified while maintaining constant thrust is now described.

7.2.1. Fan Design Speed

The fan design speed is the speed required to attain a specified performance position, for a fan subject to perfect running conditions. In reality the fan speed to attain a performance position may vary slightly. This section describes the procedure used to compute the fan stage parameters including blade whirl angles and pressure loss coefficient, for variations in shaft speed while maintaining thrust. Note that all other parameters are kept constant in this variation.

Figure 7.2.1-1 displays the cruise, cut-back and approach performance positions on a schematic of the cruise and sea level static working lines.

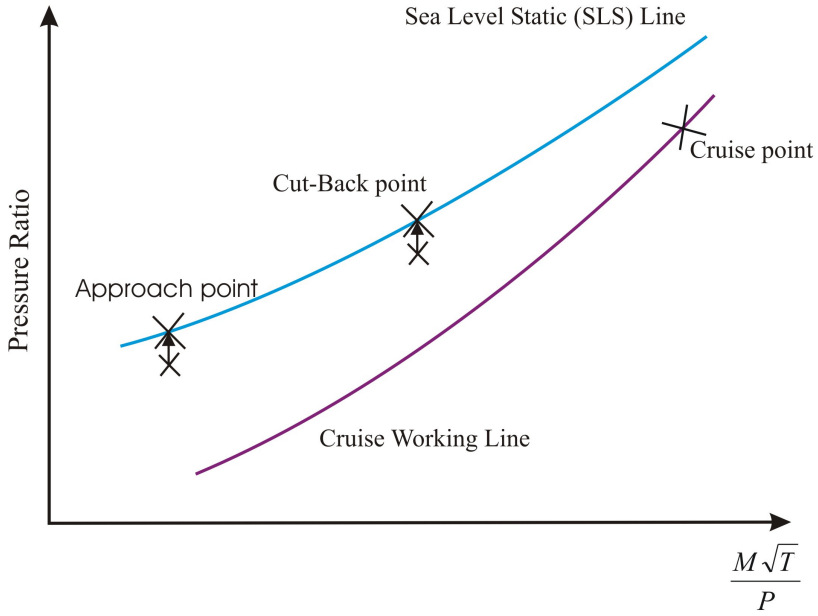

Figure 7.2.1-1 – Working line modifications with variation of design speed

During this first investigation, when fan speed is varied other fan parameters such as pressure ratio are maintained constant. In order to preserve thrust with pressure ratio, while varying fan speed, it is also necessary to maintain the same fan diameter (i.e. have the same size of engine). In order to meet these restrictions and also maintain the separation behaviour of flow over the fan blades, it is necessary to treat each performance point as a different fan design with different blade geometries. Similar separation characteristics would not be achieved by simply running the same fan geometry at a different shaft speed.

In order to maintain thrust the fan stage must produce the same work. This is achieved by modifying the angles in the velocity triangles according to the Euler work equation (Eq (0-20) in Appendix D-3).

It is assumed that fan losses do not change between performance points. The total range of shaft speeds under consideration for all three performance points is:

- Nominal case - 10%
- Nominal case - 5%
- Nominal case
- Nominal case + 5%
- Nominal case + 10%

A number of important angles relating to the flow and rotor blade are shown in Figure 7.2.1-2. Here γ_1 is the angle of incoming flow and η_1 is the blade leading edge metal angle. Therefore the angle of incidence of the blade is $i = \gamma_1 - \eta_1$. The angle γ_2 gives the flow exit angle, while η_2 denotes the blade trailing edge metal angle. The flow does not exit perfectly from the blade trailing edge and so the flow angle deviation is given by $\delta = \gamma_2 - \eta_2$. Note that changes in η_2 are incorporated at the different shaft speeds. If the flow deviation δ from the trailing edge is assumed to remain fixed, the changes in relative whirl angle between these cases are assumed to correspond to variations in the blade trailing edge 'metal angle' η_2 in order to produce this thrust at the modified shaft speed.

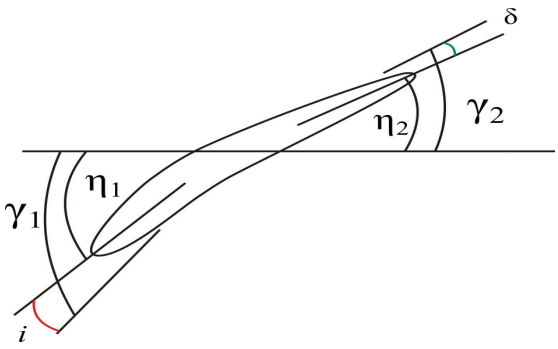

Figure 7.2.1-2. Angles used in the description of flow about a rotor

A similar procedure is then followed for the cut-back case. The cut-back position for nominal shaft speed is first performed. The same changes in metal angle identified above, for the variation in cruise point shaft speed, are applied to produce the additional cut-back shaft performance points. These changes in metal angle, when combined with the modified cut-back shaft speeds, predict a pressure ratio that corresponds to a performance point slightly below the desired cut-back point on the sea level static line. This is shown by the point marked *X* below the cut-back position in Figure 7.2.1-1. The shaft speed is therefore modified slightly to produce the same operating point as the nominal cut-back case. Here it is assumed that small changes in shaft speed do not modify the rotor relative outlet angle.

As mentioned previously, in this investigation we seek to maintain the same flow separation characteristics over the 'redesigned blade'. This is equivalent to maintaining constant Diffusion Factor. The diffusion factor is defined to relate directly to the size of the adverse pressure gradient encountered by the boundary layer on the suction side of the cascade blade. The diffusion factor is therefore a direct measure of the likelihood of boundary layer separation, and sudden loss increases through the cascade. A two dimensional approximation of the diffusion factor is given by [34]

$$DF = 1 - \frac{V_2}{V_1} + \frac{\Delta V_\theta}{2\sigma V_1} \qquad \text{Eq (7.2.1-1)}$$

where V_1 and V_2 are average velocities entering and exiting the blade row, ΔV_θ is the change in whirl velocity, and σ is the solidity (c/s).

In order to maintain constant diffusion factor it is necessary to modify the final term in Equation 7.2.1-1. This is achieved by adjusting the rotor and OGV chords and hence σ. This provides a new

rotor – stator separation distance for input to the turbulence correlations (described in Table 16, Appendix C-3).

Maintaining separation characteristics over the rotor blade while changing the blade metal angles means that the wake angle leaving the rotor trailing edge varies accordingly. As mentioned in Chapter 5, a requirement of the cascade broadband noise model is that the rotor wake strikes the vane leading edges perfectly, with no angle of attack. It is therefore necessary to modify the stagger angle of the vane cascade to match the changes in rotor wake angle. The effect of this limitation on the resulting broadband noise predictions is discussed further in Section 7.4.2, of Appendix X.

This operation was also repeated for all shaft speeds at the approach condition. The tabulated results of this procedure can be seen in Section 7.2.1 of Appendix X.

7.2.2. Fan Design Pressure Ratio

This section describes the procedure used to calculate the fan performance parameters for variations in fan pressure ratio while maintaining constant thrust, and constant shaft speed and efficiency. The five different pressure ratios calculated at cruise, cut-back and approach are:

- Nominal – 0.05
- Nominal – 0.02
- Nominal
- Nominal + 0.02
- Nominal + 0.05

Figure 7.2.2-1 shows a working line schematic which graphically indicates the procedure used to vary the fan performance characteristics during in the pressure ratio investigation of broadband noise. The procedure is described below.

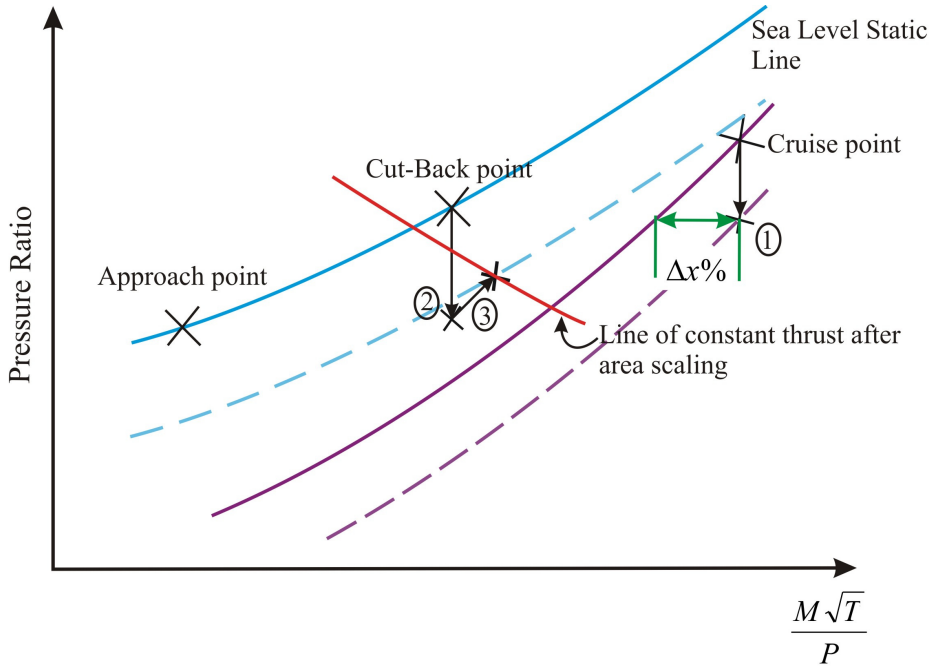

Figure 7.2.2-1 – Working line modifications with variation of design pressure ratio, not to scale

For the initial case, consider the variation of pressure ratio at the cruise point. A throughflow performance model was run for the nominal cruise point and the thrust calculated from the product of the bypass mass flow and jet velocity. The throughflow code was then used to calculate the aerodynamic parameters for the cruise point at the different pressure ratios listed previously.

This procedure is now illustrated by example. Consider for example a point on the working line diagram of reduced pressure ratio with the same cruise mass flow, point (1) in Figure 7.2.2-1, with a pressure ratio of, for example, the nominal pressure ratio – 0.02. The thrust is calculated at this point. In order to maintain the same thrust while modifying the pressure ratio it is necessary to scale the fan area. The scaling of fan area required to provide the nominal cruise thrust for the new pressure ratio can be calculated from the ratio of the nominal and new thrust values.

Again, the whirl air angles are extracted at this performance point. As for the shaft speed variation, assuming that the flow deviation through the fan remains fixed then the changes in these whirl air angles give the corresponding changes in rotor blade metal angles.

The difference in mass flow function $M\sqrt{T}/P$ between point 1 and the cruise working line is then determined as a fraction of the mass flow (marked $\Delta x\%$ on Figure 7.2.2-1). This ratio is assumed to be constant for the corresponding cut-back and approach cases.

In summary, the information obtained for each pressure ratio variation at cruise is:

- Change in flow whirl angle between the nominal cruise performance point and each alternative pressure ratio point. This is used to give equivalent metal angle changes at cut-back and approach.

- Area ratio required to maintain constant thrust at each alternative pressure ratio point. This provides new target thrusts for each pressure ratio variation at cut-back and approach.

- Difference in mass flow function as a fraction of mass flow. This is used to locate the working line of each alternative pressure ratio point.

Now consider the variation of pressure ratio at cutback. First, fan performance and behaviour is calculated for the nominal cutback position. For variations of pressure ratio, while maintaining thrust at the cut-back position, consider as an example a performance point on a lower pressure ratio working line. This target is a point with the same thrust as the original cut-back point, after area scaling. Point (3) on Figure 7.2.2-1 is this desired final point lying on the line of constant thrust. Continuing the cruise example, assume this is the nominal cutback pressure ratio – 0.02.

The same mass flow fraction $\Delta x\%$ calculated for point (1) is added (in this case) to the cut-back mass flow position on the Sea Level Static (SLS) working line. This defines the new working line (dashed blue line in Figure 7.2.2-1). The target performance position at cut-back is then initially calculated with the same fan speed and flow, using the modified metal angles derived for point (1) from the cruise case. This procedure generates performance points that do not lie exactly on the modified line of constant thrust (dashed blue line). For example a reduction in pressure ratio produces point (2), a point below the line.

Reductions in pressure ratio at the same thrust are therefore achieved in summary by modifying the shaft speed, mass flow, and pressure ratio. To compute the new point we initially assume that the mass flow rate is the same as that of the original nominal cut-back case. An initial pressure ratio estimate of point (3) is also calculated using an approximate fit to the cutback working line. The final mass flow rate and rotor pressure ratio are then calculated using an iterative procedure to compute a final solution that provides the target thrust of (3). Once the thrust solution has converged the mass flow rate of point (3) is extracted. The final cut-back performance result is then computed for this flow using the same metal angle changes from cruise. Again the final result is slightly below the target point, requiring a small change in shaft speed to meet the target pressure ratio exactly. This small change in shaft speed does not have a large impact on the accuracy of the final performance point.

This procedure is then repeated for the additional cut-back points and approach cases. Tabulated results for the pressure ratio procedure can be seen in Section 7.2.2 of Appendix X.

7.2.3. Fan Efficiency

Changing the rotor efficiency at constant thrust will change the rotor loss by modifying the outlet pressure, while keeping the swirl velocity and angles constant. The pressure loss coefficient variation with radius can be altered incrementally in the throughflow code, which in turn varies efficiency. Tabulated results for the efficiency procedure can be seen in Section 7.2.3 of Appendix X.

7.2.4. Schematic of fan working lines with variation of fan performance variables marked

Figure 7.2.4-1 displays a schematic of the fan working lines with normalized pressure ratio and mass flow axes. The performance positions generated by the procedures used for the different parameter variations are marked by '□', '○' and '◊'. Variation of shaft speed or efficiency, while maintaining thrust should generate points which lie on the default pressure ratio and mass flow position at cruise, cutback, and approach. A small variation is seen in the location of the efficiency cases marked at cutback. The variation of pressure ratio should generate a vertical line of points at each flight condition, corresponding to a variation in pressure ratio with constant mass flow. Again a small amount of deviation in the pressure ratio positions from the vertical is seen at cutback and approach, although it is unlikely to have a large influence on the accuracy of the results.

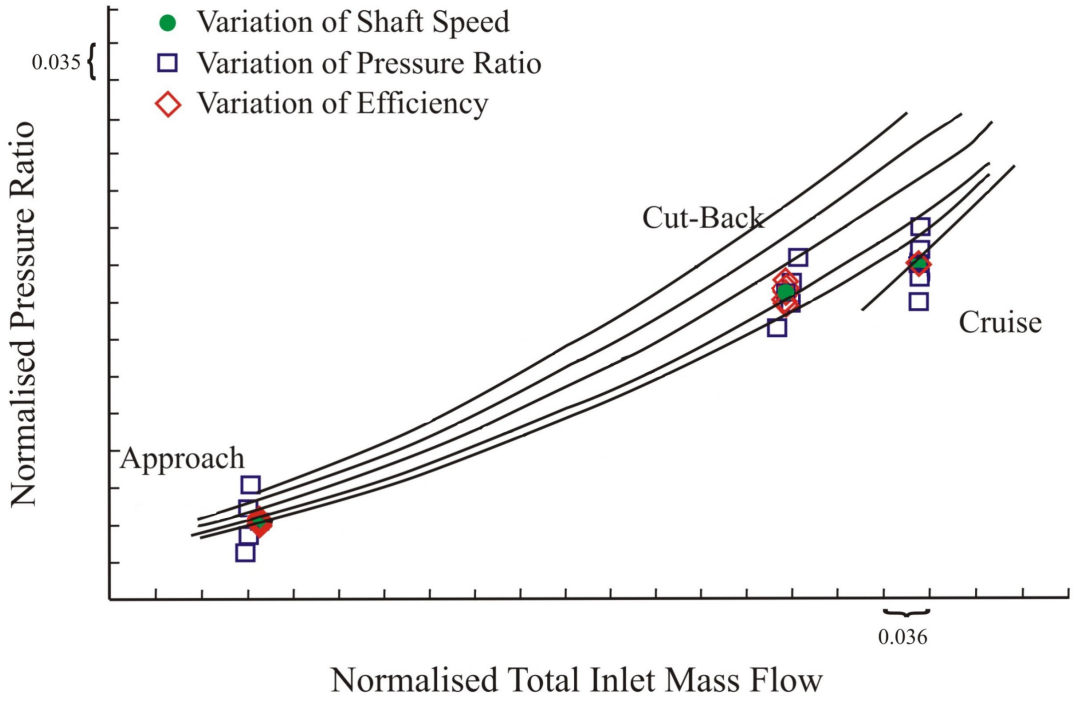

Figure 7.2.4-1 - Schematic of fan working lines with parameter study cases overlaid, note that x-axis is in Imperial units

The investigation described thus far concentrates on the Engine 3 fan, which has considered parameter variations at constant thrust around three fan performance points of cruise, cutback, and approach. In addition the modelled broadband noise of the Engine 2 fan is also considered, to provide an additional results set to validate the noise spectra predicted by the broadband noise model.

The results shown below are those of the Engine 3 fan, with variations in broadband noise predicted for changes in pressure ratio. Results for Engine 3 broadband noise variation with shaft speed and fan efficiency, and Engine 2 validation results can be seen in Section 7.3, Appendix X.

7.3. Results of investigation into the effects on broadband noise of varying fan design parameter

This section presents the results of an investigation into the effect on broadband noise of varying pressure ratio on Engine 3, while maintaining thrust. The scaling power laws from the first parametric study are then used to predict the change in broadband noise between different performance points of both fans and compared with the exact prediction.

7.3.1. Variation of low and high frequency sound power with fan performance variable

This section considers the effect of varying pressure ratio on broadband noise. The study is based around the Engine 3 fan. As seen in Chapter 6, the predicted sound power spectra are split into high and low frequency bands above and below the critical frequency. The variation of sound power in these low and high frequency bands due to variations in the engine design parameter are predicted. For all cases the low frequency band includes frequencies between *285Hz* and *1436Hz*. The high frequency band includes frequencies between *5747Hz* and *9122Hz*.

Cruise, cut-back and approach results are derived for all low frequency bands below the critical frequency. The flow Mach number onto the OGVs is insufficient in the approach case to produce a predicted spectrum which extends above the critical frequency (c.f. with Figure 6.2.1-1). Therefore, only cruise and cut-back results are displayed for the variation in the high frequency band.

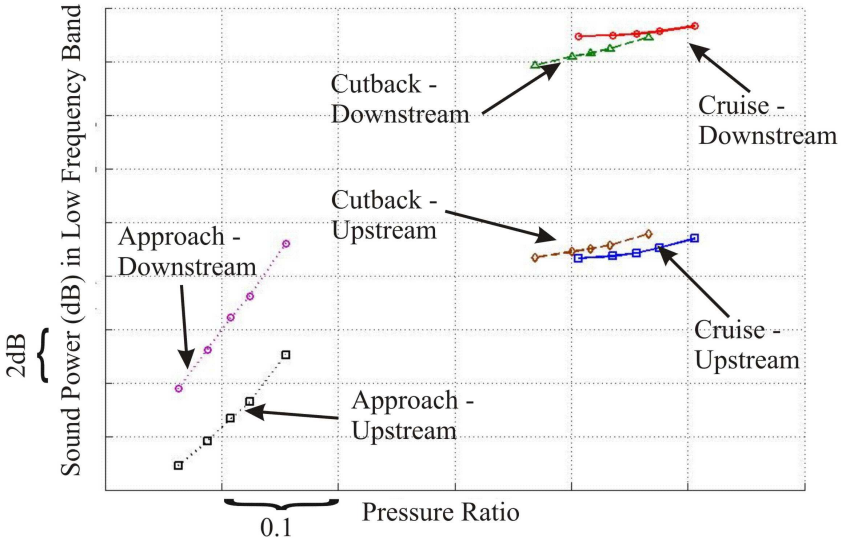

a – Below the critical frequency

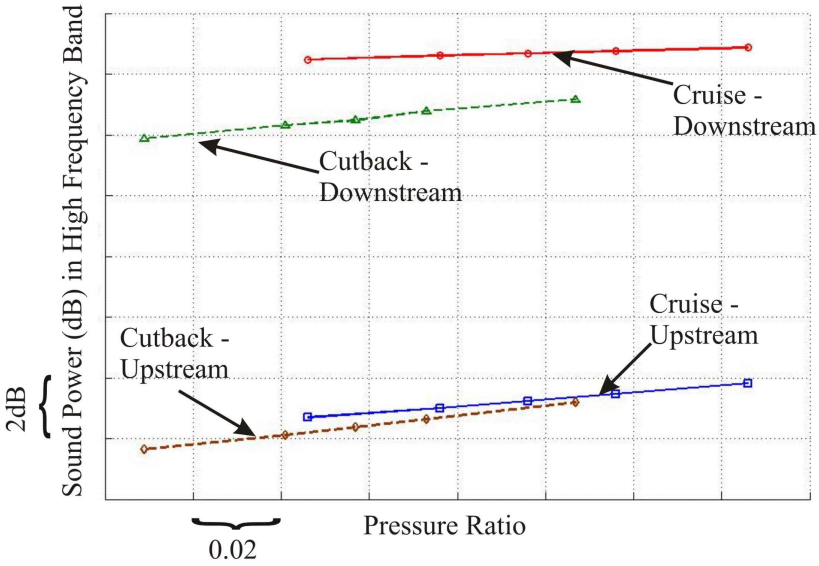

b – Above the critical frequency

Figure 7.3.1-1 Variation of sound power with fan pressure ratio

Figure 7.3.1-1a shows the variation of low frequency sound power with pressure ratio. It indicates that increasing fan pressure ratio while maintaining thrust and shaft speed increases broadband noise. The increase is greatest for the approach case, whereby there is a rise in noise level of approximately 4dB for an increase in pressure ratio of 0.1. Increasing pressure ratio at cut-back or cruise causes an increase of approximately 1dB in noise level for an increase in pressure ratio of 0.1. This behaviour is in agreement with the behaviour observed in the measurements of Ganz et al [16] who measured a

3dB increase in noise for a 10% increase in pressure ratio. Atassi and Vinogradov [9] also predicted that increasing the loading on a cascade of stator vanes increased the broadband noise generated.

The variation of high frequency sound power with pressure ratio can be seen in Figure 7.3.1-1b. Again this figure suggests that increasing the pressure ratio causes an increase in sound power. In order to further understand this behaviour it is necessary to consider variations in individual rotor wake parameters, such as turbulent length scale and turbulence intensity. These changes in wake parameters are the cause of the change in broadband noise due to changes in pressure ratio, and provide further insight into which wake parameters are the major noise generators. A full breakdown of the wake parameters for this can at cutback can be seen in Section 7.4.2.4 of Appendix X, only the variation of flow Mach number onto the OGVs due to changes in fan pressure ratio is shown here in Figure 7.3.1-2.

Figure 7.3.1-2 shows that the Mach number of the wake striking the OGVs reduces as pressure ratio reduces. This may explain the reduction in sound power with pressure ratio, though whether Mach number is the dominant sound power control mechanism is investigated in the following section.

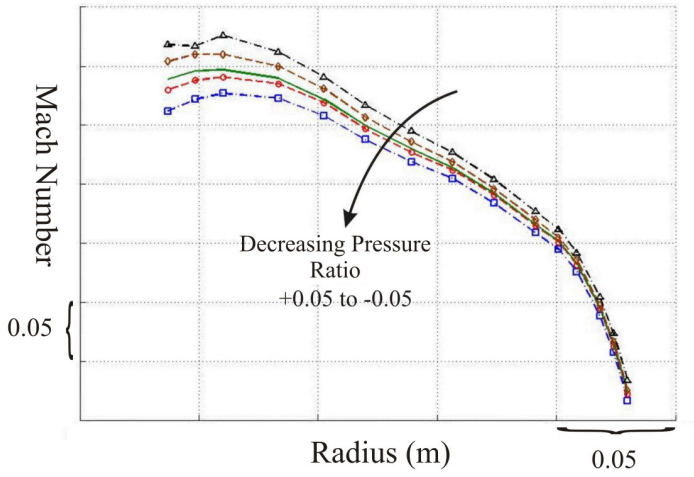

Figure 7.3.1-2 Variation of Mach number with pressure ratio at cut-back

The following section uses the scaling power laws shown in Table 11, and changes in turbulence intensity, turbulence length scale and Mach number, to predict the change in broadband noise between two performance points.

7.3.2. Prediction using power laws of first parametric study

The correlation power laws listed in Table 11 can be used to predict the variation in broadband noise, provided changes in flow parameters are known. If the broadband noise spectrum at an initial performance point is known, the broadband spectrum at a second point can be estimated according to Eq (7.3.2-1) below. This would allow a first estimate of the broadband noise for a new fan design without requiring the noise model to be run.

$$PWL(\Pi_2) = 10\log_{10}\left[\frac{\sum_i w_{ref}\, 10^{\delta PWL_i/10}}{\sum_i w_{ref}}\right] \qquad \text{Eq (7.3.2-1)}$$

The summation over *i* denotes summation over the number of radial strips. The sound power deltas for each strip due to changes in a particular parameter can be calculated using Eq (6.3-2).

Several results cases are chosen to represent the changes most likely required by an industrial fan design change.

- a - Engine 3 fan at cutback, from nominal pressure ratio - 0.05, to nominal pressure ratio + 0.05
- b - Engine 3 fan between cutback and cruise flight positions
- c - Engine 2 fan on an individual working line between 65% and 95% maximum shaft speed
- d - Engine 2 fan between working line 5, 70% maximum shaft speed, and working line 3, 95% maximum shaft speed

Figure 7.3.2-1 displays the predicted third octave sound power changes in rotor-stator interaction broadband noise for the first of the four flight cases (case a) defined above to illustrate the predictive capability of the scaling power laws. Cases b, c, and d can be seen in section 7.4 of Appendix X. The initial spectrum is the modelled spectrum for the initial flight case. This initial spectrum acts as the baseline to which the predicted change in noise is added in an attempt to accurately predict the target noise spectrum. The target noise spectrum is also modelled using the full noise model.

Individual predicted spectra are estimated using the scaling power laws presented in Section 6.3 for the flow predictors of Mach number, turbulence intensity, and turbulent length scale. A scaling power law could not be derived for changes in stagger angle. Individual predicted spectra trace the estimated 'target' spectra calculated using turbulence intensity, turbulent length scale, and Mach number. An additional spectrum is produced tracing the sum of the predicted changes due to these three flow predictors, as shown in Figure 7.3.2-1.

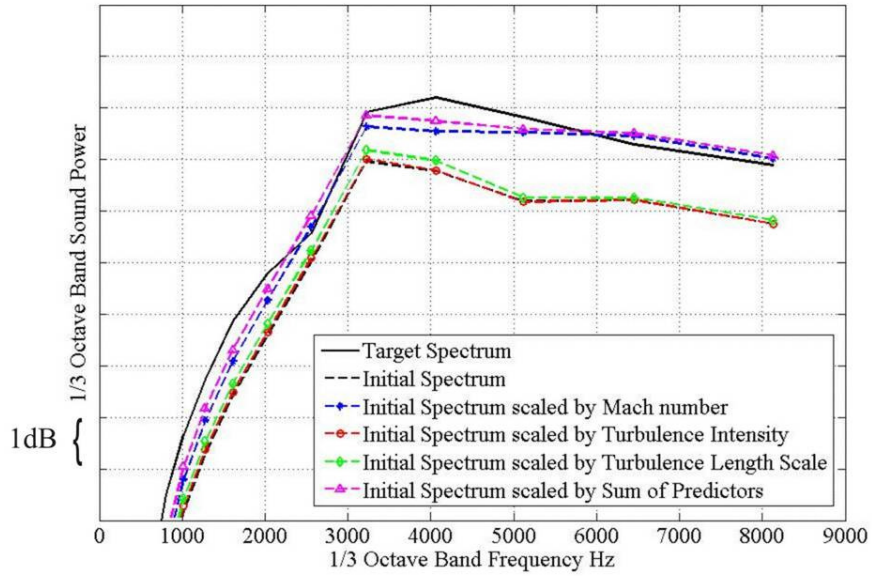

Figure 7.3.2-1 – Prediction of change in broadband noise between two flight performance positions

The change in sound power predicted by the turbulence intensity and length scale provides the smallest change to the sound power level of the initial spectrum. This is due to the relatively small changes in pressure loss coefficient between the initial and target predicted flight positions shown in Section 7.4.2.4 of Appendix X, and suggests that relying on this source for estimation of turbulence parameters does not take additional turbulence structures into account. For example, the Gliebe correlations use the same correlations whether for the hub, tip, or mid-span fan positions, including any flow structures present at these radial positions. The flow Mach number is the dominant flow predictor, particularly at higher frequencies above 5kHz (rig scale). This will be discussed further below.

Generally the most accurate predicted spectrum is that produced by summing the three flow predictors. This estimated spectrum is most accurate over the widest range of frequencies, including at lower frequencies. However, the sound power changes calculated using the scaling power laws are based on the spectral shape of the initial spectrum. Therefore the estimated spectra display the same spectral distribution as the initial spectrum.

The following section discusses these results, including the disparity between the estimated and calculated target spectra at lower frequencies.

7.4. Discussion on second broadband noise parametric study, and use of scaling power laws for sound power prediction

Results of the second parametric study show that the effect of varying fan pressure ratio, while maintaining thrust, is intuitive. As pressure ratio increases then sound power increases. Results for the variation in sound power due to changes in shaft speed, and fan efficiency, at a constant thrust, are shown in Appendix X.

In order to understand why sound power behaves in this way, individual flow and geometric parameters were analysed, with the majority of these analysis results shown in Section 7 of Appendix X. This analysis suggests that the flow Mach number onto the OGV cascade is the largest contributor to changes in the generated broadband noise, and increasing shaft speed while maintaining thrust reduces broadband noise by virtue of reducing the absolute Mach number onto the OGVs.

Using the sound power scaling laws derived during the first parametric study for the flow parameters also reinforce the suggestion that Mach number is the largest contributor. Estimation of the sound power changes using these flow scaling laws provides good accuracy at higher frequencies (above approximately 5kHz). However, these laws account for approximately one third of the calculated sound power change at lower frequencies below 5kHz. There are a number of possible explanations for this inaccuracy.

That the inaccuracy occurs at low to mid-frequencies suggests that some larger flow structures (in terms of characteristic length scale) are not taken into account in the model. This may be due to the throughflow code used to predict the fan behaviour for these flight positions. As a two-dimensional code then three-dimensional structures and separations cannot be modelled correctly and their impact will not be taken into account. This would have a larger effect on the Engine 2 fan modelled results, as seen in Appendix X. The larger changes to OGV stagger angle in the tip region are a consequence of larger changes in rotor tip turning and rotor wake whirl angles.

This problem with the capture of larger scale structures extends to the Gliebe correlations used to provide the turbulent input to the cascade model. These correlations are applied at all radial positions, whether in the clean flow of the rotor mid-span wake, or near the rotor tip where there may be large turbulent boundary layer eddies and boundary layer-tip vortex interaction. Application of the correlations in this region may require some empirical correction of turbulence intensity and length scale, both of which show little variation despite the fan performance changes of the different investigated flight positions.

Finally, the effect of changes in stagger angle was not taken into account correctly. The cascade model assumes the incoming flow strikes the OGV cascade leading edges perfectly, and is unable to consider any angle of attack. During the first parametric study a scaling power law for stagger angle could not be derived. This suggests that the stagger angle effect is not separable, and interacts with other parameters. Appendix X shows that the Engine 3 stagger angle changes by four degrees over the total range of shaft speeds considered. However, from (Figure 6.1.3-3) in Section 6.1.3 we can see that a change in stagger angle of four degrees can cause an increase in low frequency sound power of approximately 0.5dB, the inclusion of which could improve predictions.

Chapter 8
Variable Area Nozzle Study

8. Variable Area Nozzle study

In this chapter we investigate the noise reduction benefits of a variable area nozzle. A Variable Area Nozzle (VAN) is an exhaust nozzle whose diameter can be modified adaptively for different flight positions, thereby producing the most efficient overall engine design at the requisite performance point. In addition to noise control, possible benefits include reduced specific fuel consumption, increased thrust, and control of turbine entry temperature. Such nozzles currently exist on military aircraft with afterburner equipped engines to improve performance. The variable area nozzle allows a greater degree of exhaust jet expansion control. Typical afterburner control nozzles can be seen on the EJ200 engines of the Eurofighter Typhoon, shown below in Figure 8-1.

Figure 8-1 – Eurofighter EJ200 exhaust nozzles

This variable area nozzle is controlled by overlapping petals that contract and expand the nozzle area. While this method of area control is structurally strong, the weight penalty for a civil airliner is prohibitive. The use of variable area nozzles as applied to civil engine performance improvement could therefore benefit from novel control technologies such as shape memory alloys. This technology is currently attracting the attention of major aero-engine manufacturers and research institutes. Figure 8-2 displays the implementation of a variable area nozzle constructed of overlapping plates proposed by NASA. The nozzle area is adapted by use of shape memory alloys.

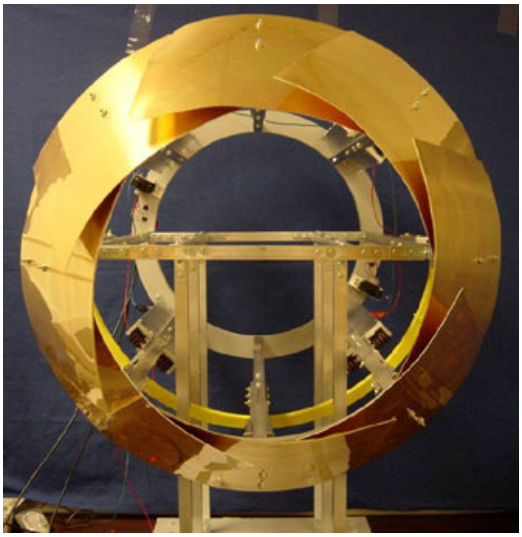

Figure 8-2 –Reduced area configuration of the variable area exhaust nozzle after the shape-memory-alloy wires are electrically heated [56]

In this chapter we investigate the effect of nozzle area variations on aircraft noise sources, including total aircraft and engine noise, jet and installation noise, fan forward and rearward noise, and turbine and core noise. Only bypass ('cold') nozzle area changes will be considered during this study. Core ('hot') nozzle changes are not considered. The noise changes in changing nozzle area are predicted using an in-house aircraft and engine noise prediction tool, hereafter referred to as the '*noise model*'.

Within this chapter the term '*delta*' is used to signify an absolute dB change in noise source level.

Noise source level predictions are presented in terms of Effective Perceived Noise Level (EPNL), in decibels calculated using the noise model. This is an internationally recognised unit for describing the noise of a single aircraft operation (e.g. approach) as experienced at one position on the ground. EPNL is a single number that includes tone corrections and duration effects, and is the standard unit for use in engine certification procedures.

The noise model consists of a number of empirically derived correlations and databases that predict engine and aircraft noise at various certification flight positions from a limited number of engine parameters. These have been derived using a combination of engine and rig scale test results. The noise model uses as input several noise correlating parameters, for example fan tip relative Mach number M_{Rel}, normalized turbine speed $\left(N/\sqrt{T}\right)_{Turbine}$, and mixed jet velocity[5] V_M.

As well as acting as a noise model correlating parameter, the fan tip relative Mach number M_{Rel} is also used in the prediction of the fan rig noise deltas, i.e. the change in noise level due to a change in nozzle exhaust area. The noise model 'correlates' fan noise sources such as broadband or buzz-saw

[5] Mixed jet velocity V_M is defined as the mean velocity on the axial centreline of the jet when both the hot and cold jet streams have completely mixed.

noise primarily on M_{Rel}, and therefore does not include the effects of changes between working lines. In order to include the effects of a change in working line (at a fixed M_{Rel}) it is necessary to introduce an additional correction that is derived from fan rig noise measurements. The method for predicting fan rig noise source changes to include this working line effect is described fully in Section 8.3.1 of Appendix X, only broad details are given in this main body of the thesis.

The aerodynamic performance calculations of the engines under investigation are performed using an in-house performance model, hereafter referred to as the '*performance model*'. This performance model is a 1-D steady state model that predicts thermodynamic, aerodynamic, and mechanical parameters of the gas turbine. This performance output also forms an input to the noise model. The model is used to predict the performance of an average production engine, and can be used for the development of engine tests and flight tests. The performance model is constructed using inputs provided for each of the turbo-machinery components (such as a compressor blade row or bypass exhaust nozzle), and each component can be modified independently. The prediction can be subjected to structural, aerodynamic, or performance constraints (e.g. thrust). This performance model provides such engine performance parameters as fan pressure ratio and mass flow which can then be directly input to the noise model.

Difficulties are anticipated when trying to use the noise model to accurately predict changes in fan noise sources. The noise model currently predicts the various fan noise sources based primarily on M_{Rel} as they are based on measured rig data obtained for fan speed changes along fixed working lines.

However, nozzle area variations whilst maintaining the same thrust result in shaft speed and pressure ratio changes. Working line modifications must therefore be included in the noise predictions. A new method, described in this chapter has been developed to allow the calculation of these changes in fan noise sources that incorporates these working line variations. The modified method, described in Section 8.3, separates fan noise changes into two components. One component is due to changes in M_{Rel}, which are predicted by the noise model, and the other is due to working line changes, which are extracted from Engine 2 rig measurements. The basis for this modelling approach is written symbolically below in Eq (8-1). For each source we assume that the effects of M_{Rel} and working line are additive, i.e.

$$\Delta SPL\left(M_{Rel}, WL\right) = \Delta 10n \log_{10}\left(M_{Rel}\right) + \Delta SPL\left(WL\right) \qquad \text{Eq (8-1)}$$

where $\Delta SPL\left(WL\right)$ denotes the change in Sound Pressure Level due to a change in working line, and 'n' is the power law of the correlation listed within the noise model that predicts the noise change due

to a change in M_{Rel}. Here we have assumed that the noise changes due to M_{Rel} and WL are additive and are therefore mutually independent. The validity of this assumption remains to be determined.

Both of these components (M_{rel} and working line effects) are important, particularly at higher fan speeds where the noise levels of the different fan noise sources can change rapidly, as shown in Chapter 4 of this public thesis document, and Chapter 4 of Appendix X. Although there is some cancelation, as shown later, it is important to incorporate both effects into the prediction.

8.1. Objectives and scope

This objectives and scope of this investigation are to:

- Provide an understanding of the effect of a change in nozzle area on fan noise in the forward and rearward arcs, jet and installation noise, and turbine and core noise.
- Provide an understanding of the noise sensitivity to engine cycle for three engine types

This study on the noise benefits of a variable area nozzle will be undertaken for the three engines:

- Engine 1
- Engine 3
- Engine 4

at:

- Approach
- Cutback
- Sideline
- Cumulative

Four engine nozzle areas will be modelled:

- Baseline – 5%
- Baseline
- Baseline + 5%
- Baseline + 10%

Three nozzle area changes are chosen in addition to the nominal area; nominal area - 5%, +5% and +10%. These nozzle area changes are chosen as representative of potential realistic changes, and include both a decrease and an increase in nozzle area. The following section will present the noise results of the variable area nozzle study.

8.2. Procedure for the derivation of engine noise changes due to nozzle exhaust area changes

The procedure for the calculation of the changes in noise due to changes in nozzle area, while keeping thrust constant, is divided into two parts. A prediction is first made of the engine performance. This provides the engine performance cycle information to the noise model, as well as the necessary fan variables for the extraction of the fan rig noise deltas. The modified aerodynamic parameters and fan noise deltas are then used to make the noise prediction.

The modelled engine performance cycle predicted for each change in nozzle area is assessed to ensure that the modified performance is realistic. Both the Engine 4 and Engine 3 engines remained within their operating limits for the specified nozzle area variations. However the Engine 1 engine approached 'red-line' limits[6] for increases in nozzle area at cutback and sideline, and had difficulty meeting the required thrust. This has a significant effect on the Engine 1 performance and noise results shown in the following sub-sections. Engine 1 noise results must therefore be treated with caution.

As mentioned above the noise model primarily correlates engine noise using the engine correlating parameters: M_{Rel}, $\left(N/\sqrt{T}\right)_{Turbine}$, and V_M. The variation of these parameters with nozzle area will now be considered individually.

8.2.1. Variation of fan tip relative Mach number M_{Rel} with nozzle area, constant thrust

Figure 8.2.1-1 shows the variation of M_{Rel} versus percentage nozzle area change for the three engines under investigation at the three certification points. As the nozzle area increases the static pressure downstream of the fan reduces. The pressure rise across the fan therefore decreases and the fan must rotate more rapidly in order to produce the same work, as predicted in Eq (0-20), Appendix D-3. Therefore the *fan tip relative Mach number increases with nozzle area, to maintain constant thrust.*

[6] A 'red-line' limit is an absolute limit of the engine under investigation. This may be a component structural limit of torsion or temperature, or the largest gross thrust that can be generated by the engine.

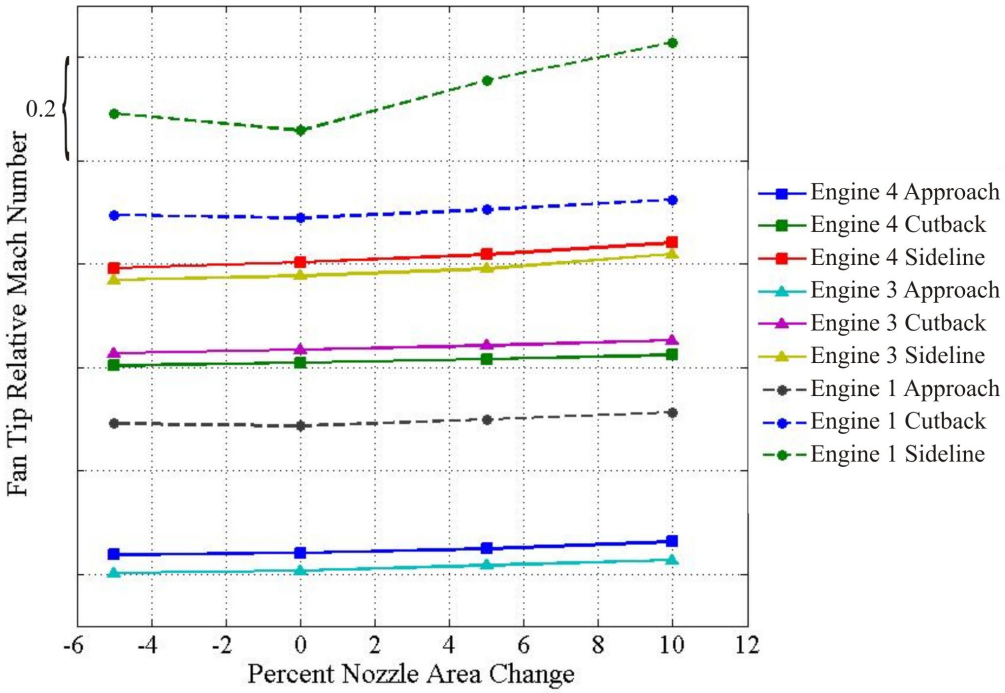

Figure 8.2.1-1 – Variation of M_{Rel} with nozzle area

Note that the Engine 1 fan speed is much higher than that of the Engine 4 and Engine 3, with a Mach number difference of approximately 0.25 for all flight cases. This difference has an influence on the derivation of the fan rig deltas in Section 8.3. Overall the increase in M_{Rel} is less than 4% over the range of nozzle area changes considered.

8.2.2. Variation of turbine speed with nozzle area

The variation of normalized turbine speed $\left(N/\sqrt{T}\right)_{Turbine}$ with nozzle area as predicted from the performance model, is shown below in Figure 8.2.2-1. As for fan shaft speed, *turbine speed increases with nozzle area* although actual increases are less than 2%. Again the Engine 1 engine at sideline is most sensitive to nozzle area.

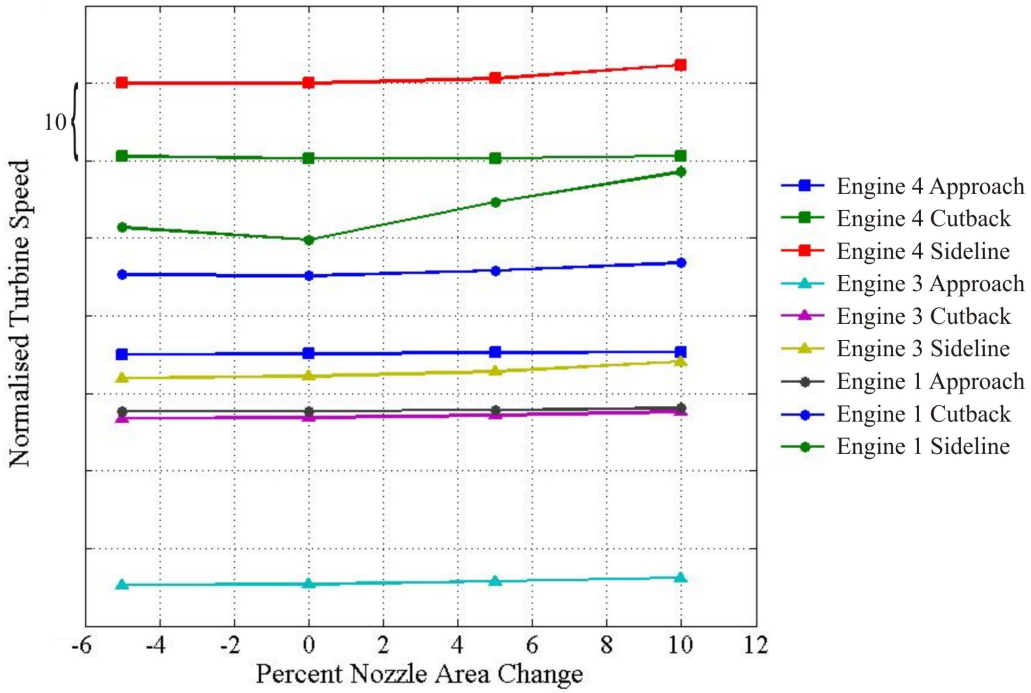

Figure 8.2.2-1 – Variation in $\left(N/\sqrt{T}\right)_{Turbine}$ with nozzle area

8.2.3. Variation of mixed jet velocity with nozzle area

As stated previously, the mixed jet velocity V_M is the average velocity of the jet when both the hot and cold nozzle streams are fully mixed. From conservation of mass, the *mixed jet velocity V_M decreases as nozzle area increases*. This is predicted from the performance model, as shown in Figure 8.2.3-1.

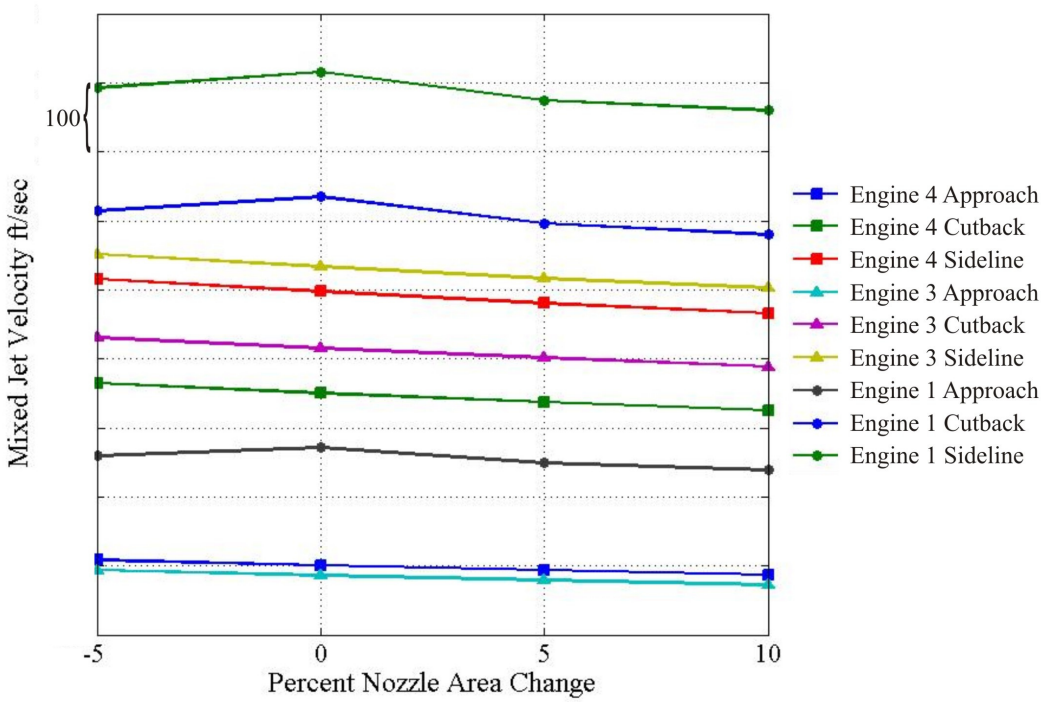

Figure 8.2.3-1 – Variation of mixed jet velocity with nozzle area

Note that the Engine 1 engine mixed jet velocity is considerably higher than that of the Engine 3 and Engine 4 engines. All engines, including the Engine 1, show the same percentage decrease in V_M for increasing nozzle area.

8.3. Determination of rig noise changes due to a nozzle exhaust area change

A full description of the method used to transfer noise deltas due to exhaust nozzle area changes, from rig scale measurements to engine scale noise predictions, can be found in Section 8.3.1 of Appendix X. A summary of the method can be found in Section 8.3.1 below.

Note that the procedure used during this investigation should not be used to predict working line changes between two completely different engines. In that case the fan is redesigned for each engine, in order to accommodate the working line shift in as efficient a manner as possible.

8.3.1. Summary of method for calculation of engine fan noise source changes using rig noise measurements

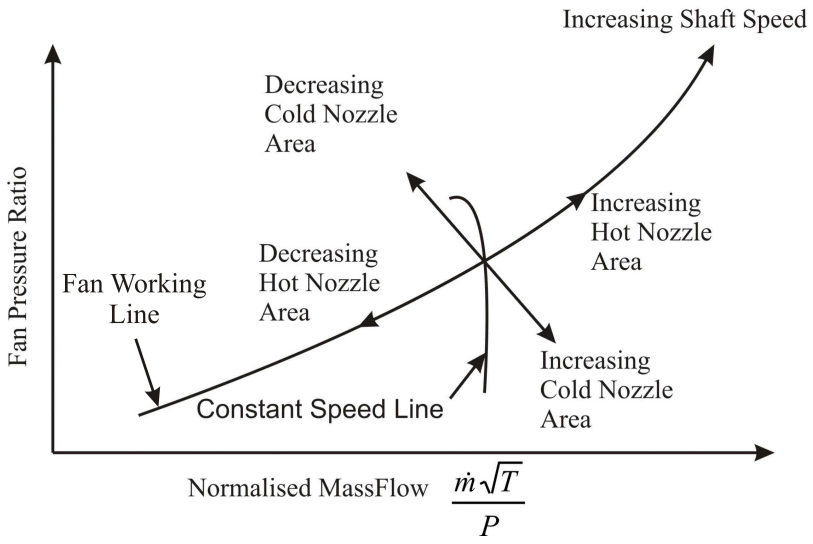

Figure 8.3.1-1 - Variation of fan operating map with exhaust nozzle area variations

Figure 8.3.1-1 displays a schematic of a fan working line, which traces the variation of fan pressure ratio and normalised mass flow with shaft speed. A change in either hot (core) or cold (bypass) nozzle area, while maintaining thrust, will move any point on this fan working line, as depicted in Figure 8.3.1-1. An increase or decrease in hot nozzle area will move the point up and down the working line respectively as the shaft speed changes. Cold nozzle area changes, which are under investigation within this study, are more complex.

Increasing the cold nozzle area reduces static pressure downstream of the fan. This reduces the pressure ratio required of the fan, which in effect moves the fan performance point onto a new working line. The increase in cold nozzle area also reduces jet velocity, as shown in Figure 8.2.3-1. In order to maintain thrust with this reduced jet velocity, the mass flow through the fan must increase $\left(Thrust = \dot{m}V\right)$. The fan must therefore rotate faster, as shown in Figure 8.2.1-1, to drive this increased mass flow at the reduced pressure ratio. Therefore this change in fan performance due to the cold nozzle area change incorporates both shaft speed and working line effects.

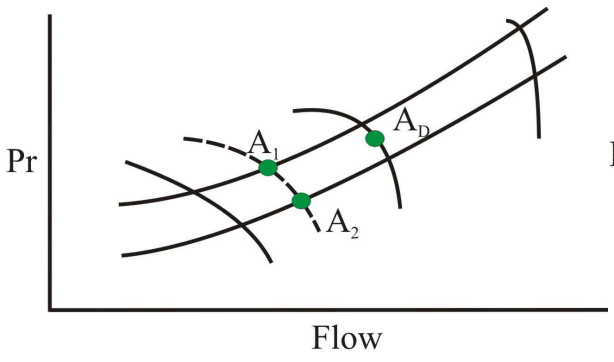

Figure 8.3.1-2 – Engine total rotor characteristics, to move from A_1 to A_2

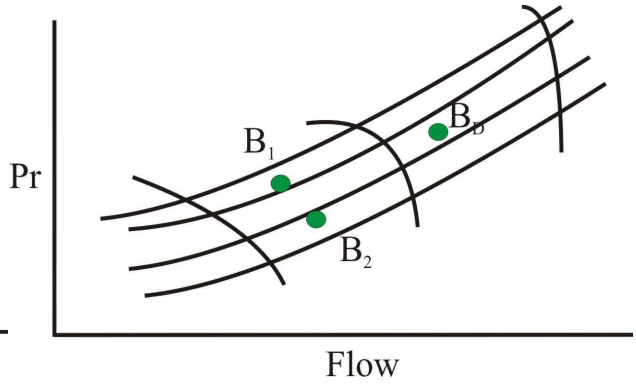

Figure 8.3.1-3 – Rig total rotor characteristics, to move from B_1 to B_2

This performance change for an increase in cold nozzle area is also shown schematically in Figure 8.3.1-2 in which point A_1 moves to point A_2, along the dashed line of constant thrust. Figure 8.3.1-2 is a schematic of the engine operating map[7] for which we would like to derive a noise delta as a result of moving from point A_1 to A_2. The procedure described in Section 8.3.1 of Appendix X predicts the fan noise deltas associated with the movement between these two performance points, for each individual fan noise source. As explained above, and displayed in Eq (8-1), this is achieved by separating these effects into those due to M_{Rel} and those due to working line changes. During this procedure engine and rig fan design points are required, and are denoted as A_D and B_D respectively.

The following sub-section describes the underlying method philosophy. This includes the identification of rig performance points that provide 'equivalent' fan noise deltas for input to the engine noise prediction model. Also listed in Section 8.3.2 of Appendix X, are the formal assumptions made that allow the application of this method philosophy.

8.3.2. Method philosophy

Using the new method described above and in Section 8.3.1 of Appendix X, the fan noise effects of working line changes are to be provided to the noise model from an external source, namely a fan rig noise measurement database. These external rig noise deltas provide a correction to the noise model for the incorporation of the effects of working line changes.

Two 'coordinates' are required in order to place the engine performance points on the rig operating map at points of 'equivalent noise'. Although *absolute rig noise levels at these operating points are not equal to engine noise at the same operating points*, these points must be placed so *the noise deltas are the same for both the rig and engine*. That is, the change in noise between the two points on the rig

[7] An 'Operating Map' is simply a diagram of fan working lines and characteristics, for either rig or engine. These trace the variation of pressure ratio versus flow for different shaft speeds.

operating map is the same as the noise change on the engine operating map, as shown below in Eq (8.3.2-1). The noise delta can then be transferred from the rig across to the engine noise model directly.

$$\Delta SPL\left(A_1 \rightarrow A_2\right) = \Delta SPL\left(B_1 \rightarrow B_2\right) \qquad \text{Eq (8.3.2-1)}$$

The first 'coordinate' used to locate the rig operating points, is the fan tip relative Mach number M_{Rel}. The absolute value of M_{Rel} is important, as both engine and rig scale fans must generate similar noise for the buzz and tone noise sources.

The second coordinate is more subtle. A parameter is required that will follow both rig and engine working lines, in order to allow the operating points to be transferred from engine to rig. Rig working lines are modified by changing the nozzle exhaust area. This nozzle area acts as the throttle on a real engine, and so this parameter is termed the 'throttle parameter', denoted ξ. The parameter chosen to fulfil this throttle matching role is normalised exhaust mass flow.

If the rig data being used was generated with the same fan design as on the engine, then the point of maximum efficiency (the design point) is directly transferable between operating maps. Broadband noise is sensitive to fan efficiency. At high speeds the degree of shock swallowing and therefore tone and buzz noise depends on the position of the operating point relative to the design point. *Therefore the second 'coordinate' used to place the engine operating points on the rig operating map is the ratio of* ξ *at the operating point in question, to* ξ *at the design point.*

For further information on the method, including a discussion on method accuracy, please see Sections 8.3.3. and 8.3.4 of Appendix X.

Chapter 9
Variable Area Nozzle Noise Prediction Results

9. Variable Area Nozzle Noise Prediction Results

This section will present and discuss selected noise results obtained from the investigation into the effect of a variable area nozzle on aircraft noise. Although all calculations were carried out for the Engines 1, 3, and 4, only selected illustrative results will be presented below in the main chapter body. Additional results will be included in the appendices.

Variable area nozzle predictions will be presented in three levels of detail. The first set of results present the variation of *total* aircraft and *total* engine noise with nozzle area. Results from Engines 1, 3, and 4 will be presented. The effect of a variable area nozzle on the various individual engine sources will then be discussed, particularly fan forward and rearward noise. These results will concentrate on Engine 3, with additional results displayed for Engine 1 at approach. Finally the variation in forward and rearward fan broadband noise with nozzle area is investigated, also for Engine 3.

9.1. Effect of a variable area nozzle on total aircraft and total engine noise

The following section presents results describing the effect of a variable area nozzle on total aircraft and total engine noise. It should be noted the approach undertaken in this study is to add a variable area nozzle to an 'existing' engine whose cycle is already pre-determined. An alternative approach would be to redesign the engine cycle to provide the greatest benefit for a change in nozzle area at each flight case. This second approach may extract larger noise benefits from an engine using a variable area nozzle, however this second approach is outside the scope of this thesis.

9.1.1. Noise sensitivity of total aircraft noise to variations in nozzle area

This section considers the effect of a variable area nozzle on total aircraft noise, corresponding to the sum of airframe noise and total engine noise.

The figures below show the variation of total aircraft noise with nozzle area for the three flight conditions. Figure 9.1.1-1, Figure 9.1.1-2, and Figure 9.1.1-3 show the results for Engines 1, 3, and 4 respectively. In these figures the 'cumulative' column denotes the summation of noise changes for each area at approach, cutback, and lateral. The 'Cumulative Best Areas' column denotes the

summation of the noise deltas at each flight condition that provide the largest improvement, regardless of nozzle area.

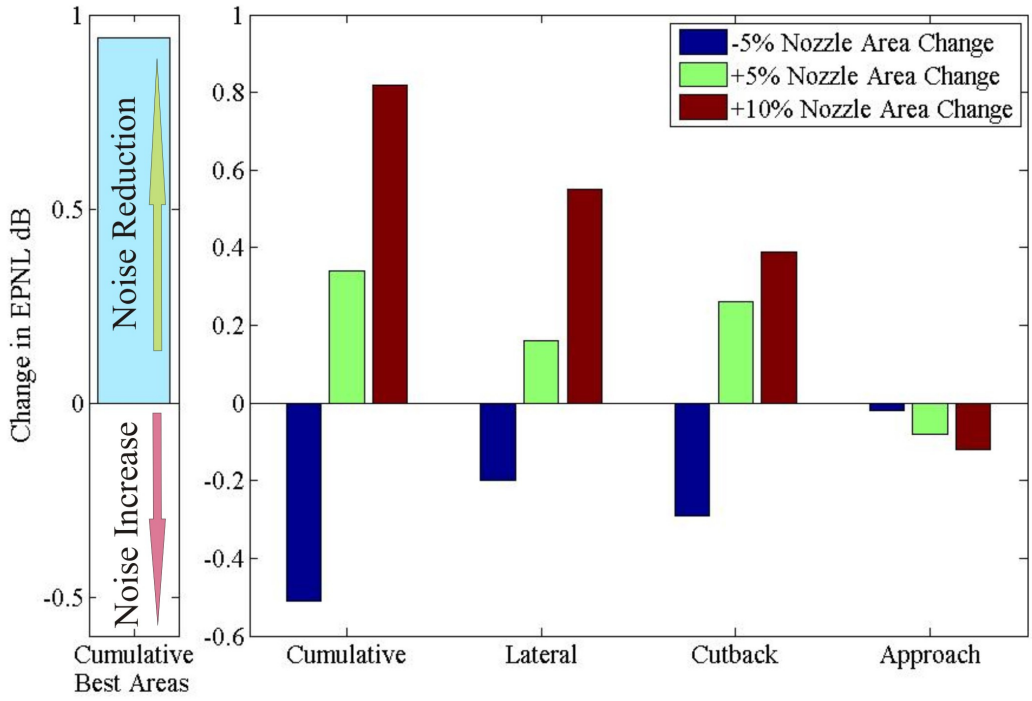

Figure 9.1.1-1 – Variation of total aircraft noise with variable area nozzle, Engine 4

Figure 9.1.1-1 predicts that the largest improvement for Engine 4 occurs at the sideline condition, with a benefit also at cutback. The most beneficial nozzle area at sideline and cutback is the +10% nozzle area change. Any nozzle area change at approach generates a noise increase. This is most likely due to the increasing shaft speed that is a consequence of an increase in nozzle area. Any reduction in nozzle area causes a noise increase on Engine 4, this is most likely due to the increase in jet velocity caused by a reduction in exhaust flow area, though individual engine noise sources must be investigated for confirmation of this assumption. For Engine 4 the cumulative best area changes are +10% at lateral and cutback, and the datum nozzle at approach. The maximum EPNL benefit predicted for Engine 4 is approximately 0.95dB.

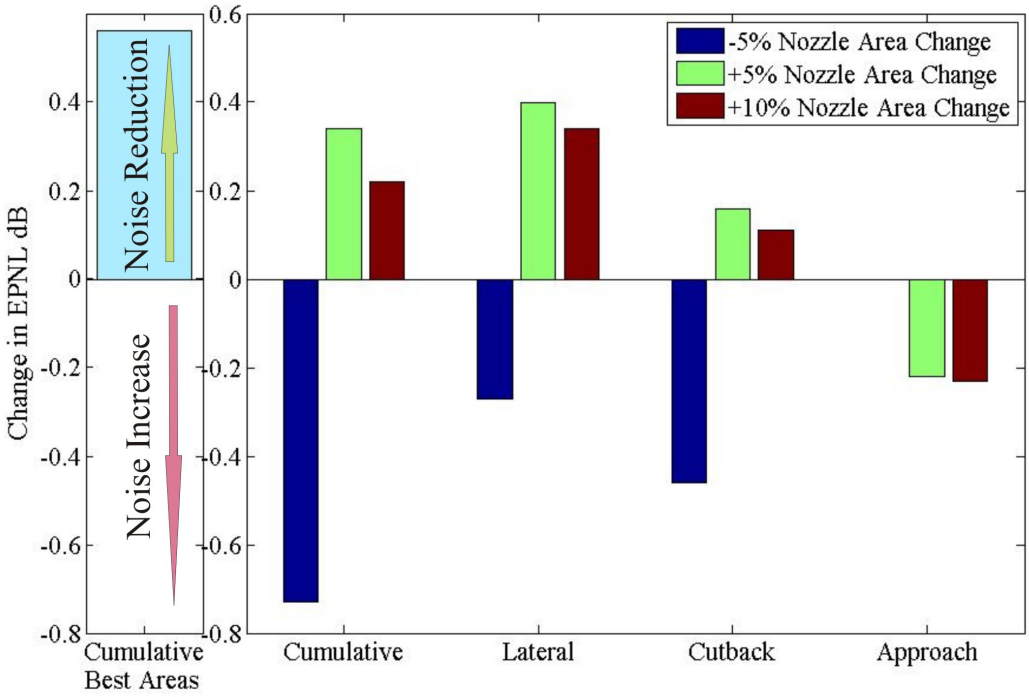

Figure 9.1.1-2 – Variation of total aircraft noise with variable area nozzle, Engine 3

Figure 9.1.1-2 shows the variation of total aircraft noise with variable area nozzle for Engine 3. It shows that Engine 3 also benefits in noise for larger nozzle areas at lateral and cutback conditions, though the most beneficial nozzle area is a +5% nozzle area change. Noise reductions are less than those predicted for Engine 4. A reduction in nozzle area is predicted to be detrimental at the lateral and cutback conditions, though this has no effect on noise generated at approach. For Engine 3 the changes most profound for a +5% nozzle area increase are at lateral and cutback, and the datum nozzle area at approach, providing a predicted noise benefit of approximately 0.6dB.

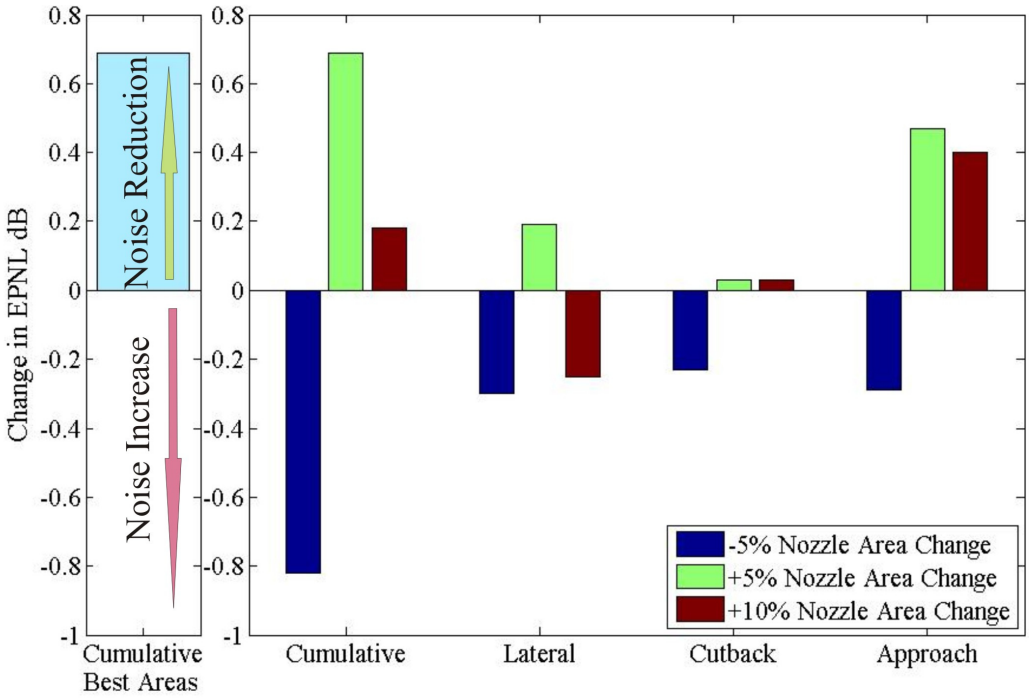

Figure 9.1.1-3 – Variation of total aircraft noise with variable area nozzle, Engine 1

Figure 9.1.1-3 shows the variation of total aircraft noise with variable area nozzle for the Engine 1 engine. In interpreting these results it is important to remember that noise at the approach flight position is predicted with fan rig noise deltas, while cutback and sideline were predicted with shaft speed change alone. Therefore only the approach flight case results are predicted with a complete input data set.

An interesting result obtained from the Engine 1 study in Figure 9.1.1-3 is that large noise benefits are predicted for the approach case. No noise benefit at approach is predicted for either Engines 3 or 4 for any nozzle area variation.

Shaft speed is expected to increase for an increase in nozzle area in order to produce the required thrust when the rotor generates a reduced pressure rise. This increase in shaft speed is seen from Figure 8.2.1-1 to be the case for all three engines, and would suggest that predicted noise behaviour should also be similar between the three engines. One can therefore postulate that this difference in prediction behaviour between the three engines at approach, is likely due to the fan rig noise deltas derived for Engine 1. The higher fan tip relative Mach number of Engine 1 generates matching rig positions that are located higher on the Engine 2 fan rig working lines (Figure 8.3.4-3 of Appendix X) than those of Engine 3 (Figure 8.3.4-2 of Appendix X) or Engine 4. As described in Section 8.3, these engine positions are overlaid onto the rig data using M_{rel} and throttle parameter ξ as matching parameters. Contrasting Figure 8.3.4-3 of Appendix X with Figure 8.3.4-2 of Appendix X, one can see

that the circles and squares denoting the positions for Engine 1 at approach, are in the vicinity of the B_M and B_2 marker positions for Engine 3 at cutback.

This may explain the improvement in noise levels for Engine 1. In this mid-region of the operating map many rig noise sources reduce in magnitude with reductions in fan pressure ratio, as seen in Section 4.4. The matched B_M and B_2 rig positions of Engine 1 therefore provide rig noise deltas of larger magnitude than those of Engines 3 or 4 for the approach flight position. This will be considered further below, when the effect of a variable area nozzle on individual engine sources (Section 9.2) are investigated.

At cutback and sideline, however, Engine 1 noise predictions are markedly different from the Engines 3 and 4 noise predictions. This is most likely due to the limitations met in deriving correct fan rig noise deltas.

The results for all three engines show a large degree of sensitivity to reductions in nozzle area of -5%. This suggests that a physical variable area nozzle need only be designed to provide increases in exhaust area. The 'best areas' cumulative total engine noise benefit for the Engine 4 engine is 0.9dB, 0.7dB for the Engine 1, and 0.6dB for the Engine 3 engine. The largest benefits seen for the Engine 4 and Engine 3 are found at sideline, although different nozzle areas provide this benefit for each engine.

9.1.2. Effect of variable area nozzle on total engine noise

Total aircraft noise is calculated by the noise model as the addition of total engine and airframe noise. Figure 9.1.2-1 below presents the variation of total engine noise with nozzle area variation for Engine 3 at the three noise certification points.

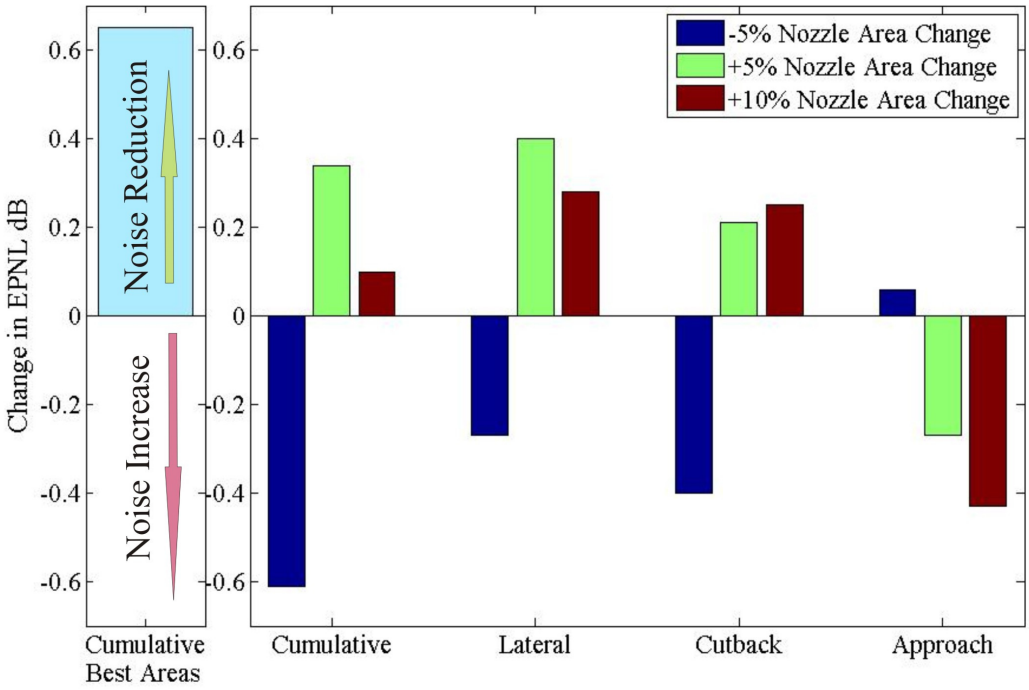

Figure 9.1.2-1 – Variation of total engine noise with variation in nozzle area, Engine 3

Comparing Figure 9.1.2-1 with Figure 9.1.1-2 for Engine 3 reveals that only noise magnitudes and not their relative importance are affected by nozzle area changes, with overall behaviour remaining comparatively constant. The noise reductions due to nozzle area change are larger for the engine alone. Total aircraft noise reductions are reduced by the addition of airframe noise. This is highlighted most markedly in the engine noise results of the approach case for Engine 3, where a reduction in noise is found for a smaller nozzle area.

Comparing the noise prediction of Figure 9.1.1-2 for total aircraft noise, with Figure 9.1.2-1 displaying total engine noise, shows that the changes in noise levels between total aircraft and total engine noise levels are small. However, the inclusion of the airframe noise contribution is sufficient to mask any improvement in the approach flight case found for a reduction in nozzle area. It is therefore important to consider both sets of predictions, total engine noise should not be considered alone. This example highlights the importance of working with the air-framer in future studies.

In order to more completely understand the noise effects of a variable area nozzle it is necessary to investigate the sensitivity of individual engine noise sources to a variable area nozzle. This is undertaken in the following section.

9.2. Variation of noise source levels with nozzle area variation

This section will consider the effect of a variable area nozzle on fan forward and rearward engine noise sources, to gain further understanding of the variations seen previously. Results displayed will concentrate on those of the Engine 3 engine, which will be shown for approach, cutback and sideline.

9.2.1. Engine 3 noise sources

The predicted variation of Engine 3 fan forward and rearward noise at approach, cutback, and sideline can be seen below in Figure 9.2.1-1. These noise changes are due to nozzle area changes from the nominal baseline nozzle geometry. The absolute noise levels of the subsources can be related to each other and additional engine noise sources by referring to Figure 3.1-2 in Section 3.1:

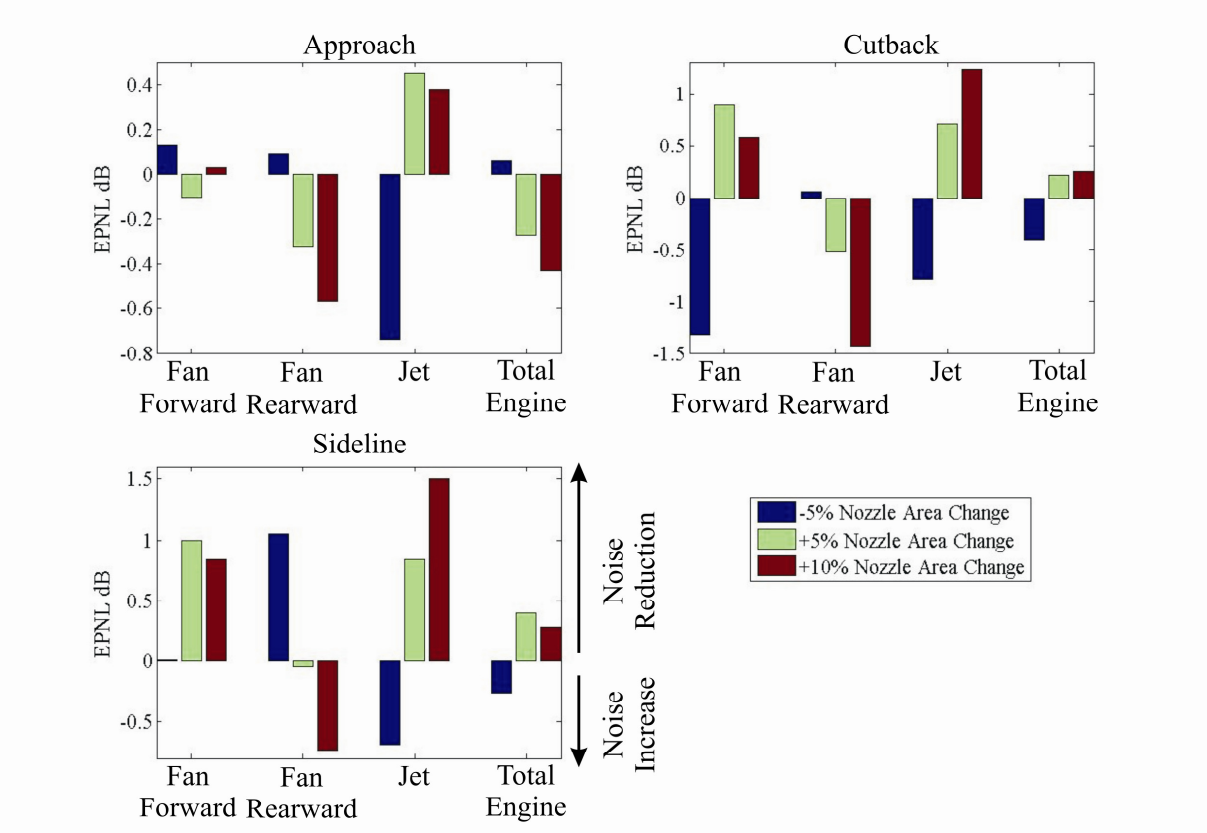

Figure 9.2.1-1 – Variation of in-flight subtotal noise sources, Engine 3

From Figure 3.1-2 the airframe noise source at the approach condition is predicted to be only slightly more quiet than the engine noise source, this is also true for Engine 3. Airframe noise is insensitive to variations in nozzle area, and acts to weaken the sensitivity of any noise variations due to changes in nozzle area. Fan forward and rearward noise, are the dominant engine sources for Engine 3 at approach. Although fan forward noise at approach is relatively insensitive to nozzle area changes, fan

rearward noise is predicted to increase by a small degree with nozzle area. This is most likely due to the increase in shaft speed, which is a consequence of an increase in nozzle area in order to maintain the specified constant thrust. The small increases in fan rearward noise is sufficient to cause the small increases in total engine noise for Engine 3 at the approach flight case. This is despite the reduction in jet noise caused by the larger nozzle area.

The Engine 3 noise source balance at cutback is clearly different than for approach, and shows much greater sensitivity to variations in nozzle area. For Engine 3 noise results at cutback, fan rearward noise again shows relatively large increases in noise for nozzle area increases. Jet noise is also an important contributor, from Figure 3.1-2 the jet noise source is seen to be louder than the fan noise source at departure. The jet noise source displays a consistent decrease in noise level for increasing nozzle area. This is due to the reduction in the mixed jet velocity caused by a larger nozzle exhaust area. Fan forward noise exhibits a large noise increase for the -5% nozzle, and a slight noise increase for the +10% nozzle area relative to the +5% nozzle area changes. This suggests that increasing the nozzle area beyond optimum will have a detrimental effect on fan forward noise. The reduction in jet, installation, and fan forward noise with a +5% increase in nozzle area are sufficient to generate the small improvements seen for total engine noise.

The three dominant noise sources for Engine 3 at sideline are the fan forward, fan rearward and jet noise sources. Jet noise is consistently reduced by increasing nozzle area, due to the reduction in mixed jet velocity. Fan rearward noise levels are predicted to increase with nozzle area. The behaviour of fan forward noise is again complex, showing no variation for smaller nozzle areas, before reducing for larger nozzle areas. The largest noise reduction is found for the +5% nozzle area change. The reductions in total engine noise for the sideline case appear to be mostly due to reductions in jet noise. As for the cutback flight case, the noise increases predicted for fan rearward noise at the sideline flight case, act to offset this noise improvement, thereby reducing potential benefits for increases in exhaust nozzle area.

The results of all three flight cases suggest that overall noise levels are extremely sensitive to fan noise changes at all three flight conditions. As the fan noise changes are strongly reliant on the rig noise deltas calculated from the Engine 2 data set using the method outlined in Section 8.2, by extension the total engine and total aircraft noise levels are also sensitive to the accuracy of these derived deltas. This highlights the necessity of using accurate rig noise deltas when attempting to model the noise effects of variable area nozzles. The following section considers the effects of exhaust nozzle area variation on noise sub-sources, specifically fan forward and rearward noise sub-sources.

9.2.2. Engine noise changes for Engine 1 at the approach flight case

Several engine noise sources for Engine 1 at approach are presented in Figure 9.2.2-1.

Apart from the large noise increase in fan forward noise for -5% nozzle area, the fan forward and fan rearward noise sources display little sensitivity to nozzle changes. As for Engine 3, jet noise decreases consistently with increasing nozzle area.

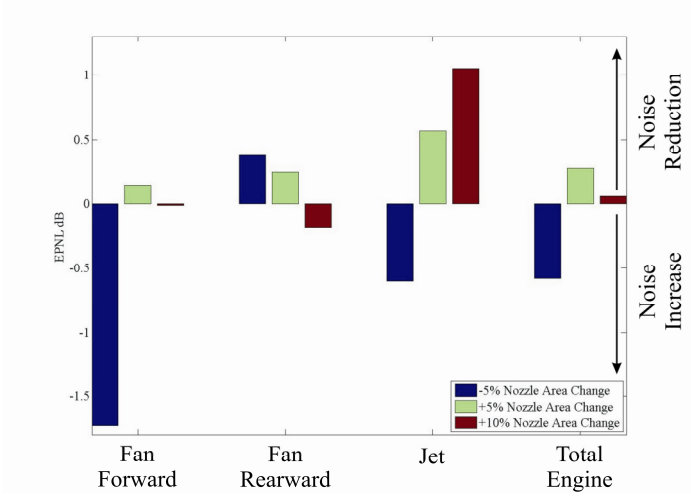

Figure 9.2.2-1 - Variation of in-flight subtotal noise sources, Approach, Engine 1

Unlike Engine 3 seen above, the Engine 1 noise model predicts a total engine noise reduction for the approach certification point. This is most likely due to differences in the fan noise deltas for these engines, extracted from the Engine 2 rig noise database. The higher fan tip relative Mach number of Engine 1 means that deltas for this engine are extracted from a different region of the Engine 2 rig operating map in terms of mass flow and pressure ratio (Figure 8.3.4-3 of Appendix X), compared to Engines 3 and 4 (Figure 8.3.4-2 of Appendix X). The engine positions are therefore in a region where a larger degree of variation in noise sources occurs, and so the Engine 1 matched rig deltas behave differently to those extracted for Engine 3.

The following section discusses the influence of varying nozzle area on the fan forward and rearward broadband noise of Engine 3.

9.3. Engine 3 broadband noise subsources

Figure 9.3-1 below displays the variation in fan forward and rearward broadband noise for Engine 3. The variation in the broadband noise subsource is investigated to see whether the behaviour is similar to that found during the second parameteric study of fan design parameters.

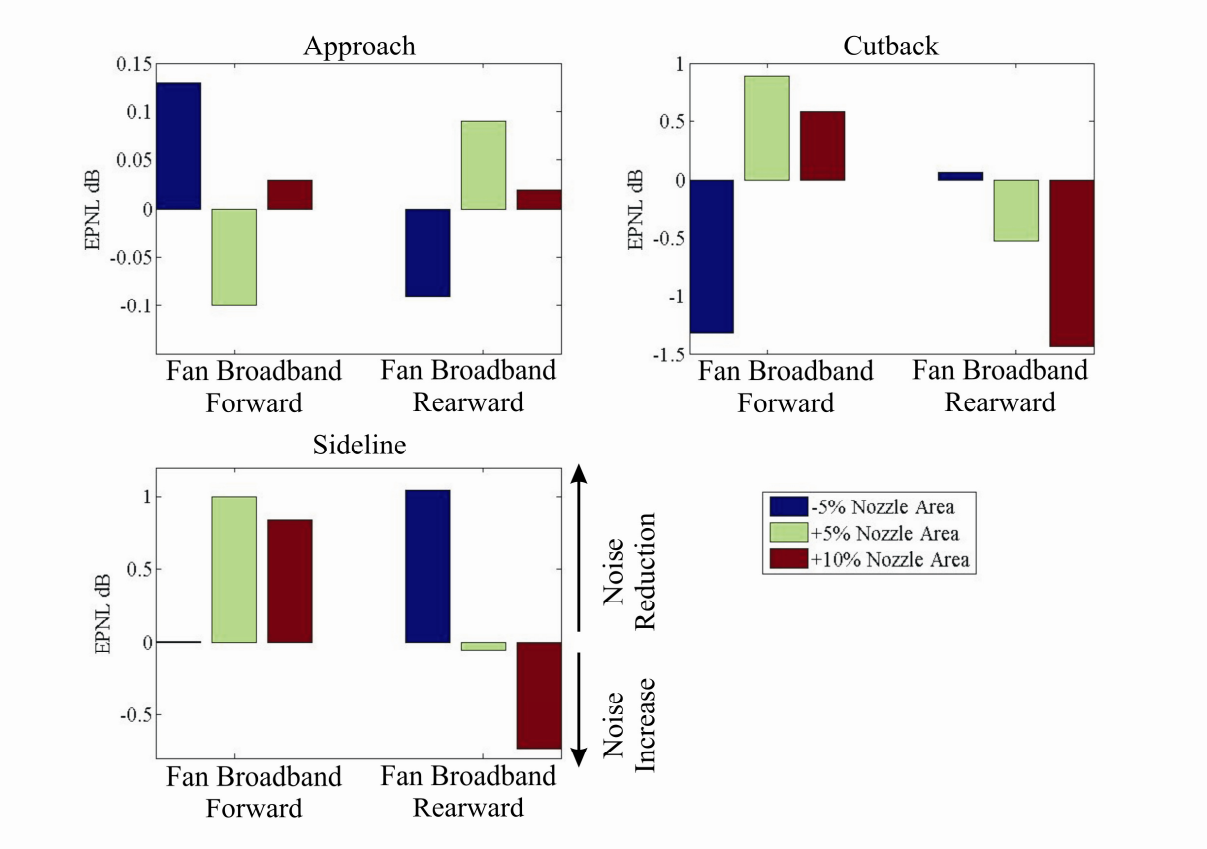

Figure 9.3-1 – Variation in forward and rearward fan broadband noise for Engine 3

Fan broadband noise at approach exhibits little sensitivity to variations in nozzle area over the complete range of nozzle areas. The variation of broadband noise at the cutback and sideline flight conditions exhibit a much higher degree of sensitivity to nozzle area increase.

At cutback and sideline, fan forward broadband noise varies in the opposite sense to fan rearward broadband noise. Noise reductions are predicted for fan forward broadband noise with increasing nozzle area, while fan rearward broadband noise increases for the same nozzle area changes. This is in agreement with the overall fan forward and rear noise variations seen in Figure 9.2.1-1.

As for the total fan forward noise, increasing the nozzle area beyond a 5% area increase, reduces the noise benefit. This suggests that increasing the nozzle area beyond optimum will reverse any benefits uncovered by moderate nozzle area increases. Further analysis of these results is included in Section 9.3 of Appendix X.

9.4. Summary

A new method has been developed to assess the noise effects of a variable area nozzle while maintaining constant thrust. This study is the first use of this method, and the predictions should be compared to experimentally measured data when such data is available.

The prediction method maps the relative working line changes from the Engine 2 rig measured noise data to the engine under consideration. The matching parameters are exhaust mass flow and total fan tip relative Mach number. The higher fan tip relative Mach number of Engine 1 introduced prediction inaccuracies at the cutback and sideline flight cases, which extended beyond the available Engine 2 rig data set. This highlights the reliance of the prediction method on accurate rig data, and suggests that the rig fan stage should be as close as possible to the engine fan stage.

From the results of this study cumulative total aircraft 'best area' noise benefits may be summarised as follows:

- Up to 1 aircraft EPNdB for Engine 4
- Up to 0.5 aircraft EPNdB for Engine 3
- Up to 0.7 aircraft EPNdB for Engine 1 – recall limitations

Any variation of nozzle area at approach is predicted to cause an increase in noise for Engine 3. This fact, combined with the noise reductions for increasing nozzle exhaust area at cutback and sideline, suggests that a variable area nozzle applied to this engine need only be designed to increase nozzle area from the datum.

As mentioned previously, the methodology used in this investigation was equivalent to adding a variable area nozzle to an existing engine. An alternative approach would be to design an engine with a variable area nozzle from the outset. This second approach, although outside the scope of this thesis, may provide further noise benefits over those already seen. The most important difference between these two approaches is that designing an engine to incorporate a variable area nozzle from the outset allows greater control over fan shaft speed. For example, at the approach flight position fan shaft speed could be reduced as nozzle area increases, thereby allowing a reduction in fan tip relative Mach number and subsequent associated noise benefits. The engines investigated as part of this study require a higher shaft speed as nozzle area increases for all flight cases including approach, thereby generating a higher fan tip relative Mach number.

Increasing the nozzle area is predicted to reduce noise for Engines 3 and 4 at cutback and sideline. Engine 1 results at these flight conditions are limited by inadequate fan rig deltas (c.f. Figure 8.3.4-2

of Appendix X), and highlight the need for accurate fan rig deltas when performing future investigations.

The similarity in noise behaviour between Engines 3 and 4 suggest that noise variation due to nozzle area change is similar for each engine at a particular flight position. The main differences between engines may therefore be due to differing engine and component architectures, causing each engine to possess different optimum nozzle areas at each flight case.

The behaviour of engine sources with variations in nozzle exhaust area is complex. Fan forward and rearwards noise sources are generally large contributors at all three flight conditions considered. For the three flight certification conditions considered, fan forward noise generally decreases with increasing nozzle area, while fan rearward noise increases with increasing nozzle area. This behaviour is sensitive to the fan rig noise deltas extracted from the Engine 2 rig noise database, and highlights the need for accurate fan rig noise deltas for use within the method.

Fan broadband noise in the rearward arc consistently increases with increases in nozzle area at cutback and sideline. Fan forward broadband noise decreases with increases in nozzle area. This decrease agrees with the findings of the cascade broadband noise parameter study carried out in Section 7.3. However, the forward arc broadband noise reduction may as likely be due to increasing rotor blockage due to the increasing shaft speed of the rotor with larger nozzle areas, which the noise model of Section 5 does not include.

Other engine sources, such as jet noise generally decrease with increasing nozzle area, due to the reduction in mixed jet velocity. The influence of these sources on total aircraft noise depends on the source balance of engine noise sources at each flight conditions.

Chapter 10
Future Work

10. Future Work

This study has highlighted several possibilities for future work.

The fan broadband noise cascade model predicts noise spectra in good agreement with measured data. However, recall that this is a 2-dimensional cascade model, for which the turbulence input is homogenous and isentropic. The model is currently under development to include a more accurate wake description [29], and 3-dimensional effects [31], which may provide additional accuracy to the broadband noise predictions. However, in order for the cascade model to be used in an industrial context, computational speed will also need to be improved.

A large database of rig measurements is available. Analysis of this database in the same fashion as the Engine 2 data may allow similar trends as found in Chapter 4b to be uncovered. A new modular fan test rig is under testing that may aid in the derivation of these new correlations.

During the study investigating the effect of a variable area nozzle on engine noise, the rig noise measurements were found to have a large influence on the extracted fan noise deltas. In future rig noise tests it would be beneficial were measurements to be taken within the large region between working lines 5, and 6 (as labelled in this report). This would allow a higher order polynomial to be fit through the noise data, and would have an important impact on final results considering the sensitivity of aircraft noise to fan noise sources at approach, cutback, and sideline.

In addition, the current method of transferring rig noise changes to engine noise predictions is based on two parameters; fan tip relative Mach number and a ‘throttle parameter’ related to mass flow. This method may be improved by being able to take into account changes in fan efficiency between different fan designs. This would allow the design performance of differing fans to be included, for example when the fan design in question possesses a different design operating point to the fan design whose rig measurements are being used to provide the noise changes.

Chapter 11

Conclusions

11. Conclusions

This thesis, with Appendix X, is the final report of this Engineering Doctorate. As mentioned previously, the EngD is a doctorate with an emphasis on providing additional training and industrial experience. This is gained by completing additional courses in technical, management, and skills training. Technical work is carried out with and for industry, both with respect to the nature of the work carried out for the sponsoring company, and by working in the sponsoring company for a significant portion of time. The sponsor is provided with the results of several years of study and research, the emphasis of which can be directed specifically by their needs. The research carried out as part of this EngD concentrates on increasing the understanding and modelling capabilities of aero-engine noise. The presented thesis reports the findings of several investigations into aero-engine noise sources, concentrating initially on fan noise. The following conclusions can be drawn from results shown in this publically available thesis.

The first, and central, investigation presented in this thesis examines fan rig noise measurements to provide greater understanding of the associated noise sources. These noise sources are both tone and broadband in nature, in both forward and rearward arcs. This rig noise investigation shows how the fan noise sources vary with pressure ratio and normalised mass flow on a working line diagram. Many of these results are shown in Appendix X, though the following conclusions can be drawn from the results shown in this thesis

- Rig data is useful as a means of understanding broadband noise.
- Rig data can be used to calculate fan noise changes due to changes in pressure ratio and mass flow.
- To reduce the magnitude of most fan noise sources, one should attempt to reduce fan pressure ratio and shaft speed.

The results of this investigation were used as input to, and to provide verification of, the other studies included in this project.

An additional analysis of a large rig noise measurement database was performed using several statistical techniques, with the correlation between different fan parameters and the measured noise providing a greater understanding of how the groupings reflect the physics of broadband noise generation. The following conclusions can be drawn from the results of this study:

- The complex relationships between predictors and measured broadband noise found in Chapters 4 and 7 can be reduced to simple linear correlations of the form of Eq (4.5-1).
- Statistical techniques are useful in attempting to identify uncorrelated independent predictor parameters.

Two example correlation equations are shown to predict low frequency broadband noise in the forward and rearward arcs, with good final agreement found when compared to rig measurements.

A fan rotor-stator interaction noise model was used to investigate this broadband noise source, for both simple geometric and aerodynamic cascade parameters, and fan design parameters. Modelled predictions of fan broadband noise were compared with rig measurements, showing good agreement.

Two parametric studies were carried out using the rotor-stator interaction broadband noise model. The first parametric study investigated the effect on broadband noise of varying simple geometric and aerodynamic cascade parameters. The results of the first parametric study were used to derive scaling power laws that allow a degree of prediction of the change in broadband noise between two flight conditions. Some of the most important findings of the first parametric study are:

- The variation of low and high frequency broadband noise is different, and must be treated separately.
- There is a simple relationship between broadband noise, and flow turbulence intensity and vane chord.
- The relationship between broadband noise, and turbulent length scale, number of vanes, and stagger angle is complex.
- The high frequency analytical model shows good agreement with predicted high frequency broadband noise when integrated over a frequency band.

The second parametric study investigated the effect of varying fan design parameters (efficiency, pressure ratio and shaft speed) on fan broadband noise at cruise, cutback and approach flight conditions. While the variation in broadband noise due to changes in shaft speed and efficiency are shown in Appendix X, the following conclusions can be drawn from results displayed in this main thesis document:

- Reducing fan pressure ratio reduces broadband noise.
- The sound power scaling laws derived as part of the first parametric study can be used to predict the change in fan broadband noise between different fan performance points along and between fan working lines. This prediction is more accurate at high frequencies.
- Flow Mach number onto the OGVs is the most significant parameter in the prediction of broadband noise.

Another major section of this thesis presents an investigation into the total aircraft and total engine noise effects of a variable area nozzle on several engines, at certification flight points. Variable Area Nozzles are a technology currently under investigation for their potential benefits to both engine performance and noise. This study provides a procedure for incorporating fan noise changes due to

nozzle area variations into the prediction of the total engine noise. The following conclusions can be drawn:

- A new method was presented for the incorporation of fan noise changes due to the working line effects of varying exhaust nozzle area. This method used fan rig noise data to provide the noise changes due to working line effects.
- The new method was applied to several study engines, at the noise certification flight points, and was shown to be a practical approach to the incorporation of fan noise effects due to changes in exhaust nozzle area.
- Variable area nozzles are shown to be a useful means of reducing engine noise, though different nozzle areas are required to provide a reduction in noise at different flight points
- Increasing nozzle area will generally reduce fan forward noise and jet noise, while increasing fan rearward noise. The overall engine noise benefit is therefore due to a reduction in fan noise and jet noise sources, the contribution of which depends on flight point. The reduction in jet noise for an increased nozzle area on Engine 3 is greater than the reduction in fan noise, at all flight points investigated.
- An optimal nozzle area exists at each flight point; increasing nozzle area beyond this optimum reduces the noise benefit.

12. References

1 **Analytical Investigation of Compressibility and Three Dimensionality on the Unsteady Response of an Airfoil in a Fluctuating Flow Field**
United Aircraft Research Laboratories Report L911359-2, 1972
J. J. Adamczyk

2 **Passage of an Isolated Airfoil Through a Three-Dimensional Disturbance**
Ph.D. Thesis, University of Connecticut, United Aircraft Report UAR-K97, 1971
J. J. Adamczyk

3 **The Aerodynamic Noise of Small-Perturbation Subsonic Flows**
Journal of Fluid Mechanics, Vol. 44, 1970, pp. 227-235
R. K. Amiet and W. R. Sears

4 **Acoustic Radiation from an Airfoil in a Turbulent Stream**
Journal of Sound and Vibration (1975) 41(4), 407-420
R. K. Amiet

5 **Noise Due to Turbulent Flow Past a Trailing Edge**
Journal of Sound and Vibration (1976) 47(3) 387-393
R. K. Amiet

6 **Review of Unsteady Airfoil Lift Theories**
United Aircraft Research Laboratories, Report M210885-2
R. K. Amiet

7 **Fundamentals of Aerodynamics – Second Edition**
McGraw-Hill International Editions, ISBN 0-07-100767-9
John D. Anderson, Jr

8 **Effect of Turbulence Structure on Broadband Fan Noise**
14th AIAA/CEAS Aeroacoustics Conference AIAA 2008-2842
H. M. Atassi, M. M. Logue

9 **Modelling Broadband Fan Noise and Comparison with Experiments**

13th AIAA/CEAS Aeroacoustics Conference AIAA 2007-3691

H. M. Atassi, I. V. Vinogradov

10 **The Joint Rolls-Royce/Boeing Quiet Technology Demonstrator Programme**

10th AIAA/CEAS Aeroacoustics Conference AIAA 2004-2869

P. Bartlett, N. Humphreys, P. Phillipson Rolls-Royce plc

J. Lan, E. Nesbitt, J. Premo The Boeing Company

11 **High frequency formulation for the acoustic power spectrum due to cascade-turbulence interaction**

Journal of the Acoustic Society of America, 119 (1), January 2006

C. Cheong, P. Joseph, S. Lee

12 **Jet Propulsion – A simple guide to the aerodynamic and thermodynamic design and performance of jet engines, second edition**

Cambridge University Press, ISBN 0521 541441

N. Cumpsty

13 **Turbulent Wake Predictions for Broadband Noise Calculations**

Institute of Acoustics, Vol. 28, Pt. 1, 2006

E. Deane, P. Joseph,

14 **Measurement and Modelling of the Two-Point correlation Tensor in a Plane Wake for Broadband Noise Prediction**

NASA Report VPI-AOE-263 May 1999

William J. Devenport, Stewart A. L. Glegg

15 **Theory of Airfoil Response in a Gusty Atmosphere, Part 1 – Aerodynamic Transfer Function**

University of Toronto, Institute for Aerospace Studies, UTIAS Report No. 139, October 1969

L. T. Filotas

16 **Boeing 18-Inch Fan Rig Broadband Noise Test**

NASA/CR-1998-208704

U. W. Ganz, P. D. Joppa, T. J. Patten, D. F. Scharpf

17 **Measurement and Prediction of Broadband Fan Noise**
AIAA-98-2316
Ulrich Ganz, Stewart A.L. Glegg, Paul Joppa

18 **Rotor/Stator Interaction Noise from Blade Wakes**
AIAA 2001-2150
7th AIAA/CEAS Aeroacoustics Conference, May 2001, Maastricht, Netherlands
Stewart A.L. Glegg, William J. Devenport

19 **Broadband Self Noise from a Ducted Fan**
AIAA 97-1612
3rd AIAA/CEAS Aeroacoustics Conference, May 1997, Atlanta, Georgia
Stewart A. L. Glegg, Cyrille Jochault

20 **The Response of a Swept Blade Row to a Three-Dimensional Gust**
Journal of Sound and Vibration (1999) 227(1), 29-64
S. A. L. Glegg

21 **Aeroacoustic Prediction Codes**
NASA/CR-2000-210244
P.Gliebe, R Mani, H. Shin, B. Mitchell, G. Ashford, S. Salamah, S. Connell

22 **UHB Engine Fan Broadband Noise Reduction Study**
NASA/CR198357, June 1995
P. R. Gliebe, P. Y. Ho, R. Mani

23 **Aeroacoustics**
1976 McGraw-Hill
Marvin E. Goldstein

24 **Similarity Rules for This Aerofoils in Non-Stationary Flows**
Journal of Fluid Mechanics, Vol 43, 1970, pp. 753-766
J. M. R. Graham

25 **Gust response analysis for Cascades Operating in Nonuniform Mean Flows**
AIAA Journal, Vol. 29, No. 9, September 1991, pp. 1463-1471
Kenneth C. Hall, Joseph M. Verdon

26 **Theory for Broadband Noise of Rotor and Stator Cascades With Inhomogeneous Inflow Turbulence Including Effects of Lean and Sweep**

NASA/CR-2001-210762

Donald B. Hanson

27 **Multi-mode sound transmission in ducts with flow**

Journal of Sound and Vibration, 264 (2003), 523 - 544

P. Joseph, C. L. Morfey, C. R. Lowis

28 **A comparison between measured and predicted fan broadband noise due to rotor stator interaction**

13th AIAA/CEAS Aeroacoustics Conference, May 2007, AIAA-2007-3692
Vincent Jurdic, Antoine Moreau, Phillip Joseph, Lars Enghardt, John Coupland

29 **Turbulence cascade interaction noise**

Proceedings of the Institute of Acoustics, Vol. 28. Pt. 1. 2006
Vincent Jurdic, Phillip Joseph

30 **The Unsteady Forces Due to Viscous Wakes in Turbomachines**

Journal of Aeronautical Sciences, Vol. 22, No. 7, July 1955, pp. 478-483

N. H. Kemp, W. R. Sears

31 **Rotor-Stator Broadband Noise prediction**

14th AIAA/CEAS Aeroacoustics Conference, AIAA-2008-2840
A. E. D. Lloyd and N. Peake

32 **Noise Due to Inlet Distortion or Turbulence**

NASA CR2479, 1974

R. Mani

33 **Sound transmission through blade rows**

Journal of Sound and Vibration (1970) **12**(1), 59-83

R. Mani and G. Horvay

34 **Aircraft Engine Design**

AIAA Education Series, 1987, ISBN 0-930403-23-1

J. D. Mattingly, W. H. Heiser, D. H. Daley

35 **Improvements of a parametric model for fan broadband and tonal noise**
Euronoise, Acoustics '08 proceedings
A. Moreau, L. Enghardt

36 **On the relation between broadband noise and fan aerodynamic performance**
Fan Noise 2007, Lyon (France) 17 - 19 September 2007
A. Moreau, L. Enghardt, H. Boden

37 **Computation of rotor wake turbulence noise**
Journal of Sound and Vibration 282 (2005) 649-678
M. Nallasamy, E. Envia

38 **The interaction between a high-frequency gust and a blade row**
Journal of Fluid Mechanics (1992), vol. 241, pp. 261-289
N. Peake

39 **Fan Source Diagnostic Test – LDV measured flow field results**
8th AIAA/CEAS Aeroacoustics Conference and Exhibit, June 2002, AIAA-2002-2431
Gary G. Podboy, Martin J. Krupar, Christopher E. Hughes, Richard P. Woodward

40 **Turbulent Flows**
Cambridge University Press, ISBN 0-521-59886-9
S. B. Pope

41 **Boundary Layer Theory – 8th Revised and Enlarged Edition**
Springer-Verlag, 2000, ISBN 3-540-66270-7
H. Schlichting, K. Gersten

42 **Some Aspects of Non-Stationary Airfoil Theory and its Practical Application**
Journal of the Aeronautical Sciences, Vol. 8, No. 3, 1941, pp. 104-108
W. R. Sears

43 **Discrete Frequency Sound Generation in Axial Flow Turbomachines**
Aeronautical Research Council, Reports and Memoranda No. 3709, 1972
S. N. Smith

44 **Axial Flow Compressor Noise Studies**
S.A.E. Transactions, 70
J. M. Tyler and T. G. Sofrin

45 **AGARD Manual on Aeroelasticity in Axial-Flow Turbomachines, Volume 1, Unsteady Turbomachinery Aerodynamics, AGARD-AG-298 Vol. 1**
Classical Two-Dimensional Methods
D.S. Whitehead

46 **Fan Source Diagnostic Test – Far-field acoustic results**
8th AIAA/CEAS Aeroacoustics Conference and Exhibit, June 2002, AIAA-2002-2427
R. P. Woodward, C. E. Hughes, R.J. Jeracki, C.J. Miller

47 **Benefits of Swept and Leaned Stators for Fan Noise Reduction**
NASA/TM-1998-208661 AIAA-99-0479
Richard P Woodward, David M Elliott, Christopher E Hughes, Jeffrey J Berton

48 **Noise Benefits of Increased Fan Bypass Nozzle Area**
NASA/TM-2004-213396 AIAA-2005-1201
Richard P Woodward, Christopher E Hughes

49 **Aeroacoustics Analysis of Fan Noise Reduction with Increased Bypass Nozzle Area**
NASA/TM-2005-213825 AIAA-2005-3075
Richard P Woodward, Christopher E Hughes, Gary G. Podboy

50 **On the large-scale structures in two-dimensional, small-deficit, turbulent wakes**
Journal of Fluid Mechanics (1986), vol. 168, pp. 31 – 71
I. Wygnanski, F. Champagne, B. Marasli

51 **Parliamentary Office of Science and Technology, April 2003 Number 195 Report Summary**

52 **The Jet Engine, Rolls-Royce Technical Publications, 2005**

53 **Fluent 6.0 Documentation**
Modelling wall roughness effects in turbulent wall bounded flows
6.13.1 Inputs at Wall Boundaries

54 **http://geolab.larc.nasa.gov/APPS/YPlus/**

55 **Variable Area Nozzle Study – Use of Fan Rig Data**

Draft, April 2008
Alexander G Wilson

56 **http://www.grc.nasa.gov/WWW/RT/2004/RS/RS13S-lee.html**

NASA variable area nozzle investigation

Appendices

Appendix A-1 : Plane Wake Theory

A visualisation of the plane wake downstream of a symmetrical aerofoil can be seen in Figure 0-1. The profiles are made visible in water flow by causing a voltage pulse through a straight ware orientated perpendicular to the flow. This creates small hydrogen bubbles that are then convected downstream. These velocity profiles clearly show the effect of the body on the flow, creating a velocity deficit profile.

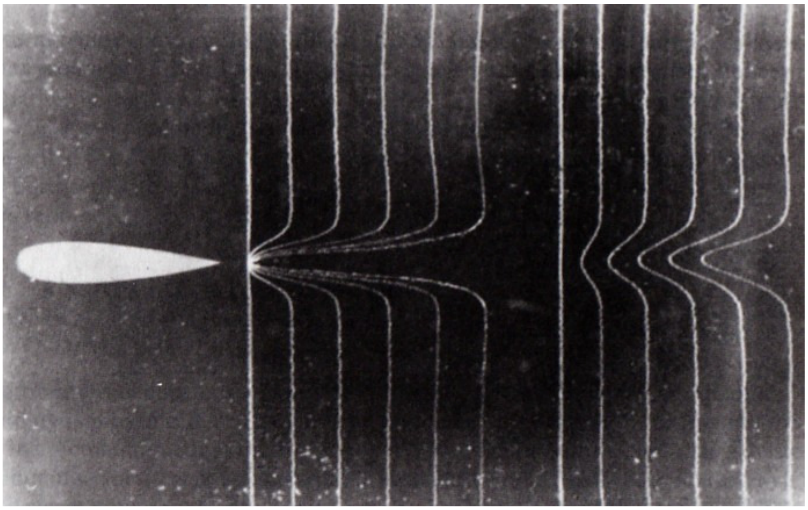

Figure 0-1 - Wake of Symmetrical Aerofoil - Laminar Flow [7]

In a turbulent wake this profile is also present in the mean flow, though superimposed by the turbulent fluctuations. The mean wake can be characterised by the maximum velocity deficit U_w (lying along the centre-line), and the half-wake width L_w (the y-position where the wake mean velocity is ½ U_w).

The classical work by Wygnanski [50] is a detailed study of large-scale structures in 2-dimensional small deficit turbulent wakes. Several wake generators are studied, including a thick symmetrical aerofoil. This investigation studied self-similarity in the far wake, specifically to assess whether a single velocity and length scale can be used to describe the flow.

In this section we review the theory of plane (2-dimensional) wakes generated by a 2-dimensional symmetric aerofoil situated in a uniform mean flow. A 2D wake is formed when a uniform flow U_∞ in the x-direction flows over a 2D object that is symmetrical about the horizontal axis ('*x-axis*' in Figure

0-2). The resulting wake is assumed 2-dimensional, and symmetric about the y plane as shown schematically below in Figure 0-2.

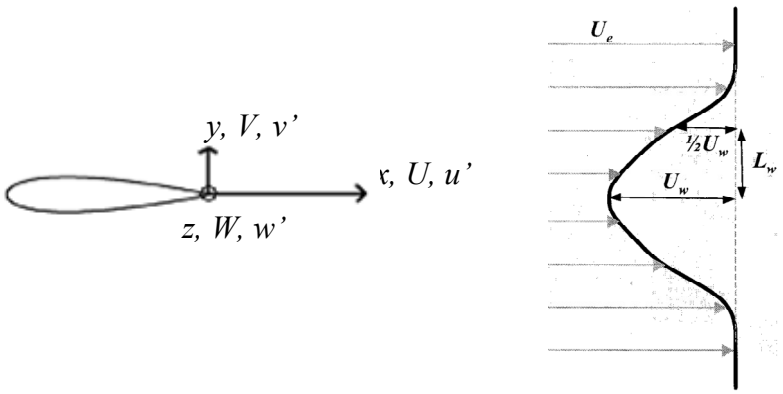

Figure 0-2 - Definitions of axes and mean wake variables

Figure 0-2 also defines the maximum wake velocity deficit $U_w(x)$ and half-wake width $L_w(x)$, and wake edge velocity U_e. The wake edge velocity is the mean flow velocity at the wake edge, assumed to be approximately $0.99U_\infty$, where U_∞ is the freestream velocity. The velocity difference, or deficit, is defined as the difference between the velocity at the wake centreline and the free-stream velocity:

$$U_w(x) = U_\infty - U(x,0,0) \qquad \text{Eq (0-1)}$$

The half-wake width is defined as the distance between the wake centreline and the wake position where the velocity defect is half that of the maximum velocity defect, i.e.

$$U\left(x \pm L_w, 0\right) = U_\infty - \tfrac{1}{2}U_w(x) \qquad \text{Eq (0-2)}$$

As the wake convects downstream of the aerofoil the wake profile spreads i.e. L_w increases, and U_w/U_∞ decays with increasing downstream distance x. For this reason the flow cannot be exactly self-similar but does tend towards asymptotic self-similarity in the far-wake. In experimental investigations of 2-dimensioal wakes, self-similar behaviour has been seen when the velocity ratio U_w/U_∞ is less than about 1/10. Wygnanski et al noted self-similar behaviour downstream of a circular cylinder at $x/\theta \approx 400$, where θ is the momentum thickness of the cylinder.

Appendix B-1 : Self-similar relationships for 2-dimensional wakes

This section will present relationships for the wake spreading parameter, and self-similar relationships for U_w and L_w. In the region of self-similar behaviour the transverse variation of mean velocity and Reynolds Stresses assume forms that are independent of x when normalised by U_w and L_w. Defining $\eta = y/L_w$, the self-similar velocity defect profile can be described in terms of the normalized function $f(\eta)$:

$$f(\eta) = \frac{U_\infty - U(x,y,0)}{U_w(x)} \qquad \text{Eq (0-3)}$$

Equation 0-3 can be rewritten as:

$$U(x,y) = U_\infty - U_w(x) f(\eta) \qquad \text{Eq (0-4)}$$

By definition $f(0) = 1$, and $f(\pm 1) = 0.5$. The Reynolds Stress variation can also be written in terms of a normalised function;

$$g(\eta) = \langle uv \rangle / U_w^2 \qquad \text{Eq (0-5)}$$

The conditions under which self-preserving flow is possible can be obtained by substituting self-preserving velocity distributions (such as $U(x,y)$ in Equation 0-4) into the equations of mean momentum and turbulent kinetic energy [50]. This results in the following relation:

$$\frac{U_\infty L_w}{U_w^2}\frac{dU_w}{dx} \propto \frac{U_\infty}{U_w}\frac{dL_w}{dx} \qquad \text{Eq (0-6)}$$

The term on the right hand side of Equation 0-6, involving the gradient of the half-wake width, is defined as the wake spreading parameter:

$$S = \frac{U_\infty}{U_w}\frac{dL_w}{dx} \qquad \text{Eq (0-7)}$$

Self-similarity states that the spreading rate should be constant. In the far wake the product $U_w(x)L_w(x)$ should be independent of x, and, together with the constancy of the spreading parameter, imply that U_w and L_w should vary as $x^{1/2}$ and $x^{-1/2}$ respectively.

A quantity that is fundamental to the prediction of the wake is the momentum thickness θ, which can be derived from the momentum integral equation

$$\theta = \frac{F}{\rho U_\infty^2} = \int_{-\infty}^{\infty} \frac{U(x,y)}{U_\infty}\left(1 - \frac{U(x,y)}{U_\infty}\right)dy \qquad \text{Eq (0-8)}$$

The drag force F per unit span and freestream velocity U_∞ (not equal to $\mathrm{Ue} = 0.99\mathrm{U}_\infty$) are constants of the wake generator that are independent of x. It can therefore be shown that in the far wake [50]:

$$\frac{U_w}{U_\infty} \sim \left[\frac{F}{\rho U_\infty{}^2 (x - x_0)}\right] \sim \left[\frac{2\theta}{(x - x_0)}\right]^{\frac{1}{2}} \qquad \text{Eq (0-9)}$$

$$\frac{L_w}{\theta} \sim \left[\frac{F(x - x_0)}{\rho U_\infty{}^2}\right] \sim \left[\frac{(x - x_0)}{2\theta}\right]^{\frac{1}{2}} \qquad \text{Eq (0-10)}$$

which clearly identifies the momentum thickness θ as the appropriate normalising length scale. Note that a factor of 2 has been introduced in Equations 0-9 and 0-10 for consistency with Wygnanski et al [50]. The momentum thickness can be related to the force on the blade by:

$$\tau_w = \rho U \frac{d\theta}{dx} \qquad \text{Eq (0-11)}$$

where τ_w is the shear stress at the wall (the integral of this shear stress around the blade surface provides the friction force experienced by the blade). Equations 0-9 and 0-10 suggest that at any position x from the wake generator, L_w and U_w can be predicted from knowledge of only θ.

To obtain these self-similar relationships it has been necessary to introduce the concept of the virtual origin x_0. This is the point relative to the wake generator from which the wake appears to originate. It is used to account for viscous and Reynolds number effects, and depends on generator geometry.

Appendix C-1 : Correlation Methods for Estimation of Wake Turbulence Parameters

This, and the following C-appendices, is a review of measurements made of the mean and turbulence properties of the wake generated by a rotor in a ducted fan. In particular 'correlation' results, which relate the steady and unsteady wake characteristics by similarity rules, are reviewed. The aim is to be able to predict the turbulence characteristics of the wake from predictions of the mean wake and other steady aerodynamic quantities such as the rotor pressure loss. This section also ascertains whether the wakes generated by ducted fans follow the classical similarity rules established for 2D wakes generated by symmetrical aerofoils under laboratory conditions.

Appendix C-2 : Correlation Approach of Gliebe et al

The classical work of Wygnanski et al [50] outlined in the literature review suggests that correlations deduced from elementary theory may be used to predict turbulence quantities in the wake from measurements of the mean wake and momentum thickness. Based on this approach Gliebe et al [21] provide a model for predicting the mean and turbulent wake parameters in the exit flow downstream of a fan. Gliebe et al derived results that relate the various turbulent wake parameters to other more easily measurable mean aerodynamic parameters. This approach will be central to the development of a similar correlation model for use in the broadband noise estimation model. Ganz et al measured a number of turbulent and mean wake quantities; these are compared below to the results of Gliebe et al and the similarity rules proposed by Wygnanski et al.

The wake measurements analysed by Gliebe et al are taken at 5 axial distances downstream of the rotor between $0.13 < x/c < 2$, where c is the aerofoil chord. Since the momentum thickness is not specified in these tests it is unknown whether these limits overlap with the experimental measurement range of Wygnanski et al, of $100 < x/\theta < 2000$. However, Gliebe et al state that these measurement positions are sufficiently far downstream for the wake to be fully developed and self-similarity has been reached, thereby allowing the use of the approach proposed by Wygnanski et al to be applied.

An important assumption made by Gliebe et al is that Mach number effects (for example shocks or expansions) on the evolution and behaviour of rotor wakes are of second order, and that viscous and rotor loading effects dominate the wake behaviour. The Low Speed Research Compressor blades used by Gliebe et al are modelled to simulate the corresponding high-speed compressible surface pressure distributions. Therefore transonic and supersonic Mach number pressure distributions are implicitly

modelled excluding any shock-boundary layer effects. The assumption is reasonable as long as the rotor inlet relative Mach number is below approximately 1.1.

As a first step to collapsing the data the mean wake velocity profile is normalised by the maximum wake velocity deficit U_w and the half-wake width L_w. Note that Gliebe et al present U_w and L_w for both the mean relative velocity and turbulence intensity wake profiles at each downstream measurement position. This is seen below in Figure 0-3 for $x = 0.5"$. However, it is not clearly specified whether L_w as derived from the mean velocity profile or the turbulence intensity profile is used to derive the correlations. It is assumed that for the calculation of mean relative velocity wake correlations, U_w and L_w are deduced from the average relative velocity profiles. To calculate turbulent intensity correlations, U_w and L_w are deduced from profiles of the turbulence intensity. It is seen that L_w derived from the turbulent intensity profile is slightly wider than that of the mean velocity profile.

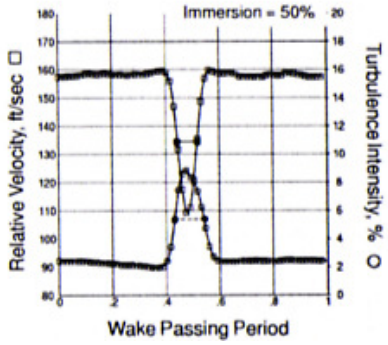

Figure 0-3– Variation of relative velocity and turbulence intensity over one wake period axial position x = 0.5" [21]

Of interest in broadband noise modelling is the turbulent velocity component normal to the leading edge of the stator vanes.

Now consider the final wake correlation model of Gliebe et al is displayed. In addition to mean velocity profile correlations of U_w and L_w, the measured wake turbulence is also investigated both in terms of turbulence intensity and turbulent velocity components, and turbulence integral length scales. Note that the turbulence intensity and turbulence integral length scales are the necessary inputs to broadband noise models.

Gliebe et al have investigated the degree to which the approach of Wygnanski et al. could be used to form correlations of rotor wake turbulence data. The first order correlation formulae for wake half-width and maximum wake velocity deficit for the turbulent wake profile are shown below in Equations 0-12 and 0-13 respectively.

$$\left(L_w/\theta\right)^2 = 0.158\frac{x}{2\theta} + 2.494 \qquad \text{Eq (0-12)}$$

$$\left(U_\infty/U_w\right)^2 = 2.133\frac{x}{2\theta} + 7.458 \qquad \text{Eq (0-13)}$$

Note that in Gliebe et al there is an inconsistency between the definition of non-dimensional distance X. In Section 3.4.4 of [21] $X = (x - x_0)/2\theta$, while in Section 3.6 of [21] $X = (x/2\theta)$. This is an important distinction. Wygnanski et al [50] chose only one value of x_0 for each generator investigated and this value had to satisfy the dependence of both U_w and L_w on initial conditions. As Gliebe et al derive equations as a function of x relative to the trailing edge, i.e. not from the virtual origin, these have been reproduced here. This then allows estimation of the correct virtual origin by calculation of the position where the ordinate equals zero.

Note that from Equations 0-12 and 0-13, the virtual origins of the wake half-width and centreline velocity deficit may not be the same. Figure 0-4 below shows a comparison between a predicted and measured normalised wake velocity defect profiles. The measured data presented The predicted velocity defect profile is calculated by

$$f(\eta) = \exp\left(-0.637\eta^2 - 0.056\eta^4\right) \qquad \text{Eq (0-14)}$$

with the measured data presented being taken from hotwire measurements recorded by Gliebe et al. Eq (0-14) is the mean wake equation of Wygnanski et al for a cylinder, including a fourth order correction. The hotwire data is normalized by $(U_\infty - U)/(U_\infty - U_{\min})$, and L_w is calculated from Equation 0-12 above, i.e. the half-wake width calculated from the turbulence intensity. The comparison is shown for two downstream distances at 50% immersion. The correlation is seen to be quite good in both cases, though accuracy improves further downstream.

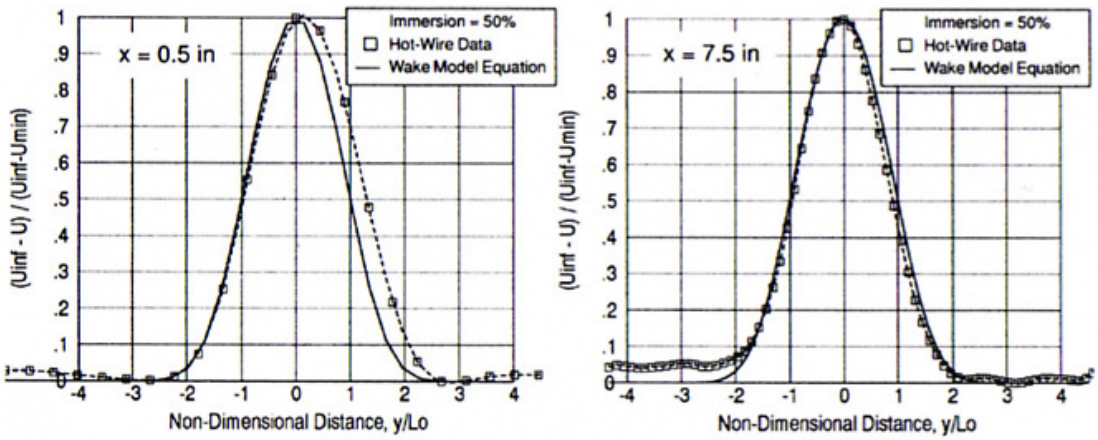

Figure 0-4 – Mean velocity comparison: x = 0.5 and x = 7.5 at Throttle 30 [21]

In addition to the turbulent wake velocity deficit and half-wake width, turbulence parameters include those listed below. Gliebe et al. also normalises these parameters and develops correlations for their behaviour. These are summarised below.

- Total wake maximum rms turbulence intensity (circumferentially averaged)

$$\frac{V'}{U_w} = 0.004417\left(\frac{x}{2\theta}\right) + 0.1402 \qquad \text{Eq (0-15)}$$

- Individual components of the turbulent velocity amplitudes and integral length scales follow the formula shown below in Equation 0-16

$$\frac{A}{U_w} = B\left(\frac{x}{2\theta}\right) + C \qquad \text{Eq (0-16)}$$

Considering the turbulent velocity components, these are the axial, circumferential, and radial directions respectively. The coefficients *B* and *C* for each turbulent velocity component are shown below in Table 1.

A	*B*	*C*	*Component*
u	0.004132	0.1412	Axial
v	0.004005	0.1423	Circumferential
w	0.005114	0.1371	Radial

Table 1 – Coefficients of Equation 0-16 for turbulence component correlations

From the similarity of these coefficients *B* and *C*, it appears that the flow is close to isotropy. Gliebe et al and Ganz et al find that the three components of the averaged individual turbulent velocity components are very similar in magnitude, indicating that the turbulence is approximately isotropic in the mid-span section, outside the effective regions of hub and tip flow. Evidence of isotropy is also seen, though less strongly when comparing integral length scales of the streamwise turbulent velocity component below.

Gliebe et al. find from their experimental data that the turbulence intensity, based on the freestream velocity at the rotor trailing edge plane, does not vary significantly with increasing downstream distance. This seems contrary to intuition. However, Gliebe et al display the normalised trends, such as those of the individual turbulence components, as the turbulence velocity rms amplitude normalized by U_w. It is known from Wygnanski et al that U_w decreases with increasing downstream distance. Therefore as the wake velocity defect decays, u_i/U_w increases and the absolute value of the normalized turbulence velocity remains approximately constant.

The turbulent wakes are found to be well defined in the mid-span region. This clarity reduces in the hub and tip regions due to interaction between the wake and wall boundary layer, as was found for the mean velocity wake. Ganz et al. present measurements of the turbulence intensity rms velocity normalized by the circumferentially averaged axial velocity. These are found to be small, less than 1%, between rotor wakes, though reaching up to 4% or 6% in the wake core. The variation of intensity for the transverse velocity component is found to increase sharply when crossing the wake, as opposed to the region between wakes, similar to that observed in 2D wakes.

Both Gliebe et al. and Ganz et al. find that the distribution of the transverse turbulent velocity component is approximately symmetric across a wake pitch. The streamwise turbulence intensity component peaks slightly towards the trailing edge of the suction side of the wake pitch, and the radial turbulent intensity velocity component peaks at the leading edge of the pressure side of the wake. This is seen below in Figure 0-5, an example taken from [16]:

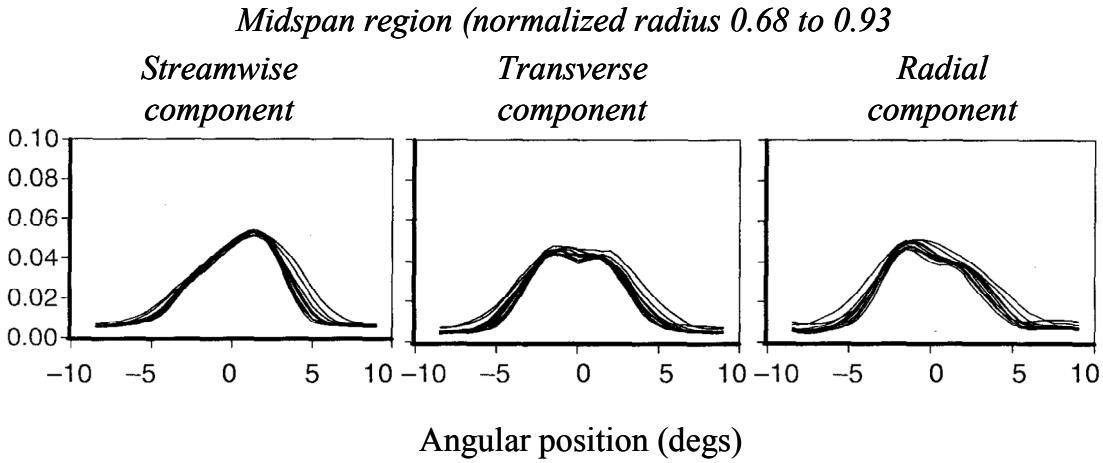

Figure 0-5 – Turbulence intensities in stationary coordinate system
Corrected fan speed 70%, low fan loading, large tip clearance

Due to the single-point hot-wire measurements performed by both Gliebe et al and Ganz et al, only the streamwise integral length scales are considered for each component. Ganz et al use Equation 0-17 below to calculate the integral length scales. Displayed is the equation for the streamwise integral length scale of velocity component *u*, equivalent equations are used for velocity components *v* and *w*:

$$\frac{\lambda_u}{\delta} = \lim_{f \to 0} PSD_{uu}(f) \frac{U}{\left(4\overline{u^2}\delta\right)} \qquad \text{Eq (0-17)}$$

In Equation 0-17, U is the mean flow velocity, $PSD_{uu}(f)$ is the power spectral density of velocity component u at frequency f, $\overline{u^2}$ denotes the variance of turbulence component u, and δ is the

normalising length scale. Gliebe et al do not specify how the integral length scales in [21] are calculated.

Ganz et al. presents measured ratios of streamwise integral length scales normalized by wake width and duct radius as seen below in Figure 0-6:

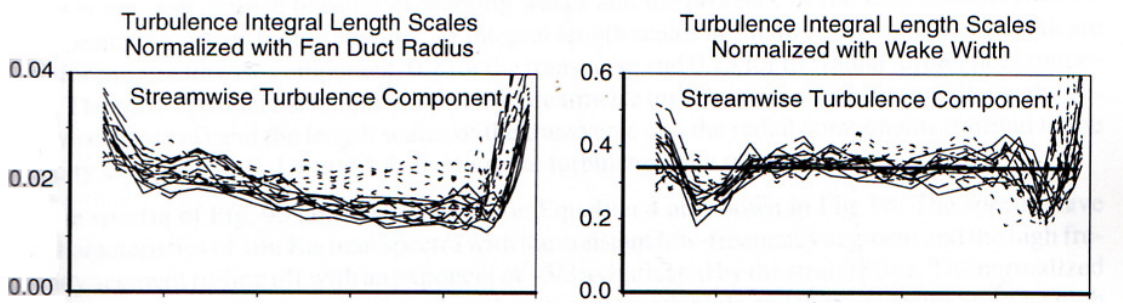

Figure 0-6 – Comparison of streamwise integral length scales normalized by duct radius and wake width, from [16]

The trailing edge momentum thickness θ is not considered as a normalising length scale. Normalising by wake width is found to provide better collapse of data. Ganz et al calculate the ratio of axial integral length scale to circumferential integral length scale as 1.8, while that of axial integral length scale to radial integral length scale is 1.4. The isotropic turbulence ratio is 2, indicating that, as found by Gliebe et al., the flow is approximately isotropic in the mid-span region.

Gliebe et al find that the axial length scales give the best correlations as a function of x when normalized by the local wake momentum thickness. Gliebe et al find that the correlations are very weak when normalized by L_w, calculated from either the mean velocity profile or the turbulence intensity profile, and blade-to-blade circumferential spacing. The axial length scale correlation for each turbulence velocity component can be seen below in Appendix C-3.

It is interesting that both Gliebe et al and Ganz et al find that the statistical properties of complex highly non-homogenous turbulence have similarities to isotropic turbulence, as seen for both turbulent velocity components and integral length scales. This implies that turbulence spectra may be normalized in a fashion used for isotropic turbulence.

Appendix C-3 : Summary of correlation coefficients proposed by Gliebe et al for estimation of the turbulent wake of a rotor

Gliebe et al. recommends the following correlation equations for estimating fan rotor wake mean velocity and turbulence velocities and length scales. Parameters used in the correlation equations are the axial distance downstream of the trailing edge x and the trailing edge momentum thickness θ. The

wake trailing edge momentum thickness can be approximated by the section drag coefficient C_D and the blade chord c, using the approximate relation displayed below in Eq (0-18):

$$\theta \approx C_d . \frac{c}{2} \qquad \text{Eq (0-18)}$$

All correlation equations take the form:

$$Y = MX + C \qquad \text{Eq (0-19)}$$

where $X = x / 2\theta$.

Y	M	C
$\left(L_w / \theta\right)^2$	0.158	2.494
$\left(U_\infty / u_w\right)^2$	2.133	7.458
$\frac{V'}{u_w}$	0.004417	0.1402
$\frac{u'}{u_w}$	0.004132	0.1412
$\frac{v'}{u_w}$	0.004005	0.1423
$\frac{w'}{u_w}$	0.005114	0.1371
$\frac{\lambda_u}{\theta}$	0.03746	1.223
$\frac{\lambda_v}{\theta}$	0.02816	1.532
$\frac{\lambda_w}{\theta}$	0.02691	1.3225

Table 12 – Correlation coefficients for use in Equation 0-19

Appendix D-1 : Basic Fan Performance Theory and Through-Flow Analysis

In addition to an understanding of turbulent wakes, modelling and modifying fan performance are also important factors within this thesis. The following D-appendices introduce various means of calculating and assessing fan performance. These include velocity triangles, rotor aerodynamic behaviour, and fan working lines.

The following Appendix D-2 on velocity triangles also introduces a basic mechanism of *through-flow* analysis. A through-flow program is used for several investigations described in this thesis, to provide aerodynamic and performance data at specified fan performance points. The through-flow program used is a two-dimensional axi-symmetric program that models the modifications to flow streams caused by the existence of the fan, using the theory of velocity triangles.

Appendix D-2 : Velocity Triangles

When considering the fan stage of a turbofan engine there are two possible frames of reference, that of the rotor or that of the nacelle.

In the nacelle frame of reference the observer appears to be sitting on the nacelle, and therefore views the fan rotating. In this frame of reference the air flow velocity is called the *absolute velocity*. This can be resolved using Pythagoras' theorem into two mutually perpendicular velocity components. These are the *axial velocity* of the air moving in the axial direction, and the *absolute whirl velocity* of the air moving in a circumferential direction around the nacelle.

In the rotor frame of reference the observer appears to be sitting on the rotor, which therefore appears to be stationary cascade of blades. The air flow then appears to be approaching at a *relative velocity*, which is made up of the absolute velocity vector and the *circumferential whirl velocity* of the air towards the blades. This circumferential whirl velocity is the blade circumferential (rotational) velocity U. It is important to note that the axial flow velocity is the same in both frames of reference.

These vectors can be seen below in a *velocity triangle*. Velocity triangles are a useful tool in understanding and designing rotating components in turbo-machines as they combine these two frames of reference in a compact format. They can be constructed at each stage in a compressor. To model the flow about a fan rotor, two are used. These can be seen below.

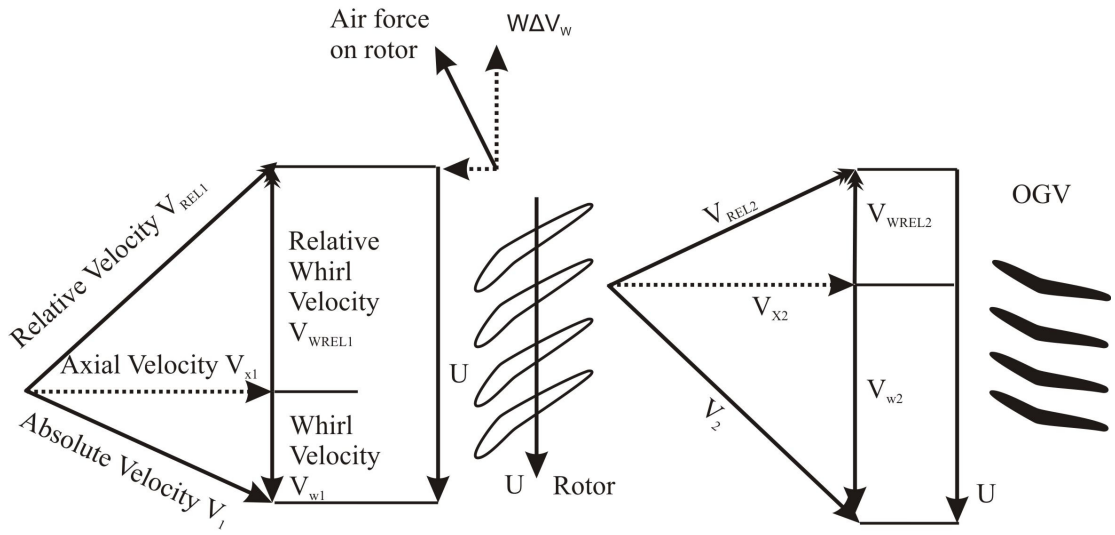

Figure 0-7 – Image of fan rotor velocity triangles

Appendix D-3 : Rotor Aerodynamic Behaviour

The relative velocity V_{REL1} approaches the rotor at a steep angle. This angle is reduced as the rotor turns the relative velocity towards the axial, which also increases the flow passage width. This increases the flow area normal to the relative flow direction, which causes the subsonic flow to slow down. The reactive force that acts to slow down the moving air is provided by the greater downstream static pressure. This slowing reduces the bulk kinetic energy, which becomes random thermal energy thereby causing the static temperature to rise. As the increase in static pressure is larger than the increase in static temperature the equation of state dictates that the density rises. These effects combine to cause a reduction in relative flow velocity greater than the increase in relative flow area.

The absolute whirl velocity of the flow exiting the rotor is larger than that entering due to the additional absolute velocity imparted on the flow by the rotor. Therefore the flow relative to the following stator/OGVs approaches at a steep angle (V_2 exiting the fan becomes equivalent to V_{REL1} entering the OGVs). The OGVs then perform the same role as the upstream rotor by turning the flow towards the axial, increasing the area normal to the absolute flow direction, and increasing the static temperature and pressure.

It is important to note that the air is always slowing down in the whirl direction relative to the rotor or stator it is passing through. However the flow never comes to a stop as what slows the flow relative to the rotor speeds it up relative to the following stator and vice-versa.

As the air moves over the rotor blades, which are modified aerofoil profiles, these apply a 'lift' force on the rotor which opposes the rotation of the fan. Therefore in the absolute frame it is necessary to input work to the fan in order to maintain rotation. This work is transmitted from the LP (low pressure) turbine via the LP shaft.

Relative total (stagnation) temperature of a gas travelling through a rotor passage at constant radius will remain constant provided no heat or *relative* shaft work is imparted. Friction due to the no-slip condition on the blade surfaces will decrease the flow velocity and increase the static temperature, but stagnation temperature remains constant. If laminar flow is assumed stagnation pressure will also remain constant, though not if friction is present.

For subsonic flow, a divergent rotor passage acts as a diffuser, slowing down the relative velocity of the flow as mentioned above. If viewing the fan perpendicular to the relative flow direction all of the passages are divergent.

If a flow streamline does not remain at constant radius when moving from the rotor leading edge to the rotor trailing edge but instead moves towards the blade tip, then the flow at the rear will be moving faster than that at the leading edge. Therefore there will be an increase in the relative stagnation temperature as more kinetic energy is converted to thermal energy. If this is the case extra shaft work in the absolute frame will have been done on the flow. All of the above comments also apply to the OGVs.

As mentioned above, in the relative frame of reference the fan and OGV's act as diffusers increasing the static pressure and slowing the relative velocity of the flow. In the absolute frame of reference the air passing through the fan is compressed into a smaller volume as it is accelerated in the direction of rotation. This rotation is opposed by the lift force of the fan blades which act as brakes against the rotation. This braking force is $M\Delta V_W$ where M is the mass flow rate through the fan. Assuming that the streamlines through the fan remain at constant radius then the rate of doing work is $MU\Delta V_W$. Another way of expressing the rate of doing work is $MC_P\Delta T$, where ΔT is the change in absolute stagnation temperature through the stage. Therefore one can state the Euler work equation that.

$$MC_P\Delta T = MU\Delta V_W \qquad \text{Eq (0-20)}$$

This equation is derived in Appendix F-1.

The change in whirl velocity ΔV_W is the same in both the absolute and relative frames of reference. Figure 0-8 below displays the magnitude of ΔV_W by overlaying the two fan velocity triangles

displayed previously. The blue lines denote the flow at fan inlet and the red lines denote the flow at fan exit.

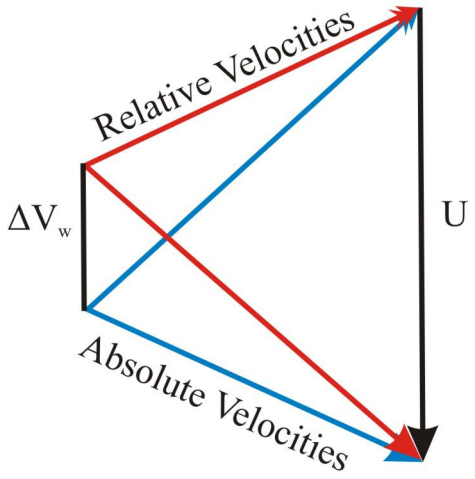

Figure 0-8 – Overlaid velocity triangles displaying ΔV_W

If the component efficiency is known then the rise in stagnation temperature can be used to calculate the rise in stagnation pressure, and vice-versa.

The above work equation and absolute stagnation variables allow the calculation of the overall component performance, but do not help in the design of the blade shape required; for this the relative velocities are needed. If the relative approach velocity and inlet static conditions are known then the relative stagnation conditions can be calculated. Recalling that in the relative frame of reference no work is done either by or on the rotor as it is not moving, therefore assuming constant radius the stagnation temperature does not change across the component. Relative stagnation pressure will fall slightly due to frictional losses, and therefore relative stagnation exit values are known. Then knowing ΔV_W and assuming constant axial Mach number across the fan then the relative exit velocity can be calculated.

This procedure is repeated for the OGV cascade, using the fan exit static conditions as inlet conditions to the OGVs.

In summary the increase in static pressure through the fan can be explained two ways:

1. In the absolute frame of reference by shaft work compressing the air into a smaller volume by accelerating it
2. In the relative frame of reference by slowing the air down and converting the bulk kinetic energy to random thermal energy as the air squashes. No relative work is done.

This is essentially the procedure followed by Q263, the through-flow calculation program that is used in this investigation to calculate new flow angles and component performances for different flight points. These flight points can be located on a working line diagram which is described next.

Appendix D-4 : Working Lines

A working line traces the pressure ratio and mass flow at different steady-state values of rotational speed. For a given value of pressure ratio and mass flow the fan will pick the appropriate speed value. A basic working line plot can be seen below in Figure 0-9. Note that as the temperature during measurement can vary, the constant speed lines are in fact constant $N/\sqrt{T}$ lines.

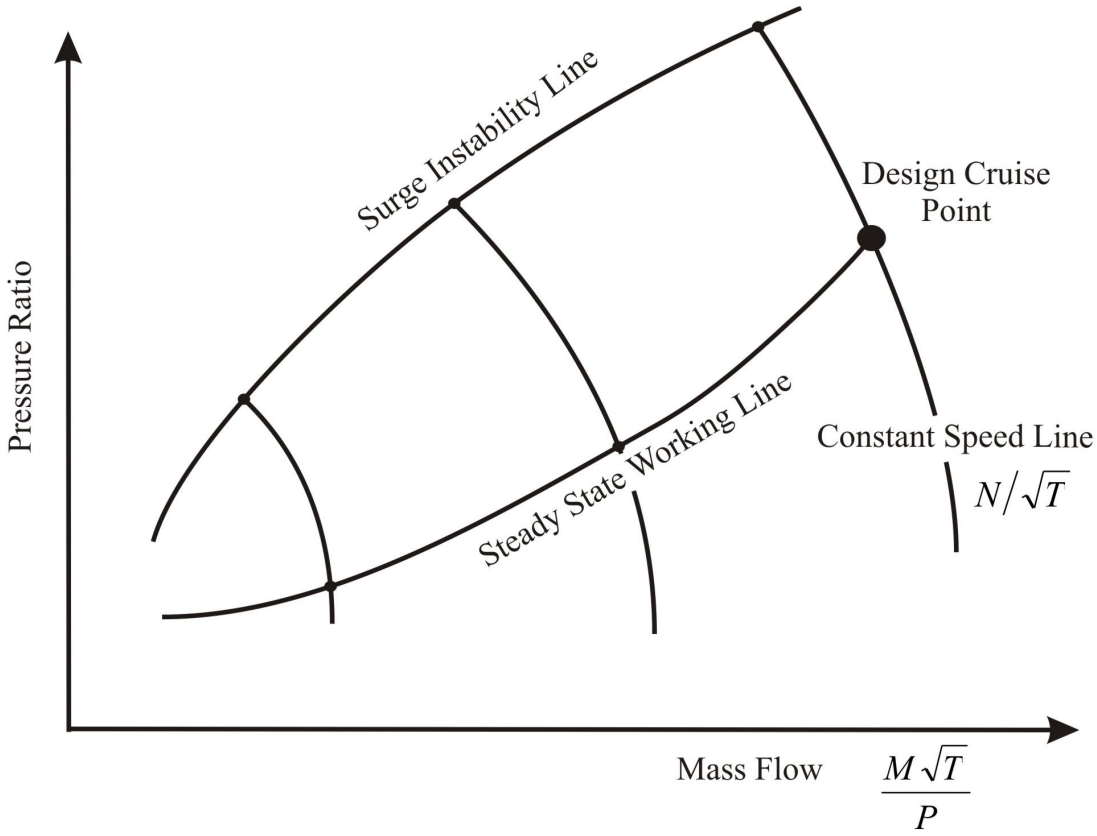

Figure 0-9 – Basic working line schematic tracing an example steady state working line

If shaft speed is maintained and mass flow reduced (equivalent to reducing the flow axial velocity), this increases the angle of incidence onto the fan blades. Assuming that the deviation of the flow leaving the blade trailing edges remains constant this means that each blade must turn the flow a larger amount. Therefore the desired pressure rise asked of the blades for a given inlet relative dynamic head increases; if this increases too far then the blades will stall. Eventually a 'surge' may occur where the flow regime breaks down and flow reversal can occur. The line locating this behaviour for a given rotational speed, there the component starts to stall or surge, is called the surge line.

Alternatively, increasing the flow passing through the fan for a given rotational speed reduces the amount of turning required of the fan. As the mass flow increases further the passages between blades will start to choke. This means that the flow passing through the throat of the passage (the narrowest

part) reaches Mach 1, at which point no further increase in mass flow is possible. Blade passage area increases after the throat and the subsonic flow slows down, this gives an overall reduction in relative speed through the passage. The mass flow at which choking takes place increases with increasing shaft speed.

Appendix E-1 : Calculation of momentum thickness from pressure loss coefficient

This Appendix will describe the conversion from fan Pressure Loss Coefficient (PLC) to momentum thickness, which forms the input to the wake correlation model derived by Gliebe et al.

The objective of the fan is to produce a rise in static pressure, thereby deflecting the flow. The PLC is defined as the difference between the inlet and exit stagnation pressures, normalized by the inlet relative dynamic pressure:

$$\overline{\omega}_i = \frac{(P_{01} - P_{02})}{(P_{01} - p_1)} = \frac{\Delta P}{q_{rel\_in}} = \frac{\Delta P}{\frac{1}{2}\rho U_{i\infty}^2} \qquad \text{Eq (0-21)}$$

Note that $U_{i\infty}$ is the inlet freestream velocity. Eq (0-21) is valid for low Mach or incompressible flow, where P is the stagnation pressure, p denotes the static pressure, and q is the dynamic pressure. The subscripts 1 and 2 denote fan inlet and exit respectively. Bernoulli's equation is valid for incompressible flow, which states that:

$$P = p + \frac{1}{2}\rho U^2 \qquad \text{Eq (0-22)}$$

The blade wake displacement and momentum thicknesses can be related to this pressure loss, in that the flow momentum lost due to this pressure loss across the blade equals the momentum thickness of the wake and therefore the pressure loss across the blade is equivalent to the pressure loss traversing the wake.

Consider the blade wake across a single passage:

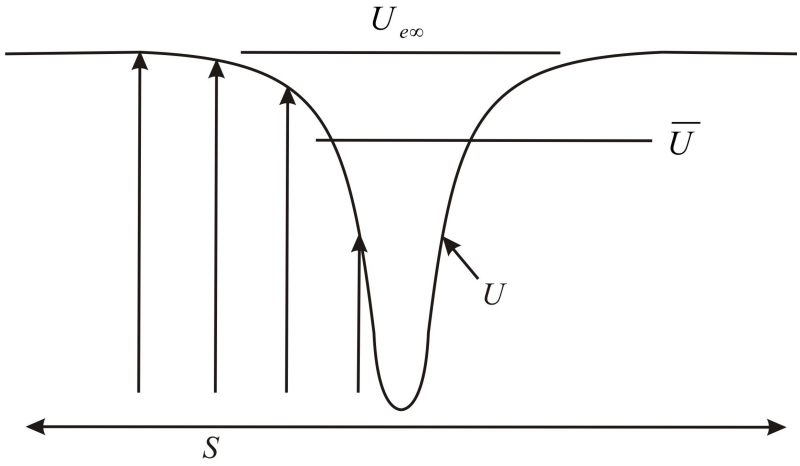

Figure 0-10 – Typical wake of one blade passage

In Figure 0-10 $U_{e\infty}$ is the blade exit freestream velocity, U is the actual velocity across the wake, $\overline{U}$ is the mean velocity, and S is the blade passage width. The displacement thickness of the wake is calculated using Eq (0-23) below:

$$\delta^* = \int_S \left(1 - \frac{U}{U_{e\infty}}\right) dy \qquad \text{Eq (0-23)}$$

The displacement thickness is physically the (circumferential) distance through which the mean flow streamlines are displaced due to the presence of the blade wake. The mean velocity $\overline{U}$ can be calculated by integrating the velocity across the wake:

$$\overline{U} = \frac{1}{S}\int U dy \qquad \text{Eq (0-24)}$$

This is related to the displacement thickness by Eq (0-25)

$$\overline{U} = U_{e\infty}\left(1 - \frac{\delta^*}{S}\right) \qquad \text{Eq (0-25)}$$

In Eq (0-25) the term in brackets is equal to the wake blockage.

The pressure loss across the wake can be written as

$$\Delta P = \tfrac{1}{2}\rho U_{e\infty}^2 \left\{1 - \left(\frac{\overline{U}}{U_{e\infty}}\right)^2\right\} \qquad \text{Eq (0-26)}$$

Normalising Eq (0-26) with the freestream dynamic pressure leads to

$$\overline{\omega_i} = 1 - \left(\frac{\overline{U}}{U_{e\infty}} \right)^2 \qquad \text{Eq (0-27)}$$

Combining Eq (0-25) and Eq (0-27) leads to

$$\frac{\delta^*}{S} = 1 - \sqrt{1 - \overline{\omega_i}} \approx \frac{\overline{\omega_i}}{2} \qquad \text{Eq (0-28)}$$

which relates the displacement thickness to the incompressible pressure loss coefficient.

A quantity that is fundamental to the prediction of the wake is the momentum thickness θ, which can be derived from the momentum integral equation

$$\theta = \frac{F}{\rho U_{e\infty}^2} = \int_{-\infty}^{\infty} \frac{U}{U_{e\infty}} \left(1 - \frac{U}{U_{e\infty}} \right) dy \qquad \text{Eq (0-29)}$$

The drag force F per unit span and freestream velocity $U_{e\infty}$ are constants of the wake generator that are independent of the distance downstream. This can also be non-dimensionalised:

$$C_D = \frac{D}{\frac{1}{2}\rho U_{e\infty}^2 c} = \frac{2\theta}{c} \qquad \text{Eq (0-30)}$$

where c is the blade chord.

The shape ('flatness') of the mean velocity profile is quantified by the 'Shape Factor' H, defined as the ratio of displacement and momentum thicknesses.

$$H = \frac{\delta^*}{\theta} \qquad \text{Eq (0-31)}$$

As in channel flow, when Reynolds number increases the velocity profile becomes steeper close to wake centreline (or the wall in the case of channel flow), and flatter away from the centreline. Therefore H decreases with increasing Reynolds number. For the Blasius boundary layer $H \approx 2.6$, while for the Klebanoff boundary layer $H \approx 1.3$.

Assuming a value of $H \approx 2$, combining Eq (0-28)and Eq (0-31) allows the drag coefficient to be written as:

$$C_D = \frac{S}{C} \overline{\omega_i} \qquad \text{Eq (0-32)}$$

Assuming that the pressure loss across the blade remains constant over a sufficiently wide velocity range (neglecting flow discontinuity effects), it is possible to relate $\overline{\omega_i}$ which is the pressure loss coefficient based on the incompressible dynamic pressure at exit, to the pressure loss coefficient based on the compressible dynamic pressure at inlet:

$$\Delta P = \overline{\omega} q_{rel\_in} = \overline{\omega_i} q_{i\_rel\_ex} \qquad \text{Eq (0-33)}$$

$$\overline{\omega} = \frac{\Delta P}{q_{rel\_in}} = \frac{\overline{\omega_i} q_{i\_rel\_ex}}{q_{rel\_in}} \qquad \text{Eq (0-34)}$$

Therefore the drag can be related to the loss coefficient:

$$C_D = \frac{S}{C} \overline{\omega} \frac{q_{rel\_in}}{q_{i\_rel\_ex}} \qquad \text{Eq (0-35)}$$

Inserting Eq (0-30) this becomes

$$\theta = \frac{S}{2} \overline{\omega_i} = \frac{S}{2} \overline{\omega} \frac{q_{rel\_in}}{q_{i\_rel\_ex}} \qquad \text{Eq (0-36)}$$

The correlations derived by Gliebe et al use the derived momentum thickness and distance downstream as input parameters, and provide the turbulent velocity fluctuations and turbulence length scale required by the rotor-stator broadband noise model.

Appendix F-1 : Derivation of the Euler work equation

This derivation is based on that found in Reference [12].

Consider a hypothetical fan blade rotating at an angular velocity denoted Ω in radians/sec. Flow enters the fan at radius r_1 with a tangential whirl velocity V_{W1}, and exits at a radius r_2 with a whirl velocity of V_{W2}. If an imaginary packet of fluid of mass $\delta m = \dot{m} \delta t$ passes through the rotor, this packet has momentum $\delta m r_1 V_{W1}$ on entry and $\delta m r_2 V_{W2}$. Torque is equal to the rate of change of moment of momentum, which can be written as:

$$T = \dot{m}\left(r_2 V_{W2} - r_1 V_{W1}\right) \qquad \text{Eq (0-37)}$$

The power can then be written as:

$$\dot{W} = T\Omega = \dot{m}\Omega\left(r_2 V_{W2} - r_1 V_{W1}\right) = \dot{m}\left(U_2 V_{W2} - U_1 V_{W!}\right) \quad \text{Eq (0-38)}$$

U_1 and U_2 are therefore the speed of the blade row at inlet and outlet. The power is also equal to the mass flow rate times the change in stagnation enthalpy per unit mass; $\dot{W} = \dot{m}\Delta h_0$.

The enthalpy h can be described by Eq (0-39) below:

$$h = e + pv \quad \text{Eq (0-39)}$$

The internal energy is denoted e, pressure p, and specific volume v. Note that pv is not the 'pressure energy'. The pressure is the facilitator that enables conversion from thermal energy to, in this case, displacement work. As the pressure increases the specific volume of the fluid packet this is the 'bulk displacement energy'.

If the process is assumed to be isentropic, and the specific heat capacity of the gas is a constant value, then the gas is said to be *calorically perfect*. Enthalpy can be written

$$h = c_p T \quad \text{Eq (0-40)}$$

Total enthalpy is given by:

$$h_0 = h + \frac{V^2}{2} \quad \text{Eq (0-41)}$$

where V is the axial flow velocity through the fan. From Eq (0-38) it can be written that:

$$\Delta h_0 = U_2 V_{W2} - U_1 V_{W1} \quad \text{Eq (0-42)}$$

Assuming that V does not change through the fan it can be written that:

$$\Delta h_0 = \Delta h = C_p \Delta T = U_2 V_{W2} - U_1 V_{W1} \qquad C_p \Delta T = U \Delta V_W \quad \text{Eq (0-43)}$$

Appendix G-1 : Derivation of temperature ratio

$$\eta_{comp} = \frac{T_{3i} - T_2}{T_3 - T_2} \quad \text{Eq (0-44)}$$

$$\frac{T_{3i}}{T_2} = \left(\frac{P_3}{P_2}\right)^{\frac{\gamma-1}{\gamma}} \quad \text{Eq (0-45)}$$

$$\eta\left(T_3 - T_2\right) = T_{3i} - T_2 \quad \text{Eq (0-46)}$$

$$\eta\left(T_3 - T_2\right) = T_2\left(\frac{P_3}{P_2}\right)^{\frac{\gamma-1}{\gamma}} - T_2 \quad \text{Eq (0-47)}$$

$$T_3 - T_2 = \frac{\left[T_2\left(\frac{P_3}{P_2}\right)^{\frac{\gamma-1}{\gamma}} - T_2\right]}{\eta} \quad \text{Eq (0-48)}$$

$$\frac{T_3}{T_2} = 1 + \frac{\left[\left(\frac{P_3}{P_2}\right)^{\frac{\gamma-1}{\gamma}} - 1\right]}{\eta} \quad \text{Eq (0-49)}$$

Appendix H-1 : Derivation of least squares analysis

From Eq (4.5-1) assume two broadband noise levels being calculated using two predictors. This can be written as:

$$\begin{aligned} w_1 &= P_{1,1}a_1 + P_{2,1}a_2 \\ w_2 &= P_{1,2}a_1 + P_{2,2}a_2 \end{aligned} \quad \text{Eq (0-50)}$$

The residual equation Eq (4.6.1-1) can be rewritten using Eq (0-50) above as

$$\begin{aligned} r_1 &= w_1 - P_{1,1}a_1 - P_{2,1}a_2 \\ r_2 &= w_2 - P_{1,2}a_1 - P_{2,2}a_2 \end{aligned} \quad \text{Eq (0-51)}$$

alternatively

$$r_j = w_j - \sum_i^2 P_{i,j}a_i = \mathbf{w} - \mathbf{Pa} \quad \text{Eq (0-52)}$$

where **w** is a vector of length *j*, **a** is a vector of length *i*, and **P** is a matrix of dimensions $i \times j$ The least squares method attempts to minimise the square of the residual. The length of vector **r** is the *norm* of the residual vector, therefore Eq (0-52) squared can be written as

$$\begin{aligned}\mathbf{r}^2 = \mathbf{r}^T\mathbf{r} &= \left(\mathbf{w}-\mathbf{P}\mathbf{a}\right)^T\left(\mathbf{w}-\mathbf{P}\mathbf{a}\right) \\ &= \left(\mathbf{w}^T\mathbf{w}-\mathbf{w}^T\mathbf{P}\mathbf{a}-\mathbf{a}^T\mathbf{P}^T\mathbf{w}+\mathbf{a}^T\mathbf{P}^T\mathbf{P}\mathbf{a}\right) \\ &= \left(\mathbf{w}^T\mathbf{w}-2\mathbf{w}^T\mathbf{P}\mathbf{a}+\mathbf{P}^T\mathbf{P}\mathbf{a}^2\right)\end{aligned} \qquad \text{Eq (0-53)}$$

Eq (0-53) is minimised when

$$\frac{\partial\mathbf{r}^2}{\partial\mathbf{a}} = \left(-2\mathbf{w}^T\mathbf{P}+2\mathbf{P}^T\mathbf{P}\mathbf{a}\right)=0 \qquad \text{Eq (0-54)}$$

Dividing Eq (0-54) by 2, and rearranging leads to:

$$\mathbf{P}^T\mathbf{w} = \mathbf{P}^T\mathbf{P}\mathbf{a} \qquad \text{Eq (0-55)}$$

which is Eq (4.6.1-2) above.